



The Preserve: Lehigh Library Digital Collections

# Exploring Interfacial Structure Near a Hydrophobic Surface: A Computational Study

## Citation

Kaya, Orhan. *Exploring Interfacial Structure Near a Hydrophobic Surface: A Computational Study*. 2025, <https://preserve.lehigh.edu/lehigh-scholarship/graduate-publications-theses-dissertations/theses-dissertations/exploring-19>.

Find more at <https://preserve.lehigh.edu/>

*This document is brought to you for free and open access by Lehigh Preserve. It has been accepted for inclusion by an authorized administrator of Lehigh Preserve. For more information, please contact [preserve@lehigh.edu](mailto:preserve@lehigh.edu).*

# Exploring Interfacial Structure Near a Hydrophobic Surface: A Computational Study

by

Orhan Kaya

Presented to the Graduate and Research Committee  
of Lehigh University  
in Candidacy for the Degree of  
Doctor of Philosophy  
in  
Mechanical Engineering and Mechanics

Lehigh University

January 2025

© 2025 Copyright  
Orhan Kaya

Approved and recommended for acceptance as a dissertation in partial fulfillment  
of the requirements for the degree of Doctor of Philosophy.

---

Defense Date

---

Approved

---

Dissertation Director

Committee Members:

---

Alparslan Oztekin, (Director)  
(MEM, Lehigh University)

---

Meng-Sang Chew (Member)  
(MEM, Lehigh University)

---

Yue Yu (Member)  
(MATH, Lehigh University)

---

Edmund B. Webb III (Member)  
(MEM, Lehigh University)

## **Acknowledgments**

I would like to express my deepest gratitude to the Ministry of National Education, Türkiye, for their financial support. Without their invaluable assistance, my PhD studies would not have been possible.

I would also like to extend my thanks to the members of my committee for their support in the preparation of this dissertation.

# Table of Contents

<b>Acknowledgments</b> .....	iv
<b>List of Tables</b> .....	viii
<b>List of Figures</b> .....	xi
<b>Abstract</b> .....	1
 <b>Chapter 1: Introduction</b> .....	 2
1.1. Motivation .....	2
1.2. Research objectives and original contributions to the literature .....	4
1.2.1. Development of Force Field Parameters .....	5
1.2.1.1. TD-bonded parameters .....	6
1.2.1.2. PTFE parameters .....	7
1.2.2. Aqueous solution droplets over a PTFE surface .....	10
1.2.3. Aqueous solution slabs over a PTFE surface .....	12
1.3. Outline of the dissertation .....	14
 <b>Chapter 2: Computational Methodology</b> .....	 17
2.1. Force field development .....	17
2.2. Molecular dynamics .....	23
2.2.1. Discretization schemes .....	23
2.2.2. Interactions between atoms .....	24
2.2.3. Boundary conditions and periodicity.....	25
2.2.4. Limitations of molecular dynamics .....	25

<b>Chapter 3: Force Field Parameter for Titanocene Dichloride .....</b>	<b>26</b>
3.1. Introduction .....	26
3.2. Parameterization methods .....	26
3.2.1. CHARMM interaction model .....	26
3.2.2. Partial charge optimization .....	29
3.2.3. Bond and angle optimization .....	30
3.2.4. Dihedral optimization .....	31
3.3. Parameterization results .....	31
3.3.1. Charge parameters .....	32
3.3.2. Bond and angle parameters .....	35
3.3.3. Dihedral parameters .....	36
3.4. Validation methodologies and results .....	38
3.4.1. Power spectrum .....	38
3.4.2. Explicit solvent simulations .....	42
3.4.3. Normal mode analysis .....	44
 <b>Chapter 4: Force Field Parameter for Polytetrafluoroethylene .....</b>	 <b>46</b>
4.1. Introduction .....	46
4.2. Parameterization methods .....	47
4.2.1. AMBER interaction model .....	47
4.2.2. Charge optimization .....	48
4.2.3. Bond, angle, and dihedral optimization .....	48
4.2.4. Van der Waals optimization .....	51
4.3. Parameterization results .....	57
4.3.1. Charge parameters .....	57
4.3.2. Bond, angle, and dihedral parameters .....	58
4.3.3. Van der waals parameters .....	63
4.4. Validation methodologies and results .....	66
4.4.1. Density distribution .....	66
4.4.2. Radial distribution function .....	69
4.4.3. Power spectrum .....	71

4.4.4. Specific heat capacity .....	74
<b>Chapter 5: Effects of Salinity and Temperature on Droplet Wettability on Hydrophobic Surface.....</b>	<b>76</b>
5.1. Introduction .....	76
5.2. Methods .....	76
5.2.1. Simulation setting and molecular interactions .....	76
5.2.2. Constructing the simulation model.....	78
5.2.3. Measurement of surface roughness and contact angle .....	81
5.3. Results and discussion.....	91
5.3.1. Salinity and temperature effects .....	100
<b>Chapter 6: Interfacial Dynamics of Water Slabs on Hydrophobic Membrane..</b>	<b>109</b>
6.1. Introduction .....	109
6.2. Methods .....	110
6.2.1. Simulation setting and molecular interactions .....	110
6.2.2. Constructing the simulation model.....	112
6.3. Results and discussion.....	113
<b>Chapter 7: Conclusions and Recommendations for Future Research .....</b>	<b>124</b>
7.1. Conclusions .....	124
7.2. Recommendations for Future Research.....	126
<b>References .....</b>	<b>128</b>
<b>Vitae .....</b>	<b>139</b>



## List of Tables

<b>Table 1.</b> Comparison of experimental and predicted structures of assigned bonds (Å) and angles (°) for various basis sets.....	32
<b>Table 2.</b> The energies of interactions (kcal/mol) between the explicit TIP3P water and TD molecule. The MM interaction energies were calculated using the ffTK objective function.....	34
<b>Table 3.</b> The names and charges of the atoms in TD.....	34
<b>Table 4.</b> Optimized bond parameters for TD.....	36
<b>Table 5.</b> Optimized angle parameters for TD. ....	36
<b>Table 6.</b> Optimized dihedral parameters for TD.....	37
<b>Table 7.</b> Comparison of theoretical VDOS spectra with experimental IR spectrum of TD molecule. ....	41
<b>Table 8.</b> Comparison of experimental, QM optimized, MD probability distributions of angles and bond distances. ....	42
<b>Table 9.</b> The initial simplex has seven vertices in the parameter space. ....	52
<b>Table 10.</b> The simplex update operations and their equations in the parameter space.....	55
<b>Table 11.</b> Optimized charge parameters for PTFE. ....	58
<b>Table 12.</b> Optimized bond parameters for PTFE.....	60

<b>Table 13.</b> Optimized angle parameters for PTFE. ....	60
<b>Table 14.</b> Optimized dihedral parameters for PTFE. ....	60
<b>Table 15.</b> Comparison of the relative conformational energy differences (kcal/mol) of gauche (g), ortho (o), anti (a), trans (t) for C <sub>4</sub> F <sub>10</sub> as a function of the C-C-C-C torsional angle, using various force fields and their QM-derived counterpart values, including those from the present work [a], Okada et al. [7], the <i>n</i> -C <sub>4</sub> F <sub>10</sub> specific and generalized perfluoroalkane OPLS-AA force field [15], Jang et al. [10], and Borodin et al [17]. ....	62
<b>Table 16.</b> Optimized vdW parameters for PTFE. ....	64
<b>Table 17.</b> Comparison of our density (kg/m <sup>3</sup> ) and percent error (%) from MD simulations of various-sized PTFE ensembles, with MD simulations using Okada [7] and GAFF force field parameters [19], with the experimental density at 300 K reported in reference [65]. ....	68
<b>Table 18.</b> Lennard-Jones parameters and partial charges for PTFE, water, and ions..	78
<b>Table 19.</b> The configuration of six different cubic saline cases. ....	81
<b>Table 20.</b> This table presents the contact angles measured for droplets of various diameters (ranging from 20 nm to 30 nm) interacting with rough, amorphous PTFE surfaces. The data includes the effects of different temperatures (25°C and 80°C) and salinities (pure water and saline). ....	98
<b>Table 21.</b> Comparison of NaCl concentration changes for different sizes of nanodroplets at the end of 1 ns at 25°C and 80°C. ....	99
<b>Table 22.</b> Comparison of the positions of the first peaks in the radial distribution functions of experimentally obtained NaCl solutions, their standard deviations (in parentheses), and the MD simulation in this study.....	105

<b>Table 23.</b> Lennard-Jones parameters and partial charges for PTFE, water, and ions.....	111
<b>Table 24.</b> Configurations of water and ion count with $C_{NaCl}$ in saline and pure slabs on non-porous and porous PTFE.....	113
<b>Table 25.</b> The averaged pore contact angle measurements for pure and saline water slabs.....	120

## List of Figures

<b>Figure 1.</b> Illustration of Contact Angle and Wettability: Hydrophobic vs. Hydrophilic Surfaces.....	2
<b>Figure 2.</b> Illustration of Contact Angle and Wettability: Hydrophobic vs. Hydrophilic Surfaces.....	5
<b>Figure 3.</b> The schematic shows the path for valence, charge, and vdW parametrization.....	18
<b>Figure 4.</b> (a) Optimized water interactions between the explicit TIP3P water and TD molecule. (b) Schematic representation of atom labels used for the final partial charges shown in Table 3. ....	33
<b>Figure 5.</b> The comparison of QM reference data and MM force field data for (a) the bond fitting and (b) the angle fitting. ....	35
<b>Figure 6.</b> The percent error of the equilibrium QM and MM angles for all dihedral combinations is shown. ....	37
<b>Figure 7.</b> (a) Velocity autocorrelation function. (b) Velocity density of states (VDOS) or power spectrum of TD in the range 0 to 4000 $\text{cm}^{-1}$ calculated from the velocity autocorrelation function; red dashed lines show the experimental infrared spectrum. ....	40
<b>Figure 8.</b> Ti - Cl bond angle (d) and three angle values with the distances (a)(b)(c) were compared through a 10-ns explicit MD	

simulation to those resulting from QM optimum value and experimental data [48]. The horizontal axis displays the bond distance (in Å) or angle (in °) values, while the vertical axis shows 1000 instances of the probability density for a given measurement. ....	43
<b>Figure 9.</b> Comparison of normal mode analysis between frequencies produced by QM-APFD/6-31(d) and MM-CHARMM for titanocene dichloride. ....	45
<b>Figure 10.</b> a) The molecular structure schematic of PTFE consists of long chains with repeating units of tetrafluoroethylene (n units), as indicated in parentheses. b) A bond schematic of the reference molecule to be parameterized. ....	49
<b>Figure 11.</b> A schematic representation of the update mechanisms within the simplex optimization algorithm. ....	54
<b>Figure 12.</b> (a) The comparison between MM-calculated results and QM conformational energies across 29 conformational sets is presented. The comparison of bond lengths (b), bond angles (c), and dihedral angles (d) between MM-calculated results and QM reference values are shown, along with the total number of data points (Data), root mean square deviation (RMSD), average absolute deviation (AAD), and maximum value differences (Max). ....	59
<b>Figure 13.</b> Torsional energy versus C-C-C-C dihedral angle for <i>n</i> -C <sub>4</sub> F <sub>10</sub> (a) from QM APFD/6-31G* calculations (the present work) and calculations using the Okada et al., generalized perfluoroalkane OPLS-AA, and <i>n</i> -C <sub>4</sub> F <sub>10</sub> specific force fields. (b) from QM APFD/6-31G* calculations (the present work) and calculations using the force fields from Borodin et al. and Jang et al. ....	61
<b>Figure 14.</b> The iterative simplex update procedure starts with the first peak values in the plane highlighted in pink and ends in blue. ....	63

<b>Figure 15.</b> Variation of density (a) and heat of vaporization (b) with temperature for $n$ -C <sub>4</sub> F <sub>10</sub> . .....	65
<b>Figure 16.</b> The equilibrated cubic PTFE ensembles of varying size: (a) [CF <sub>3</sub> -(C <sub>2</sub> F <sub>4</sub> ) <sub>20</sub> -CF <sub>3</sub> ] <sub>20</sub> , (b) [CF <sub>3</sub> -(C <sub>2</sub> F <sub>4</sub> ) <sub>40</sub> -CF <sub>3</sub> ] <sub>40</sub> , (c) [CF <sub>3</sub> -(C <sub>2</sub> F <sub>4</sub> ) <sub>50</sub> -CF <sub>3</sub> ] <sub>50</sub> , and (d) [CF <sub>3</sub> -(C <sub>2</sub> F <sub>4</sub> ) <sub>100</sub> -CF <sub>3</sub> ] <sub>100</sub> . .....	68
<b>Figure 17.</b> Comparison of experimental RDF peak values with RDFs for equilibrated cubic PTFE ensembles of various sizes: [CF <sub>3</sub> -(C <sub>2</sub> F <sub>4</sub> ) <sub>20</sub> -CF <sub>3</sub> ] <sub>20</sub> , [CF <sub>3</sub> -(C <sub>2</sub> F <sub>4</sub> ) <sub>40</sub> -CF <sub>3</sub> ] <sub>40</sub> , [CF <sub>3</sub> -(C <sub>2</sub> F <sub>4</sub> ) <sub>50</sub> -CF <sub>3</sub> ] <sub>50</sub> , and [CF <sub>3</sub> -(C <sub>2</sub> F <sub>4</sub> ) <sub>100</sub> -CF <sub>3</sub> ] <sub>100</sub> . .....	70
<b>Figure 18.</b> (a) Temporal variation of the velocity autocorrelation function. (b) VDOS or power spectrum of the PTFE chain (500 to 2500 cm <sup>-1</sup> ) with experimental peak points shown by the red dashed lines. ....	73
<b>Figure 19.</b> Comparison of computed and experimental specific heat capacity vs. temperature for different ensembles of various sizes: [CF <sub>3</sub> -(C <sub>2</sub> F <sub>4</sub> ) <sub>20</sub> -CF <sub>3</sub> ] <sub>20</sub> , [CF <sub>3</sub> -(C <sub>2</sub> F <sub>4</sub> ) <sub>40</sub> -CF <sub>3</sub> ] <sub>40</sub> , [CF <sub>3</sub> -(C <sub>2</sub> F <sub>4</sub> ) <sub>50</sub> -CF <sub>3</sub> ] <sub>50</sub> , and [CF <sub>3</sub> -(C <sub>2</sub> F <sub>4</sub> ) <sub>100</sub> -CF <sub>3</sub> ] <sub>100</sub> . .....	75
<b>Figure 20.</b> Simulation model construction workflow: (a) Initial PTFE chain with $n = 50$ tetrafluoroethylene units. (b) Replication into 50 chains in a cubic lattice. (c) Energy minimization and 5 ns MD simulation at 298.15 K and 101.325 kPa. (d) Lattice replication to enlarge amorphous PTFE for analysis. (e) Integration of Na <sup>+</sup> and Cl <sup>-</sup> ions into an SPC/E water lattice. (f) Final merging of equilibrated saline and pure water lattices with PTFE at 298.15 K and 353.15 K. (g) Visualization of lattice configurations in 3D isometric and 2D orthographic projections. ....	80
<b>Figure 21.</b> The equilibration of a 20 nm pure droplet on the PTFE surface at 25°C is shown in MD snapshots (a)–(d) at (a) 0 ns, (b) 0.32 ns, (c) 0.6 ns and (d) 1 ns in the XZ plane. (f), (e), and (g) display the	

interfacial area growth over time for 20 nm, 25 nm, and 30 nm droplets, respectively. (Note: dashed lines mark stabilization points.).....	82
<b>Figure 22.</b> The total energies of the (a) 30 nm, (b) 25 nm, and (c) 20 nm droplet size as a function of simulation time. ....	83
<b>Figure 23.</b> The effect of temperature and salinity on the height of the droplet mass center (a) 30 nm, (b) 25 nm, and (c) 20 nm droplets on a PTFE surface. ....	86
<b>Figure 24.</b> Methodology for 20 nm droplet contact angle measurement: (a) Equilibration at 25°C in XZ and YZ views, (b) 30 Å central section removed, (c) Cross-sections post-removal, (d) Contact angle equation, (e) Tangent-based angle determination with PTFE surface. ....	88
<b>Figure 25.</b> This figure illustrates the interaction of 30 nm droplets with rough, amorphous PTFE surfaces at two temperatures (25°C and 80°C) and two salinities (pure water and saline) across different planes (XZ and YZ).....	89
<b>Figure 26.</b> This figure illustrates the interaction of 25 nm droplets with rough, amorphous PTFE surfaces at two temperatures (25°C and 80°C) and two salinities (pure water and saline) across different planes (XZ and YZ).....	90
<b>Figure 27.</b> This figure illustrates the interaction of 20 nm droplets with rough, amorphous PTFE surfaces at two temperatures (25°C and 80°C) and two salinities (pure water and saline) across different planes (XZ and YZ).....	90
<b>Figure 28.</b> Effect of salinity on the contact angle of droplets on a PTFE surface: Visualization of 20 nm diameter pure (a) and 8.45% saline (b) water droplets, each 3 nm thick, on a PTFE surface at 25°C in the XZ plane, including density contours. ....	91

<b>Figure 29.</b> This figure shows contact angle measurements of 20 nm pure droplets on rough, amorphous PTFE surfaces, including water/vapor interface data, PTFE surface roughness ( $R_a$ , $R_q$ ), and calculated contact angles ( $\theta_{xz}$ , $\theta_{yz}$ ).....	92
<b>Figure 30.</b> This figure shows contact angle measurements of 20 nm saline droplets on rough, amorphous PTFE surfaces, including water/vapor interface data, PTFE surface roughness ( $R_a$ , $R_q$ ), and calculated contact angles ( $\theta_{xz}$ , $\theta_{yz}$ ).....	93
<b>Figure 31.</b> This figure shows contact angle measurements of 25 nm pure droplets on rough, amorphous PTFE surfaces, including water/vapor interface data, PTFE surface roughness ( $R_a$ , $R_q$ ), and calculated contact angles ( $\theta_{xz}$ , $\theta_{yz}$ ).....	94
<b>Figure 32.</b> This figure shows contact angle measurements of 25 nm saline droplets on rough, amorphous PTFE surfaces, including water/vapor interface data, PTFE surface roughness ( $R_a$ , $R_q$ ), and calculated contact angles ( $\theta_{xz}$ , $\theta_{yz}$ ).....	95
<b>Figure 33.</b> This figure shows contact angle measurements of 30 nm pure droplets on rough, amorphous PTFE surfaces, including water/vapor interface data, PTFE surface roughness ( $R_a$ , $R_q$ ), and calculated contact angles ( $\theta_{xz}$ , $\theta_{yz}$ ).....	96
<b>Figure 34.</b> This figure shows contact angle measurements of 30 nm saline droplets on rough, amorphous PTFE surfaces, including water/vapor interface data, PTFE surface roughness ( $R_a$ , $R_q$ ), and calculated contact angles ( $\theta_{xz}$ , $\theta_{yz}$ ).....	97
<b>Figure 35.</b> The graph shows contact angle variation with size, salinity, and temperature. Dashed red and blue lines mark the experimental 2 mm droplet angles, as referenced [90]. .....	100



- Figure 36.** (a) Ion mass concentration and water density profiles, and (c) partial pressure of a NaCl nanodroplet at 25°C and 80°C over time.  
(Note: Avg is average intensity and Std is standard deviation). ..... 101
- Figure 37.** Visualization of the analysis setup for a 30 nm diameter droplet at 25°C in the YZ plane, used to assess the effects of salinity and temperature. .... 102
- Figure 38.** Ion mass concentration and density profiles of 30 nm NaCl nanodroplets: (a) Comparison between Free-floating and PTFE-adsorbed droplets, and (b) density and dimensionless density distributions near the PTFE Interface. (Note: The densities in the droplets have been normalized using the reference densities of PTFE, water, Na, and Cl.)  
(c) Visualization of interfacial roughness and spreading area growth.... 103
- Figure 39.** Radial distribution functions for atoms under different temperature and salinity conditions and in the presence (PTFE) or absence (Free) of a PTFE membrane: (a) sodium-oxygen, (b) chloride-oxygen, (c) sodium-hydrogen, and (d) chloride-hydrogen. 106
- Figure 40.** Radial distribution functions for atoms under different temperature and salinity conditions and in the presence (PTFE) or absence (Free) of a PTFE membrane: (a) oxygen-oxygen, and (b) chloride-sodium..... 107
- Figure 41.** The figure shows the assembly of the PTFE polymer and its merging with saline water slabs. In (a), the PTFE chain is constructed as  $\text{CF}_3-(\text{C}_2\text{F}_4)_n-\text{CF}_3$  with 'n' set to 50. In (b) and (c), the chains are duplicated, minimized, and replicated along the z-axis. In (d), the PTFE chains are fully assembled along the x- and y-axes. Panels (e) and (f) depict the merging of saline water slabs with non-porous and porous PTFE, highlighting the 24 nm pore in the porous PTFE..... 113

<b>Figure 42.</b> Center of mass shifts (a) and partial pressure variations (b) for pure and saline water slabs on porous and non-porous PTFE surfaces over time.....	114
<b>Figure 43.</b> Initial coalescence points and time to contact for pure and saline water slabs on porous and non-porous PTFE surfaces .....	115
<b>Figure 44.</b> Comparison of density profiles and wetting interfaces between pure water slab on non-porous and porous PTFE surfaces.....	116
<b>Figure 45.</b> (a) Illustration of slab-induced bending and pore contact angles in PTFE before and after deformation. (b) Initial and final deformation of the PTFE surface affected by the pure slab. (c) Initial and final deformation of the PTFE surface affected by the saline slab.....	117
<b>Figure 46.</b> Calculation method for pore contact angles: (a) Establishment of the cylindrical coordinate system. (b) Water/vapor interface data and pore contact angle determination for pure and saline water slabs. (c) Comparison of contact angles ( $\theta$ ) at different pore regions for pure and saline water slabs.....	119
<b>Figure 47.</b> NaCl concentration and water density distribution in saline water slabs on porous and non-porous PTFE: (a) Pore-center and pore-away regions on porous PTFE. (b) Surface-wide sampling on non-porous PTFE. (c) NaCl concentration profiles along the Z-axis. (d) Water density profiles along the Z-axis. ....	121

## **Abstract**

Molecular dynamics (MD) simulations were conducted to investigate the interactions at the interface between aqueous solutions and hydrophobic polytetrafluoroethylene (PTFE), filling significant knowledge gaps in the literature and providing novel insights into the atomic-level interactions of water with planar hydrophobic interfaces.

First, force field parameters for Titanocene Dichloride (TD) and PTFE were developed to address gaps in TD research and to validate PTFE simulations against experimental data. Subsequently, the effects of salinity and temperature on water droplet wettability were investigated, showing that PTFE's hydrophobicity increases with higher salinity and temperature. Observations revealed ion segregation away from the PTFE surface, offering crucial insights into disruptions in water structuring and changes in droplet spreading.

Lastly, a new interfacial system was designed to simulate interactions between saline and pure water slabs on both porous and non-porous PTFE membranes. This led to novel findings on vapor bridge formation, slab-induced bending, variations in pore contact angles, and ion segregation. Salinity was found to prolong vapor bridge persistence, delay coalescence, increase deformation, and result in higher ion concentrations within the porous region. These findings will deepen the understanding of water slab interactions with hydrophobic surfaces and help advance desalination and membrane technology.

# Chapter 1: Introduction

## 1.1. Motivation

The interaction between water and planar hydrophobic surfaces is crucial in many industrial and environmental processes, such as water desalination and microfluidic technologies. Contact angles measure hydrophobicity and surface wettability. Figure 1 shows a hydrophobic surface on the left with a contact angle ( $\theta$ ) greater than  $90^\circ$ , where the droplet forms a near-spherical shape, typical of water-repellent surfaces. On the right, a hydrophilic surface has a contact angle of less than  $90^\circ$ , where the liquid spreads and adheres more. Larger contact angles indicate hydrophobicity, while smaller angles indicate hydrophilicity.



**Figure 1.** Illustration of Contact Angle and Wettability: Hydrophobic vs. Hydrophilic Surfaces.

Despite extensive research on water desalination at the macroscale, atomistic level investigations remain incomplete, and water interactions at a confined planar hydrophobic interface at these scales are still poorly understood. This incompleteness has left many unresolved questions that continue to be actively debated in the literature: Does a vapor gap form between the water and hydrophobic surfaces? If so, what is the thickness of this gap, and how do ions behave near the interface under different conditions? Is the surface morphology of the hydrophobic substrate affected by the structuring of water or vapor at the interface? If so, what kind of deformations occur on the hydrophobic substrate? What are the mechanisms and kinetics of scale nucleation at the interface between saline water and the hydrophobic surface? What role do different ion species play in nucleation, and how do their size and charge affect nucleation kinetics? Does the presence of a vapor gap or surface morphology accelerate or decelerate the onset of concentration polarization? How do dynamic flow conditions affect concentration polarization near hydrophobic surfaces? The inability to address these and many other critical questions is primarily due to the limitations of experimental techniques in resolving these interfaces at the required scale and time and the significant computational complexity, cost, and time involved in designing realistic hydrophobic surfaces.

There is no study—whether experimental, atomistic simulations, or others—thoroughly addressed this incomplete literature by investigating the behavior of pure and saline water confined to a planar interface with a realistic hydrophobic substrate. In this dissertation, we addressed outstanding literature gaps by employing molecular dynamics (MD) simulations, which offer a powerful approach to studying these interfaces at the atomistic level. Our work involves the development of force field parameters to examine the

interfacial dynamics of both pure and saline water slabs on hydrophobic surfaces, both porous and non-porous. We believe the findings will provide valuable insights into the morphological characteristics of water and hydrophobic interfaces, advancing atomic-scale understanding of these interactions.

## **1.2. Research objectives and original contributions to the literature**

This section outlines the research objectives, driven by the motivation discussed earlier. Each objective aligns with the overarching goals of the thesis, highlighting novel contributions and referencing relevant literature where applicable.

The main objectives of this study, as illustrated in Figure 2, were multifaceted and aimed at providing a comprehensive understanding of PTFE interactions. First (I), force field parameters were developed, with Titanocene Dichloride (TD) and polytetrafluoroethylene (PTFE) selected as representative systems for validation to ensure accurate modeling of these materials at the molecular level. This parameterization was essential for capturing the complex behaviors and interactions required for precise simulations. Second (II), aqueous solution droplets over a PTFE surface were investigated to examine the effects of salinity and temperature on contact angles. This included analyzing how these variables influenced wettability and conducting detailed analyses involving ion distribution, density profiles, and the radial distribution function (RDF) to provide deeper insights into the structural and dynamic properties at the PTFE interface. Finally (III), the study was extended to aqueous solution slabs over a PTFE surface to investigate various interfacial phenomena, such as the formation of water vapor bridges, shifts in the center of mass, initial coalescence, partial pressure within vapor gaps, detailed density profiles of wetting interfaces, slab-induced

bending, and pore contact angle formation. NaCl concentration in distinct spatial regions was also assessed to provide insights into ion segregation and wetting mechanisms under different conditions. This comprehensive approach ensured that both nano-scale (droplets) and nano-scale (slabs) interactions were addressed.

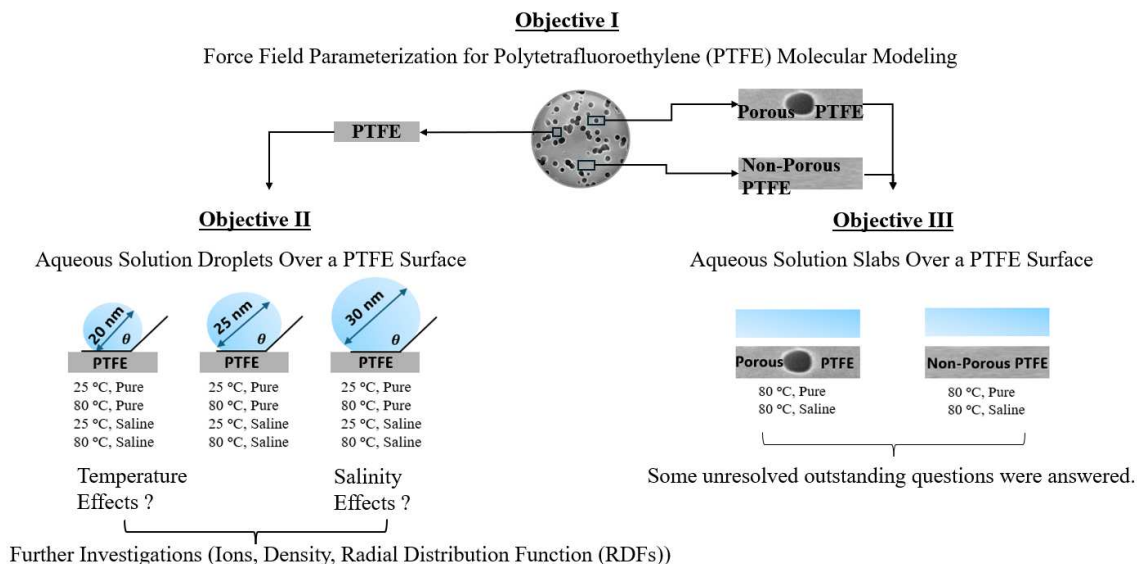


**Figure 2.** Illustration of Contact Angle and Wettability: Hydrophobic vs. Hydrophilic Surfaces.

### 1.2.1. Development of Force Field Parameters

The first objective was to develop a novel system for deriving force field parameters that accurately reproduce the potential energy landscape, ensuring that molecular simulations of structures, dynamics, and interactions closely reflect real-world behavior. This system was established and tested on bonded parameters for Titanocene Dichloride (TD) using a Chemistry at Harvard Macromolecular Mechanics (CHARMM)-compliant functional and polytetrafluoroethylene (PTFE) using an Assisted Model Building and Energy Refinement (AMBER)-compatible force field functional form.

### 1.2.1.1. TD-bonded parameters

The TD-bonded parameters were derived and validated against experimental data through power spectra and normal mode frequency analysis. The computed values closely matched experimental infrared spectra and quantum mechanical calculations, accurately predicting bond lengths, angles, and dihedrals. Further validation included explicit solvent simulations and comparisons with experimental geometries, demonstrating the robustness of the parameters in both vacuum and solvated environments. The force field development system successfully passed all validation tests.

The original contributions of this objective to the literature were as follows:

- A novel application of the simplex optimization method was developed to fine-tune Lennard-Jones force field parameters in MD simulations. The results demonstrated improved accuracy in property predictions, such as density and heat of vaporization, validated against experimental data.
- A wide range of conformational states was incorporated into the development of the force field system. This approach ensured the transferability of the parameters and improved the accuracy of predictions for the reference molecule's thermodynamic properties across various molecular weights and assemblies.
- The first CHARMM-compliant force field parameters for Titanocene Dichloride (TD), the first non-platinum-based chemotherapeutic drug candidate to undergo clinical trials, were introduced in this work. The lack of TD parameters in the existing literature hindered the computational study of this critical molecule in drug discovery. These new parameters were considered for computational molecular research on TD.



Experimental papers on TD published in prestigious journals are as follows: The TD-based complexes have emerged as promising alternatives, showing efficacy against cisplatin-resistant tumors [1] [2]. TD-based complexes have demonstrated cell-killing effects on various tumor cells with lower toxicity as the first non-platinum-based chemotherapeutic molecule to undergo phase I and II clinical trials, respectively [3] [4]. Although the TD-based structures create exciting prospects for clinical trial candidates, to date, the mechanism of action of TD binding to DNA/RNA nucleic acid sites remains undefined at the molecular level [2] [4] [5] [6]. Force field parameters developed in this dissertation should be suitable for investigating this important phenomenon.

#### **1.2.1.2. PTFE parameters**

The objective was to design a novel parameter derivation system and apply it to polytetrafluoroethylene (PTFE) to develop new transferable AMBER-compatible force field parameters to accurately capture its morphological characteristics and interfacial dynamics. These parameters were derived to ensure reliable predictions of PTFE's thermodynamic properties while addressing the shortcomings of previous models.

The original contributions of this objective to the literature were as follows:

- The first comprehensive set of AMBER-compatible force field parameters for PTFE was developed, encompassing a range of conformational states and molecular weights. This approach ensured the transferability of the parameters and improved the accuracy of predictions for the reference molecule's thermodynamic properties across various molecular weights and assemblies.

- Since previous PTFE parameter sets were developed for the gas phase, a PTFE parameter set suitable for the condensed phase was presented for the first time in the literature, offering improved thermodynamic predictions and vibrational accuracy.

The previously developed PTFE parameters in the literature were aimed at solving challenging experimental problems and reproducing experimental and theoretical data with high accuracy. However, they often had certain shortcomings, which are listed as follows: Okada et al. (1999) [7] developed an all-atom PTFE model using a Molecular Dynamics (MD) calculation package GEMS/MD for the reference molecules of perfluoroalkanes, including *n*-C<sub>3</sub>F<sub>8</sub>, *n*-C<sub>4</sub>F<sub>10</sub>, and *n*-C<sub>6</sub>F<sub>14</sub>; that work utilized the HF/6-31G ab initio method, omitting the electron correlation effect [8] [9]. The charges were derived using experimental dipole moment data. The bond, angle, and dihedral parameters were derived using the first principles method. They optimized the vdW parameters by adding artificial nonbonding potentials between atoms separated by four bonds at positions 1 to 5 (vdW<sub>1-5</sub>). They claimed that the '1-5' interactions involving long PTFE chains are significant because the attractive interactions between fluorine atoms at these positions can affect the molecule's conformation and properties. However, articles published later showed that the PTFE chain helix, affected by the artificial vdW<sub>1-5</sub> potential function between an atom and its fourth bond partner, did not adequately describe the energy landscape. While the trans conformations (*t*<sup>+</sup>, *t*<sup>-</sup>) closely matched the theoretical calculation results, the energy plot generated using the parameters failed to reproduce gauche conformations (*g*<sup>+</sup>, *g*<sup>-</sup>).

Jang et al. (2003) [10] developed a new Dreiding-type valence potential set for analyzing vdW<sub>1-5</sub> non-bond interactions and predicted helical conformations. They conducted

B3LYP/6-31G\* [11] [12] model chemistry employing the Hessian-Biased Singular Value Decomposition (HBSVD) technique [13] to derive bond, angle, torsional, and molecular vibrational frequencies parameters with Dreiding functional form by including many effects of electron correlation except treatment of dispersion. The charges were derived with Mulliken population atomic point charges (MUL) [14]. They compared energy-minimized conformations between reference data and the force field of longer perfluorinated alkanes. The authors concluded that Coulomb repulsion is the dominant helicity source for the all-trans conformations. They predicted the correct helical minima with  $t^+$ ,  $t^-$ , and helical ( $h^+$ ,  $h^-$ ) conformations. However, at the onset of bending torsional angle values, the  $g^+$  and  $g^-$  conformational sets proved unstable.

Watkins and Jorgensen (2001) [15] proposed another all-atom parameter set for PTFE molecules. They derived the force field for PTFE using OPLS functional form; their quantum mechanical data were generated using the LMP2/cc-pVTZ<sup>(-f)</sup> [16] [9] and HF/6-31G\* [8] [9] theoretical method that adds corrections to achieve superior accuracy for electron correlation without treatment of dispersion. Despite good prediction of densities and heat of vaporization, Borodin et al. (2002) [17] showed that the transferability of the  $n$ -C<sub>4</sub>F<sub>10</sub> and  $n$ -C<sub>5</sub>F<sub>12</sub> could not adequately define conformational energetics by using the same torsional parameters. Thus, Borodin et al. derived bond, angle, and nonbonded parameters using MP2/aug-cc-pvDz [18] [9] and B3LYP/D95+\* [11] [9] model chemistry. They provided a satisfactory description of the transferability for  $n$ -C<sub>4</sub>F<sub>10</sub> and  $n$ -C<sub>5</sub>F<sub>12</sub> but exhibited notably less precise thermodynamic data, encompassing density and heat of vaporization. The General AMBER Force Field (GAFF) [19] database contains parameters for numerous polymers, including PTFE. Rahul et al. [20] concluded that the standard

GAFF necessitates parameter tuning to precisely predict specific heat across various polymers, PTFE included. The new force field for PTFE developed during this dissertation overcomes many of these shortcomings and provides a powerful new tool to the molecular dynamics modeling community.

### **1.2.2. Aqueous solution droplets over a PTFE surface**

The research objective was to verify that the derived force field parameters for PTFE accurately predicted contact angle values by comparing them with experimental results, ensuring consistency with PTFE interfaces. During this process, a gap in the literature was identified—specifically, the absence of studies addressing how salinity and temperature affect the contact angle on realistically modeled hydrophobic surfaces. After the verification, the interfaces between pure and saline water on porous and non-porous hydrophobic PTFE surfaces were established and analyzed using equilibrium molecular dynamics simulations.

The original contributions of this objective to the literature were as follows:

- The first study to combine temperature and salinity effects on PTFE (hydrophobic surface): This study was one of the first to explore the combined effects of temperature and salinity on the wettability of water droplets on a realistic hydrophobic surface, providing new insights into the behavior of saline droplets.

The studies of droplets conducted on different surfaces are listed as follows: In 2009, Jae Hyun et al. [21] investigated the impact of temperature on the contact angle of a pure water nanodroplet containing 4827 water molecules on a hydrophilic titanium dioxide ( $\text{TiO}_2$ ) surface using molecular dynamics (MD) simulations. The study computed the contact

angles and analyzed the changes with temperature. It was found that as the temperature increased, the contact angle decreased, making the surface more hydrophilic. The paper explains that this behavior is due to a decrease in surface tension and hydrogen bonding as temperature rises. The authors suggested that while their study focused on  $\text{TiO}_2$  surfaces, similar investigations could be extended to other types of surfaces to understand the generalizability of temperature-dependent wettability behavior. In 2011, Christopher et al. [22] utilized MD simulations to measure the contact angle of nanodroplets containing approximately 2000 water molecules with dissolved NaCl and  $\text{MgCl}_2$ , both with and without an electric field. They used a graphite-like surface in their MD simulations and adjusted its hydrophilicity to vary from more hydrophilic to less hydrophilic by setting specific Lennard-Jones parameters. They concluded that adding salts (NaCl and  $\text{MgCl}_2$ ) increased the contact angle of nanodroplets in the absence of an electric field. However, this increase was more significant on more hydrophilic surfaces compared to less hydrophilic ones. The authors did not provide a detailed analysis of the exact mechanisms causing the change in contact angle. However, they attributed the significant increase in contact angle primarily to the rise in solution/vapor surface tension. In 2015, Jun Zhang et al. [23] investigated the wetting and evaporation of salt-water nanodroplets on hydrophilic platinum surfaces with water nanodroplets containing 5832 water molecules. They discovered that the contact angle increases with higher salt concentration due to changes in surface tensions. The authors' current study was conducted on completely smooth hydrophilic surfaces at the molecular level. They suggested that investigating the behavior of droplets on rough surfaces could provide additional insights. In 2020, Xin Li et al. [24] examined how varying concentrations of NaCl solutions influence the wettability of the

nanodroplets containing 8435 water molecules on a hydrophilic MgO(001) surface. It was found that the ordered structure of water molecules in the first hydration layer is critical in determining the wettability and that ion hydration significantly influences the orientation and ordering of water molecules, leading to a more hydrophobic surface as salt concentration increases. The authors suggested that the applicability of the findings could be enhanced by including the effect of temperature variations and generating rough surfaces.

### **1.2.3. Aqueous solution slabs over a PTFE surface**

As the first to develop this interfacing system, all the results obtained in this research are novel and make significant contributions to the literature. The analyses performed thus far encompassed several critical aspects, including the equilibration process (such as the formation of water vapor bridges and center of mass shifts), initial coalescence, partial pressure within the gap, density profiles of wetting interfaces, slab-induced bending, and pore contact angle formation, and NaCl concentration in different spatial regions.

The original contributions of this objective to the literature were as follows:

- Transient water vapor bridges were observed for the first time as intermediate structures, lowering the energy barrier to contact—an underexplored mechanism in molecular dynamics. The center of mass tracking provided a timeline, highlighting these bridges' role in system stabilization during equilibration.
- The role of partial pressure within the interfacial gap as a driving force for the initial coalescence between a water slab and hydrophobic PTFE was reported here for the first time. Peaks in partial pressure were observed as indicators of coalescence time,

opening new avenues for exploring nucleation's energetic and thermodynamic aspects at hydrophobic interfaces.

- A detailed study of wetting interfaces on porous and non-porous PTFE surfaces has provided new insights into the impact of interfacial water density on surface morphology. The variations in density distributions and wetting ranges reveal how water slabs induce structural deformations on hydrophobic surfaces, such as bending and pore contact angles.
- A comprehensive analysis of NaCl concentration in spatially defined regions was conducted, introducing a fresh perspective on concentration polarization at porous interfaces. Surface porosity selectively influenced ion accumulation, particularly in the Pore-Center region, where sharp ion gradients were observed. This unique contribution bridged a gap in the existing literature, as the effects of microscopic porosity on ion distribution across interfaces had not been addressed in most prior studies.
- This work created a new methodology for forming planar interfaces between PTFE substrates and pure and saline water films. This permitted the simulation system to form the interface under the action of atomic forces with no bias introduced by the formation method. This is critical to properly assess whether a vapor gap between the liquid and solid is predicted to be in equilibrium.
- The nature of the PTFE surface – and the resulting hydrophobic interface with water – is unique from the substrates studied in these preceding scenarios. First, the interfaces studied here exhibit pronounced hydrophobicity purely as a result of the underlying atomic interactions; that is, these are realistic, accurate atomic-scale

descriptions of hydrophobic interfaces. Perhaps more significantly, the surfaces studied here exhibit greater roughness than substrates in preceding studies, permitting a new understanding of hydrophobic interfacial structure and behavior.

### **1.3. Outline of the dissertation**

This outline provides a brief description of each chapter:

- The computational methodology chapter outlines the development of force field parameters essential for accurate molecular simulations. It covers bond lengths, angles, dihedral angles, and non-bonded interactions like van der Waals forces and electrostatics. The chapter details the parameterization of valence, charge, and van der Waals terms using quantum mechanical reference data. The simplex optimization method is used to refine Lennard-Jones parameters, ensuring experimental and QM data consistency. The chapter describes the molecular dynamics workflow, including discretization schemes, boundary conditions, and MD simulation limitations.
- This chapter introduces newly developed CHARMM-compliant force field parameters for titanocene dichloride (TD), a non-platinum chemotherapeutic candidate previously lacking such parameters. It details the parameterization process, including charge optimization, bond and angle fitting, and dihedral refinement, validated against experimental data to accurately reproduce TD's vibrational spectra and dynamics in vacuum and solvent—key for drug discovery and cancer research.



- The force field parameter for polytetrafluoroethylene (PTFE) chapter discusses the parameterization of PTFE using the AMBER force field, optimized for condensed-phase simulations. The novel parameters capture PTFE's structural and thermodynamic properties, such as density, heat capacity, and radial distribution functions. The development process includes QM calculations for charge distribution, bond angle, dihedral optimizations, and van der Waals parameter fitting through molecular dynamics. The chapter emphasizes the importance of these parameters in accurately modeling PTFE, which is crucial for studying its interactions in various environments.
- The salinity and temperature effects on hydrophobic wettability chapter presents the impact of salinity and temperature on the wettability of water droplets on PTFE surfaces. The chapter explores how changes in salinity and temperature affect the contact angles of droplets on both porous and non-porous PTFE surfaces. The findings reveal that increasing salinity and temperature increase the contact angle, which indicates a more hydrophobic surface. These results offer novel insights into the behavior of saline water at hydrophobic interfaces.
- The interfacial dynamics of water slabs on a hydrophobic membrane chapter delves into the molecular dynamics of water slabs interacting with hydrophobic PTFE membranes, focusing on the interfacial dynamics at the atomic level. It examines the formation of vapor bridges, water structuring near the surface, and the influence of surface roughness and salinity on these dynamics. The chapter provides a detailed analysis of the interactions between pure and saline water and PTFE

surfaces, offering a clearer understanding of water behavior at hydrophobic interfaces with potential applications in filtration and membrane technologies.

- The conclusions and recommendations chapter summarizes key findings, including the successful development of force field parameters for TD and PTFE and insights into water-hydrophobic surface interactions, while also identifying areas for future research.

## **Chapter 2: Computational Methodology**

### **2.1. Force field development**

Force field development is a disciplined and intricate process that is not trivial. It can be a complicated and time-consuming task, with the ultimate goal being to develop parameters that accurately reproduce the potential energy landscape of a system. This ensures that simulations of molecular structures, dynamics, and interactions closely approximate real-world behavior. Unlike kinetic energy, which depends on the molecule's translational or rotational position in space, potential energy is determined by specific interatomic relationships within the structure, including bond lengths, bond angles, dihedral angles, and non-bonded interactions such as van der Waals forces and electrostatic interactions. These relationships collectively define the molecular conformation. In our work, developing a force field required carefully determining several elements, including functional forms, the target model with atom types, reference data, the objective function, conformational states, and parameters such as charges, bonds, angles, torsional angles, and non-bonded interactions. The process involves several key steps, as shown in Figure 3:

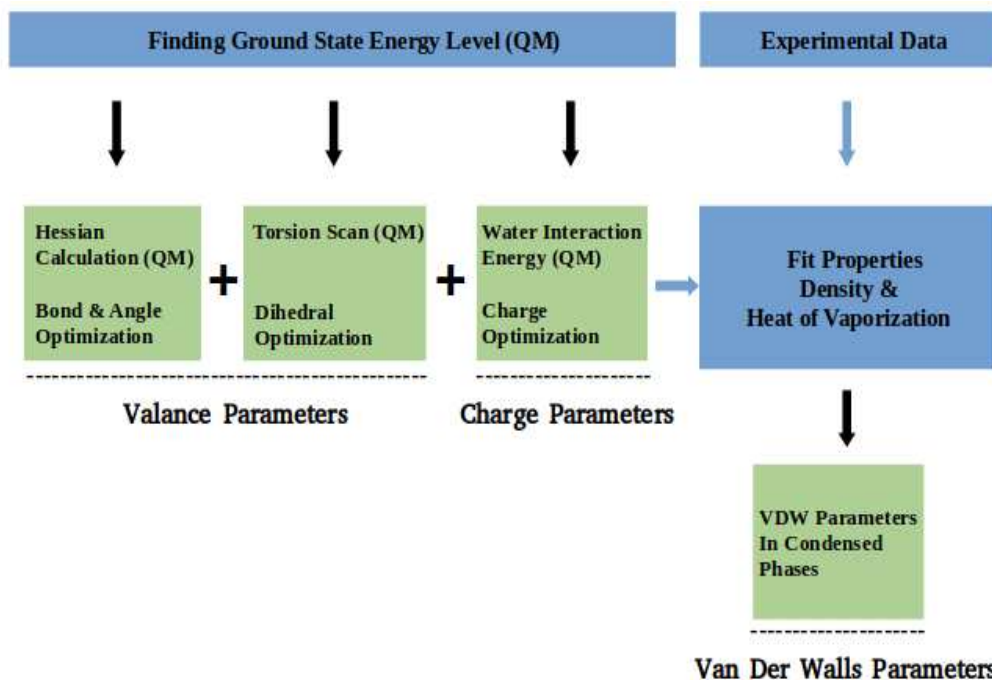


**Figure 3.** The schematic shows the path for valence, charge, and vdW parametrization.

Before parameterizing the valence and charge parameters, defining the ground state energy level is essential. This ensures the system's most stable configuration is accurately captured, providing a solid foundation for fitting bond lengths, angles, dihedrals, and charges. By establishing the ground state, we can ensure that the force field reflects the system's true equilibrium structure and energetics, leading to more accurate simulations.

#### 1. Valence Parameters:

- **Hessian Calculation (Quantum Mechanical - QM):** We perform a Hessian calculation to optimize bond lengths and angles based on quantum mechanical data, ensuring that the vibrational frequencies and force constants are accurate.

- Torsion Scan (QM): We generate a potential energy surface through a torsional scan to optimize dihedral angles and ensure the molecule's conformation responds accurately to rotations about its bonds.

## 2. Charge Parameters:

- Water Interaction Energy (QM): We model the interaction between the molecule and water using QM calculations to derive accurate charge parameters, which are crucial for representing electrostatic interactions. We also derive the charge parameters directly from QM calculations.
- Charge Optimization: The charges are fine-tuned to match electrostatic potentials or interaction energies, ensuring the molecule interacts correctly with its environment.

## 3. Van Der Waals Parameters:

- Non-bonded interactions, particularly Van der Waals parameters, are adjusted using experimental data such as density and heat of vaporization in condensed phases. This step ensured that the force field behaved appropriately in the liquid or solid states.

The simplex fitting procedure was developed to optimize the vdW parameters. The generalized optimization methodology for the fitting process in our algorithm involves creating a simplex with  $N$  vertices in an  $n$ -dimensional parameter space. The number of parameters  $n$  corresponds to the number of force field parameters optimized for the molecule in question, which may vary depending on the system's atom types and interaction parameters. Each vertex is represented by a vector  $\mathbf{x}_i = (x_{i1}, x_{i2}, \dots, x_{in})$ , where  $i$  ranges from 1 to  $N$ . For example, in the case of a molecule with  $m$  atom types, the number

of parameters  $n$  would be equal to  $2m$ , accounting for the two Lennard-Jones parameters ( $\epsilon$  and  $\sigma$ ) per atom type. If there are three atom types (as in the original case with F,  $\text{CF}_2$ , and  $\text{CF}_3$ ),  $n = 6$ . However, this value will change for any molecule with a different number of atom types. The initial simplex will always have  $N = n + 1$  vertices, representing perturbations from the starting values of the force field parameters.

**Parameter Bounding and Initialization:** Each parameter  $x_{ij}$  is bound within a range suitable for the studied molecule. For the general case, these bounds will depend on empirical or estimated parameter values for the specific atom types and interactions. In the example of Lennard-Jones parameters, these bounds might be  $(0, 5)$ , as used in the original method, but this can be adjusted based on the molecular system. A small perturbation  $\delta$  is applied to create the initial simplex vertices, which are defined as follows:

- Vertex 1:  $(x_{11}, x_{12}, \dots, x_{1n})$
- Vertex 2:  $(x_{11} + \delta, x_{12}, \dots, x_{1n})$
- Vertex 3:  $(x_{11}, x_{12} + \delta, \dots, x_{1n})$

Continue similarly for all  $N$  vertices.

**Optimization Steps:**

- **Energy Minimization:** The system energy is minimized for each vertex parameter set using the steepest descent algorithm or another energy minimization technique appropriate to the molecular system.
- **Equilibration:** Following minimization, the system is equilibrated using a series of MD simulations. The specifics of the simulation (e.g., 1 ns NVT) depend on the molecular system's characteristics, including temperature, particle count, and volume constraints.

- **Thermodynamic Property Evaluation:** The optimized parameters are evaluated by running short simulations (e.g., 20 ps NVT) to test the convergence of thermodynamic properties, such as the heat of vaporization, which can be generalized to other relevant properties (e.g., binding energy, radial distribution functions, etc.) depending on the target molecular system.

**Objective Function Calculation:** The objective function,  $f_{\text{target}}$ , quantifies the discrepancy between the computed ( $P_{\text{xn}}$ ) and experimental ( $P_{\text{target}}$ ) values for the chosen thermodynamic property (e.g., the heat of vaporization for the Lennard-Jones force field). This function is applied to each vertex and generalized to the property of interest for the molecule under study. The function is defined in Eq. (A.1):

$$f_{\text{target}}(x_n) = \left( w \left( 1 - \frac{P(x_n)}{P_{\text{target}}} \right)^2 \right)^{1/2} \quad (\text{A.1})$$

**Simplex Update Procedures:**

The vertices are updated using the standard Nelder-Mead simplex operations [25]: reflection, expansion, contraction, and shrinking. These operations adjust the parameters in the n-dimensional space to minimize the objective function, regardless of the molecular system.

1. **Centroid Calculation ( $c_j$ ):** The centroid  $c$  is calculated for the simplex, excluding the worst vertex in Eq (A.2):

$$c_j = (x_{1j} + x_{2j} + \dots + x_{(N-1)j}) / (N - 1) \quad (\text{A.2})$$

2. **Reflection ( $r_j$ ):** The worst vertex is reflected across the centroid in Eq (A.3):

$$\blacksquare \quad r_j = c_j + (c_j - x_{wj}) \quad (\text{A.3})$$

3. Expansion ( $e_j$ ): If the reflected vertex improves the objective function, an expansion step is performed in Eq (A.4):

$$\blacksquare \quad e_j = \gamma * r_j + (1 - \gamma) * c_j \quad (\text{A.4})$$

where  $\gamma$  is the expansion coefficient, typically set to 2.

4. Contraction ( $c_{oj}$ ): If the reflected vertex does not improve sufficiently, contraction is performed to bring the parameters closer to the centroid in Eq (A.5):

$$\blacksquare \quad c_{oj} = \beta * x_{wj} + (1 - \beta) * c_j \quad (\text{A.5})$$

where  $\beta$  is the contraction coefficient, typically set to  $\pm 0.5$ .

5. Shrinking ( $s_{ij}$ ): If none of the above steps improve the objective function, all vertices are shrunk towards the best vertex in Eq (A.6):

$$\blacksquare \quad s_{ij} = \delta * x_{bj} + (1 - \delta) * x_{ij} \quad (\text{A.6})$$

where  $\delta$  is the shrinking coefficient, typically set to 0.015.

This force field development methodology can be applied to any reference molecule to derive parameter sets, which can then be used in molecular simulations to generate a wide range of outputs, depending on the system being studied, the type of simulation (e.g., molecular dynamics, Monte Carlo), and the properties of interest. Common types of output obtained from molecular simulations include structural properties, thermodynamic properties, transport properties, interfacial and surface properties, dynamic properties, phase behavior, spectral properties, reaction mechanisms, and kinetics.

In this dissertation, MD simulations were used, and more information on them is provided in the next section.



## 2.2. Molecular dynamics

Molecular dynamics (MD) simulates particle motion by solving classical equations of motion, where particles interact through potential energy functions representing forces like covalent bonds, van der Waals, and electrostatic interactions—the changes in positions and velocities, revealing atomistic system dynamics.

The MD workflow involves:

- Initialization: Set particles in a simulation box with a defined force field.
- Energy Minimization: Relax the system to remove unphysical forces.
- Assigning Velocities: Assign random velocities, where the distribution of velocities directly relates to the temperature of the system.
- Equilibration: Stabilize the system under a thermodynamic ensemble.
- Production Run: Simulate dynamics over time to collect data for analysis.

### 2.2.1. Discretization schemes

In MD, time discretization is used to integrate the equations of motion over small time steps ( $\Delta t$ ), typically femtoseconds ( $10^{-15}$  s), to capture atomic vibrations and maintain stability. The Verlet and velocity-Verlet algorithms efficiently update positions ( $r_i(t)$ ) and velocities ( $v_i(t)$ ) together, as shown in Eq (A.7), and Velocities are updated using Eq (A.8):

$$r_i(t + \Delta t) = r_i(t) + v_i(t)\Delta t + \frac{F_i(t)}{2m_i}(\Delta t)^2 \quad (\text{A.7})$$

$$v_i(t + \Delta t) = v_i(t) + \frac{F_i(t) + F_i(t + \Delta t)}{2m_i} \Delta t \quad (\text{A.8})$$

The Verlet algorithm conserves energy and momentum well over long-time simulations, which is crucial for the accuracy of MD results.

### 2.2.2. Interactions between atoms

In MD, particles interact with each other according to a force field, a mathematical description of the system's potential energy as a function of atomic positions. The total potential energy  $U_{\text{total}}$  is composed of both bonded and non-bonded interactions in Eq (A.9):

$$U_{\text{total}} = \sum_{\text{bonds}} U_{\text{bond}} + \sum_{\text{angles}} U_{\text{angle}} + \sum_{\text{dihedrals}} U_{\text{dihedral}} + \sum_{\text{non-bonded}} U_{\text{LJ}} + U_{\text{Coulomb}} \quad (\text{A.9})$$

Bonded interactions describe interactions between chemically bonded atoms and include:

- Bond stretching: Modeled by harmonic or Morse potentials, representing energy changes with bond length. Angle bending: Captures deviations from equilibrium bond angles, typically using harmonic potentials.
- Dihedral angles: Describes rotations around bonds, often modeled with periodic functions

Non-bonded Interactions: These describe interactions between atoms that are not directly bonded and include:

- Van der Waals interactions: Modeled by the Lennard-Jones potential, describing short-range attractive and repulsive forces.
- Electrostatic interactions: Charged particles interact via Coulomb's law; long-range forces are calculated using methods like Ewald summation or PME to reduce computational cost.

### **2.2.3. Boundary conditions and periodicity**

MD simulations are often limited by computational resources, meaning only a finite number of particles can be simulated. To avoid edge effects and to approximate a bulk system, periodic boundary conditions (PBC) are employed. PBC means that when a particle exits one side of the simulation box, it re-enters from the opposite side, creating the illusion of an infinite system without surface effects.

In PBC, the simulation box becomes a unit cell that repeats itself infinitely in all directions. Particles interact with the nearest periodic image of other particles, ensuring that the forces calculated for each particle are consistent with an infinite, or continuum, bulk material.

### **2.2.4. Limitations of molecular dynamics**

MD is limited by computational demands for long timescales and the number of particles that can be simulated. However, advances in algorithms, parallel computing, and GPU acceleration have enhanced its ability to handle larger systems and more extended simulations.

## **Chapter 3: Force Field Parameter for Titanocene Dichloride**

### **3.1. Introduction**

In this chapter, the novel force field development system was tested to derive new CHARMM-compliant bonded parameters for Titanocene Dichloride (TD). We developed parameters using the APFD hybrid density functional theory (DFT) method, which offers advantages over existing methods by including dispersion terms. TD exhibits antiproliferative and cytotoxic effects on various tumor cells and is the first non-platinum-based chemotherapeutic drug candidate molecule to be subjected to clinical trials. The lack of TD parameters in existing literature hinders the computational study of this critical molecule in drug discovery.

### **3.2. Parameterization methods**

#### **3.2.1. CHARMM interaction model**

Developing a force field requires the determination of functional forms, a target molecular structure with atom types, reference data from either experiment or quantum mechanics

theory, an objective function for fitting, relevant molecular conformational states, and parameters in the chosen functional forms (e.g., charges, bonded, and nonbonded terms). In this study, the CHARMM functional form, which is widely accepted for biomolecular simulation, was used in Eq. (A.10) [26]:

$$\begin{aligned}
U = & \sum_{bonds} k_b(b - b_0)^2 + \sum_{angles} k_\theta(\theta - \theta_0)^2 \\
& + \sum_{dihedrals} k_\phi[1 + \cos(n\phi - \delta)] \\
& + \sum_{nonbonded} \left( \epsilon_{ij} \left[ \left( \frac{R_{min_{ij}}}{r_{ij}} \right)^{12} - 2 \left( \frac{R_{min_{ij}}}{r_{ij}} \right)^6 \right] + \frac{q_i q_j}{\epsilon_r r_{ij}} \right) \quad (A.10)
\end{aligned}$$

In the above functions, total energy ( $U$ ) is expressed as a summation of various energy terms from bond stretching, angle bending, torsion (dihedral), angle distortion, and nonbonded terms: Lennard-Jones (12-6) and electrostatic interactions.  $k_b$ ,  $k_\theta$  and  $k_\phi$  denote force constants for bond, angle, and torsion. The  $b$  and  $b_0$  denote the instantaneous and equilibrium separation distances between two bonded atoms. The  $\theta$  and  $\theta_0$  are the instantaneous and equilibrium bond angles formed by two bonds to the same central atom. The dihedral multiplicity and phase angle are denoted by  $n$  and  $\delta$  (their values favor specific structures among groups of four atoms);  $\phi$  denotes the instantaneous dihedral angle. The Lennard-Jones (LJ) energy minimum for the nonbonded atom pair  $ij$  is determined by  $R_{min_{ij}}$ , and the van der Waals (vdW) energy well depth is denoted by  $\epsilon_{ij}$ . In the last non-bond term,  $q_i q_j$  are atomic charges,  $\epsilon_r$  is the effective dielectric constant,

and  $r_{ij}$  represents i to j atom distance. Having determined the functional form, a target molecular structure with atom types was modeled in .pdb formatted files containing twenty-two bonds, thirty-one valence angles, and forty torsion terms using the Avogadro molecular editor [27]. The atom types were provided by the ParamChem web server [28]. Since these tools are based on databases of molecular fragments of molecules and compounds that are pre-parameterized for a given force field, ParamChem is highly accurate in determining CHARMM atom type [29]. Then, the atom types were assigned to the molecule using the Molefacture Tool in Visual Molecular Dynamics (VMD) package [30]. For the Lennard Jones (LJ) parameters of C, H, and Cl atoms in the TD molecule, very similar atom types available in the CGenFF databases were used [31]. The LJ parameter for the titanium atom was taken from ref. [21]. The parameterization procedure first started with geometry optimization. The water interaction energy was then calculated at the QM level using the ffTK optimization method to determine the charge parameters. Then, the Hessian calculation was performed at the QM level to obtain the bond and angle parameters. Dihedral optimization was performed at the QM level with a Torsion Scan to determine the dihedral parameters. QM optimization of bond, angle, and dihedral parameters was performed in Gaussian software [32], and molecular mechanics (MM) geometry optimization of bond, angle, and dihedral was performed in NAMD software [33] during ffTK optimization. Finally, the parameter sets in CHARMM functional forms ( $k_b; k_\theta; b_0; \theta_0; k_\phi; \varepsilon_{ij}; R_{min_{ij}}; q_i; q_j$ ) have been successfully identified.

The optimization of the TD molecular structure was carried out with the APFD theoretical method in Gaussian 16, using a series of basis sets: initially, 6-311G(2d,p), followed by 6-31(d), then 6-311+G(2d,p), and concluding with 6-311+G(d,p) [34]. Each basis set

included six primitive orbital basis functions, three basis functions per valence orbital, and one primitive function (6-31). Additionally, some of the basis sets included the following functions: d-polarization (heavy atoms), p-polarization (hydrogen), and diffusion functions (+) on heavy atoms [35]. The aim was to identify the most accurate model chemistry for the molecule by comparing it to experimentally measured properties. Once the most accurate basis sets were identified, they were used consistently in all steps of the parameterization process.

### **3.2.2. Partial charge optimization**

The partial charge parameters were obtained in ffTK by interacting the TD molecule with explicit TIP3P water [36]. Thirteen different initial interactions were defined using the ffTK algorithm to form hydrogen bonds, one for each water molecule with the target atom of TD as hydrogen (acceptor) or oxygen (donor). The Gaussian input files generated by the ffTK algorithm were visually checked before the QM calculation to avoid misidentified orientation or overlapping of water molecules. Then, QM optimization was conducted using the APFD/6-31(d) model chemistry to refine the interaction distance, energy, and dipole moment between each explicit water molecule and target atom. This optimization provided thirteen QM-level data sets of equilibrium distance ( $d_{QM}$ ), interaction energy ( $E_{QM}$ ), and dipole moment ( $\mu_{QM}$ ) for fitting and optimization of partial charges. QM-derived data sets were imported into ffTK for MM charge fitting. Before starting the fitting procedure, trial values for each atomic charge in the molecule were defined by the ffTK algorithm. However, the charge of the hydrogen atoms bound to cyclopentadienyl was manually kept at the standard value of  $0.09^+$  and was not changed during the fitting

procedure. For the MM charge fit, using the trial atomic partial charges and ffTK nonbonded energy functions, MM optimized distances, energies, and molecular dipole moment were measured for comparison with each QM-derived data set. This comparison was made with the objective function of ffTK. The trial atomic partial charges were then modified for every corresponding MM interaction energy, which varied by distance to ensure that energy differences of each  $E_{\text{QM}}$  and  $E_{\text{MM}}$  agreed within the proposed convergence criterion of 0.2 (kcal/mol). The final optimized charges were obtained when all interaction energy differences were below the proposed 0.2 (kcal/mol) convergence criterion.

### 3.2.3. Bond and angle optimization

In the TD molecule, 22 bonds and 31 angle combinations were detected. In order to optimize the MM force field parameters, the fit process was performed using the QM-derived reference data set. First, the TD molecule was optimized using APFD/6-31(d) theory to obtain the QM-derived equilibrium data set of the bonds and angles. Second, the force constants were obtained using the Hessian matrix, which captures the second-order partial derivatives of a function's potential energy surface relative to atomic pair coordinates. Trial MM geometry and PES were adjusted to match QM data using parameters from ffTK. Fitting utilized Mayne et al.'s [37] objective function, with Guvench et al.'s [38] simulated annealing for optimization. The equilibrium bond ( $r_{eq}$ ), equilibrium angle  $\theta_{eq}$ , bond force constant ( $k_b$ ) and angle force constant ( $k_\theta$ ) sets were defined until the final objective function value stopped decreasing in subsequent iterations. In general,



deviations in each QM and MM value were accepted up to 0.03 Å for bond lengths and up to 3° for angle values.

#### **3.2.4. Dihedral optimization**

Data from dihedral scans of H-C-C-H, H-C-C-C, and C-C-C-C were acquired using APFD/6-31(d) theory to optimize their parameters in QM PES studies. Torsion scans were automatically selected using the ffTK algorithm, and manual adjustments set torsion values to  $n=2$  and  $\delta=180$ , ensuring cyclopentadienyl rings remained flat [39]. These scans were used to optimize the  $k_\phi$  force constants. Mayne et al.'s [37] objective function evaluated energy barriers and MM force constants' equilibrium angles. Guvench et al.'s [38] simulated annealing optimized this function. Iterative parametrization refined the RMSE. It is recommended in the literature for this value to be below 0.5 kcal/mol [26].

### **3.3. Parameterization results**

Table 1 demonstrates the influence of various basis set configurations on the results of geometry optimization, providing a comprehensive comparison of bond lengths and angles across different regions of the molecular structure. In particular, the table focuses on the 1C-11H and 1C-2C bond lengths, offering insights into how these distances are affected by the choice of basis set. Furthermore, it highlights the 21Ti-23Cl bond length and the 22C-21Ti-23Cl bond angle, critical for understanding the molecular coordination environment around the titanium atom. This comparison emphasizes the sensitivity of bond distances and angles to the level of theory used. It sheds light on the accuracy of different

computational methods in predicting molecular geometries, particularly in complex systems involving transition metals and halides.

**Table 1.** Comparison of experimental and predicted structures of assigned bonds (Å) and angles (°) for various basis sets.

Assignments <sup>a</sup>	Experiment <sup>b</sup>	6-311G (2d,p)	6- 31(d)	6- 311+G (2d,p)	6- 311+G(d,p)
1C – 11H	*1.07	1.07	1.07	1.07	1.07
1C – 2C	*1.42	1.42	1.42	1.42	1.42
21Ti – 23Cl	*2.25	2.27	2.25	2.28	2.25
22Cl-21Ti-23Cl	*100.0 °	102.5 °	101.4°	102.9°	103.4°

<sup>a</sup>The assignments are shown schematically in Figure 1a. <sup>b</sup>Experimental measurement data were obtained from ref [35].

The diffusion function (+) widens the angle involving Cl-Ti-Cl, and the second polarization function (d) lengthens the Ti-Cl bond. The result with the 6-31(d) basis set exhibits high accuracy compared to results from the literature, and it provided good starting reference data for the parameterization of bonds, angles, and dihedrals.

### 3.3.1. Charge parameters

New CHARMM-compatible charge parameters were computed, capable of capturing both the TD and intermolecular energies of water. In total, thirteen independent explicit TIP3P water molecules were assigned to interact with the optimized TD molecule, either with the oxygen atom or the hydrogen atom of the water, as illustrated in Figure 4a. Hydrogen atoms (H11 to H20) from the cyclopentadienyl group, colored white, were made to interact with the water's oxygen atom. A pink-colored Titanium (Ti21) atom was made to interact with the water's oxygen atom, while cyan-colored Chlorine atoms (Cl22; Cl23) were assigned

to interact with its hydrogen side. The energies for each interaction between QM and MM calculations were then determined, starting with a preliminary set of charges refined toward the target value.

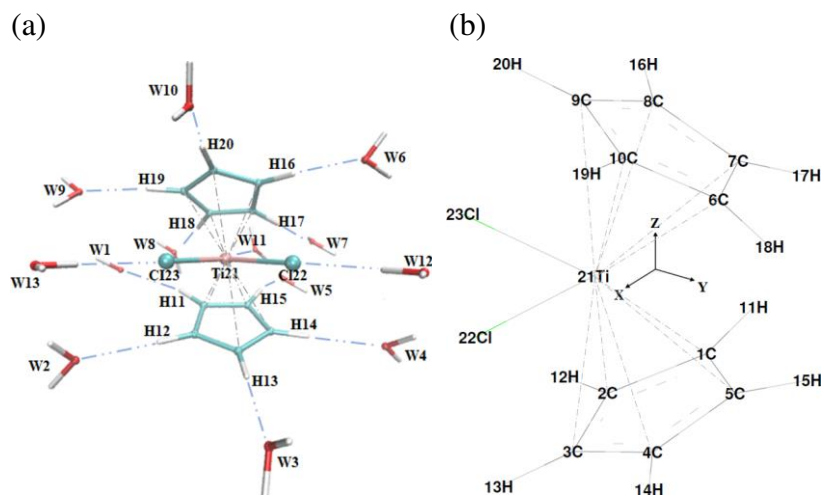


**Figure 4.** (a) Optimized water interactions between the explicit TIP3P water and TD molecule. (b) Schematic representation of atom labels used for the final partial charges shown in Table 3.

Once the distance and energy of the molecular mechanics (MM) interaction (dMM and EMM) for each site were consistent, the interaction energies between the system and a single explicit water molecule were calculated by subtracting the energy of the TD-water complex from the combined energies of the individual TD and water molecules. This approach ensured accurate evaluation of TD-water interactions, aligning with experimental and quantum mechanical data.

**Table 2.** The energies of interactions (kcal/mol) between the explicit TIP3P water and TD molecule. The MM interaction energies were calculated using the ffTK objective function.

Interaction Energy	E <sub>QM</sub> (kcal/mol)	E <sub>MM</sub> (kcal/mol)	Energy Diff.
W1 – H11	-4.257	-4.336	-0.079
W2 – H12	-2.756	-2.671	0.085
W3 – H13	-2.713	-2.649	0.064
W4 – H14	-3.424	-3.545	-0.121
W5 – H15	-4.633	-4.493	0.140
W6 – H16	-3.520	-3.432	0.088
W7 – H17	-4.848	-4.680	0.168
W8 – H18	-4.226	-4.341	-0.115
W9 – H19	-2.844	-2.780	0.064
W10 – H20	-2.836	-2.767	0.069
W11 – Ti21	0.036	0.034	-0.002
W12 – Cl22	-4.532	-4.683	-0.151
W13 – Cl23	-4.500	-4.684	-0.184

According to the standards set in CgenFF, the interaction energy between water and hydrogen or oxygen atoms should not surpass 0.2 (kcal/mol), and distances within 0.1 Å. Once these standard convergence criteria were met, the final partial charges listed in Table 3 were calculated. The schematic representation is shown in Figure 4b.

**Table 3.** The names and charges of the atoms in TD.

Atom	Charge	Atom	Charge
1C	- 0.144	8C	- 0.184
2C	- 0.228	9C	- 0.221
3C	- 0.192	10C	- 0.165
4C	- 0.212	21Ti	+ 1.995
5C	- 0.078	22Cl	- 0.578
6C	- 0.206	23Cl	- 0.566
7C	- 0.121	H	+ 0.090
Total charge:0			

### 3.3.2. Bond and angle parameters

The bonded force constants underwent optimization using the Hessian internal coordinate calculation method via the ffTK tool. The potential energy within the MM framework was computed using optimized partial charge via the NAMD software. The optimization iterations for generating the MM potential energy were utilized until the ffTK objective function value ceased decreasing compared to the previous one. The bond lengths and angles were compared with the literature convergence values at the final target value, as illustrated in Figure 5 (a and b).

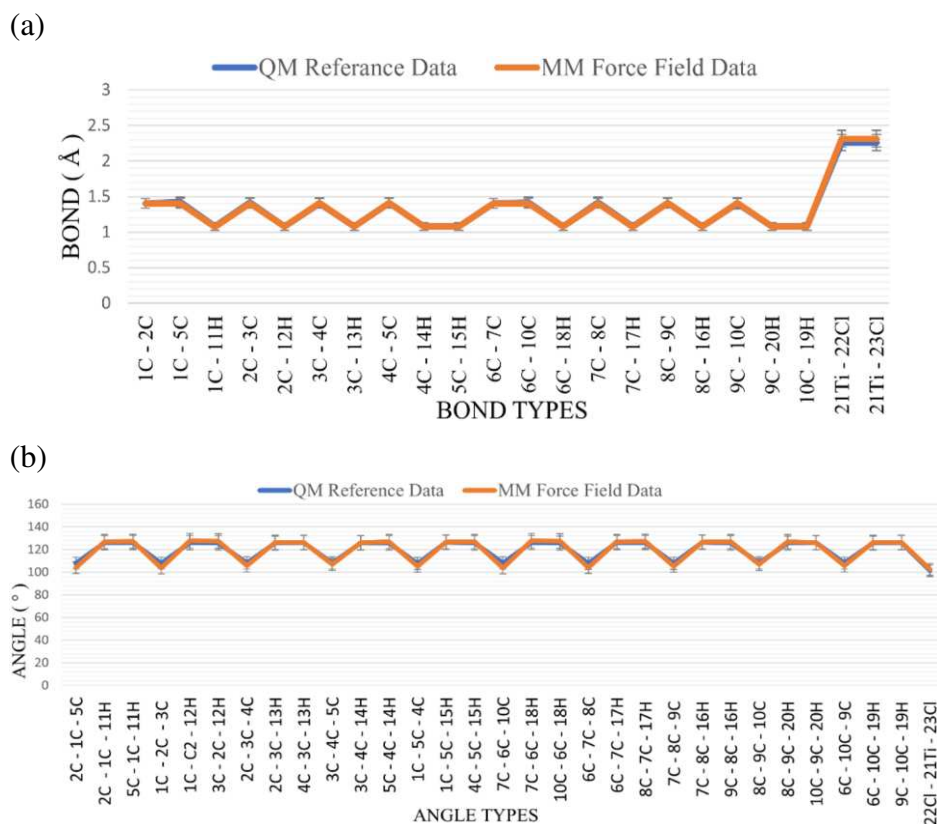


**Figure 5.** The comparison of QM reference data and MM force field data for (a) the bond fitting and (b) the angle fitting.

The bond pairs did not exceed 0.03 Å deviation in all cases, and the non-linear angles did not exceed 5° deviation as these values conform to the standards set by CgenFF. The final bond and angle parameters shown in Tables 4 and 5 were then calculated.

**Table 4.** Optimized bond parameters for TD.

Bond parameters	$K_b \left( \text{kcal/mol/\AA}^2 \right)$	$b_0 \left( \text{\AA} \right)$
C – C	429.5413	1.4052
C – H	366.7862	1.0752
Cl – Ti	103.4945	2.2490

**Table 5.** Optimized angle parameters for TD.

Angle parameters	$K_\theta \left( \text{kcal/mol/rad}^2 \right)$	$\theta_0 \left( ^\circ \right)$
C – C – C	73.9923	107.9838
C – C – H	29.4156	126.8217
Cl – Ti – Cl	135.8504	101.4349

### 3.3.3. Dihedral parameters

Dihedral parameter sets, as listed in Table 6, were obtained from QM-derived PESs using APFD/6-31(d) model chemistry. The ffTK algorithm automatically identified the dihedrals to be scanned, and these dihedrals were scanned in both directions starting from optimized geometry with a step size of 5 degrees and 6 steps per scan using Gaussian software. The QM-derived PESs data generated by these scans were imported back into ffTK to reconstruct the entire torsional profile. A simulated annealing protocol [37] optimized the MM energy for all scanned dihedrals, corresponding to each torsional energy profile in the

QM dihedral scan. While the optimization was being carried out, the force constant  $k_{\phi}$  was the only parameter that was continuously varied.

The equilibrium torsion values were fixed manually to  $n = 2$ , and  $\delta = 180$ , to preserve the planarity of the cyclopentadienyl rings. The RMSE of the optimized dihedral parameters was calculated as 0.47 (kcal/mol). The refined result shows that the MM data agrees well with the relevant QM data, considering the CHARMM's convergence criterion of 0.5 kcal/mol.

**Table 6.** Optimized dihedral parameters for TD.

Dihedral Parameters	$K_{\phi}$ (kcal/mol)	$n$	$\delta$
C – C – C – C	5.1379	2	180
C – C – C – H	1.6300	2	180
H – C – C – H	0.1489	2	180

The percent error values of the reference equilibrium dihedral angles measured using ffTK remained below 5% compared to QM, as in the standard set by the CGenFF protocol.

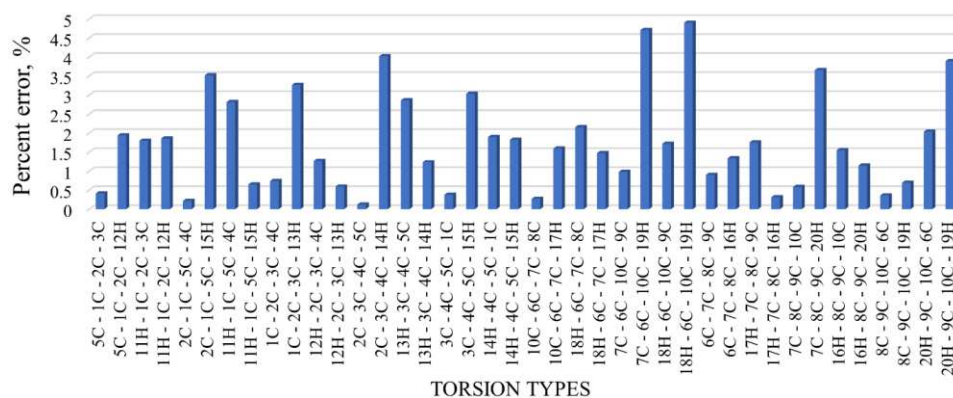


**Figure 6.** The percent error of the equilibrium QM and MM angles for all dihedral combinations is shown.

### 3.4. Validation methodologies and results

Although achieving agreement between force field parameters and ab initio data is crucial, this alignment alone does not guarantee accurate parameter optimization. MD simulations should also evaluate how well the compound dynamics compare with corresponding experimental data. As there is limited experimental data on TD available in the literature, we used three distinct methods to validate the optimized force field parameters for the TD molecule.

#### 3.4.1. Power spectrum

The velocity density of states (VDOS) or power spectrum was obtained by performing a Fourier transform of the VDOS and compared with the experimental infrared spectrum. This process provides valuable information on the typical frequencies of the motion of bonds, angles, and dihedrals, providing insight into the optimized parameters' accuracy [40]. The power spectrum is calculated using data from an MD simulation according to [41] as follows in Eq. (A.11):

$$P(\omega) = \int_{-\infty}^{+\infty} C(n) e^{i\omega t} dt \quad (\text{A.11})$$

$C(n)$  represents the normalized autocorrelation function (ACF). The ACF calculation was executed using in the equation provided following Eq. (A.12):

$$C(n) = \sum_{i=1}^m v_k(i) v_k(i+n) / \sum_{i=1}^m v_k(i) v_k(i) \quad (\text{A.12})$$



The  $n$ -th point in the discrete ACF is represented by  $C(n)$ , and the  $v_k$  are individual wave vectors of the corresponding velocities. The  $v_k$  are defined in Eq. (A.13):

$$v_k(t) = \sum_j u_j(t) e^{ikx_j^0} \quad (\text{A.13})$$

The velocity vector of the  $j$ -th atom is represented by  $u_j$ , where  $k = \frac{2\pi}{\lambda}$  denotes the wave vector, and  $x_j^0$  is defined as the equilibrium vector of the  $j$ -th atom. MD simulations were carried out with GROMACS [42] to calculate power spectra by implementing optimized force field parameters. The simulations utilized periodic boundary conditions (PBC) with 50 TD molecules in a 100 Å edge-length cubic box. Lennard-Jones potentials were utilized to calculate short-range interactions, with a cutoff of 10 Å and a dispersion correction for energy and pressure. At each timestep, neighbor lists with a 10 Å cutoff were generated for nonbonded interactions, and the PME method calculated electrostatics [43]. The energy was minimized in 15000 steps using the steepest descent. Then, the NPT ensembles were conducted for 1.2 nanoseconds to achieve a correct box length/density. The Nose-Hoover thermostat kept the temperature at 298.15 K and pressure at 100 kPa [44] using the Parrinello-Rahman method [45]. This was followed by NVT simulations at  $T = 300$  K, and the simulation box size used matches the average size observed in the preceding NPT simulation for equilibrium property acquisition. The power spectra were calculated by performing an NVT simulation with a 2 fs timestep; the simulation ran for 1000 ps, consisting of 700 ps of equilibration followed by 300 ps of analysis time.

We calculated the TD power spectrum or velocity density of states (VDOS) by analyzing autocorrelation functions of the average atomic velocity using MM-optimized parameters;

velocity autocorrelation results are depicted in Figure 7a. The VDOS results were compared with the experimental infrared spectrum in Figure 7b. Although the intensities disagreed with specific values, the peak positions of the calculated VDOS exhibited good agreement with the experimental infrared spectrum obtained from ref [46].

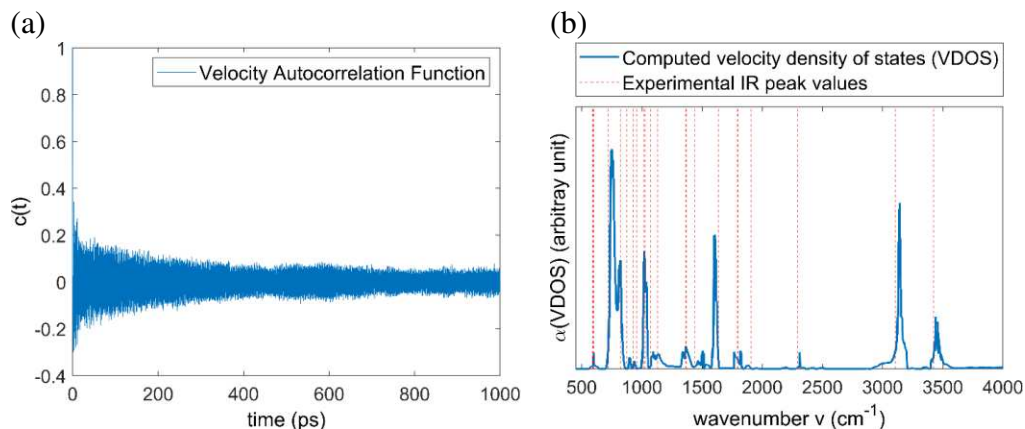


**Figure 7.** (a) Velocity autocorrelation function. (b) Velocity density of states (VDOS) or power spectrum of TD in the range 0 to 4000  $\text{cm}^{-1}$  calculated from the velocity autocorrelation function; red dashed lines show the experimental infrared spectrum.

The experimental peak values shown as red dashed lines in Figure 7b were compared in detail in Table 7 with the calculated values obtained from MD simulations. Table 7 also displays the vibrational band assignments established through experimental methods to identify the portion of the molecules linked to a specific mode frequency. If a frequency could not be assigned experimentally, we used a hyphen in the assignment section. Additional notations were included alongside the observed vibrational frequencies in experimental data to denote their respective intensities. As an example of the discrepancies observed in peak intensity, the 1440  $\text{cm}^{-1}$  vibrational band was experimentally calculated as vigorous intensity; however, the corresponding peak observed from MD simulation

results was at  $1461\text{ cm}^{-1}$ , exhibiting a relatively low intensity. Despite the few discrepancies in intensity, the simulation data agree remarkably well with the IR experimental study regarding peak positions (deviations  $< 25\text{ cm}^{-1}$ ) for the vibrations occurring below the  $2500\text{ cm}^{-1}$  band formed by C-H, C-C stretching, and bending. The highest deviation ( $45\text{ cm}^{-1}$ ) occurred above the  $2500\text{ cm}^{-1}$  band, obtained at C-H stretching modes for the vibration value of  $3105\text{ cm}^{-1}$ , contrasting the value of  $3150\text{ cm}^{-1}$ .

**Table 7.** Comparison of theoretical VDOS spectra with experimental IR spectrum of TD molecule.

assignments <sup>a</sup>	calc. <sup>b</sup>	expt. <sup>c</sup>	assignments <sup>a</sup>	calc. <sup>b</sup>	expt. <sup>c</sup>
— — — —	3460	3425 v	$\delta(\text{C} - \text{H})$ o.p	1094	1071 w
$\nu(\text{C} - \text{H})$	3150	3105 m	— — — —	1037	1028 s
— — — —	2311	2293 vw	$\delta(\text{C} - \text{H})$ i.p	1012	1016 s
— — — —	1887	1906 vw	— — — —	949	956 w
— — — —	1818	1798 vw	$\delta(\text{C} - \text{C})$ i.p	937	928 w
— — — —	1765	1793 vw	$\delta(\text{C} - \text{H})$ o.p	888	873 m
— — — —	1608	1637 vw	$\delta(\text{C} - \text{H})$ o.p	821	822 vs
$\nu(\text{C} - \text{C})$	1461	1440 s	— — — —	745	721 w
— — — —	1363	1370 m	— — — —	606	603 vw
$\nu(\text{C} - \text{C})$	1356	1366 w	$\delta(\text{C} - \text{C})$ o.p	598	595 vw
ring breath (Cp)	1143	1131 m	— — — —	586	590 vw

<sup>a</sup>The vibration assignments were obtained from experimental ref [46]. <sup>b</sup>The peak band positions ( $\text{cm}^{-1}$ ) were computed from the MD trajectory. <sup>c</sup>Experimental peak values of the infrared spectrum were obtained from ref [47].

Notations:  $\nu$  (bond-stretch); o.p (out of plane); i.p (in-plane);  $\delta$  (bend, angle deformation); Intensity (v corresponds to "very," s indicates "strong," m stands for "moderate," and w represents "slight"); Cp (cyclopentadienyl ring).

### 3.4.2. Explicit solvent simulations

The MD simulations were utilized to test the optimized parameter sets against QM or experimental data. A cubic box with 30 Å edges housed a TD molecule and 100 TIP3P water molecules, prepared using PyMOL and simulated with GROMACS. Energy is minimized with the steepest descent (5000 steps), then NPT equilibration (300 K, 1 bar, 200 ps) for density stabilization is conducted. The last 10 ns simulations were run with an NVT ensemble at 300 K; recording coordinates every 10 ps, yielding 1000 snapshots for analysis.

The optimized parameter sets were tested to see if the model could validate QM results and experimental bonded values. Therefore, the 10-ns MD simulations in an explicit solvent were utilized, and vibration measurements were recorded at 10 ps intervals. The histograms were then constructed by taking the average bond angle combinations in the molecule every 10 ps. The obtained data were organized into histograms, shown as filled blue circles in Figure 8, and fitted to a Gaussian distribution used to define the maximum intensity distribution, shown as a red line in Figure 8.

**Table 8.** Comparison of experimental, QM optimized, MD probability distributions of angles and bond distances.

Methods	C – C – H ( ° )	C – C – C ( ° )	Cl – Ti – Cl ( ° )	Ti – Cl ( Å )
Gaussian fit*	125.50	108.43	101.11	2.2577
QM method**	126.39	107.18	101.62	2.2495
Experiment***	126.00	108.00	100.00	2.2500

\*The Gaussian probability density function was fitted to a series of points obtained from the MD simulations. \*\*The optimum values for the assigned angles and bond length were calculated in APFD/6-31(d) model chemistry from Gaussian software. \*\*\*Experimental measurement data were obtained from electron and neutron diffraction studies [48].

The values of the MD probability distributions are compared with the experimental and QM-optimized values in Table 8. The QM and experimentally derived angle and bond measurements align within a Gaussian distribution with 98% accuracy, showing that the parameters effectively capture the TD's true shape.

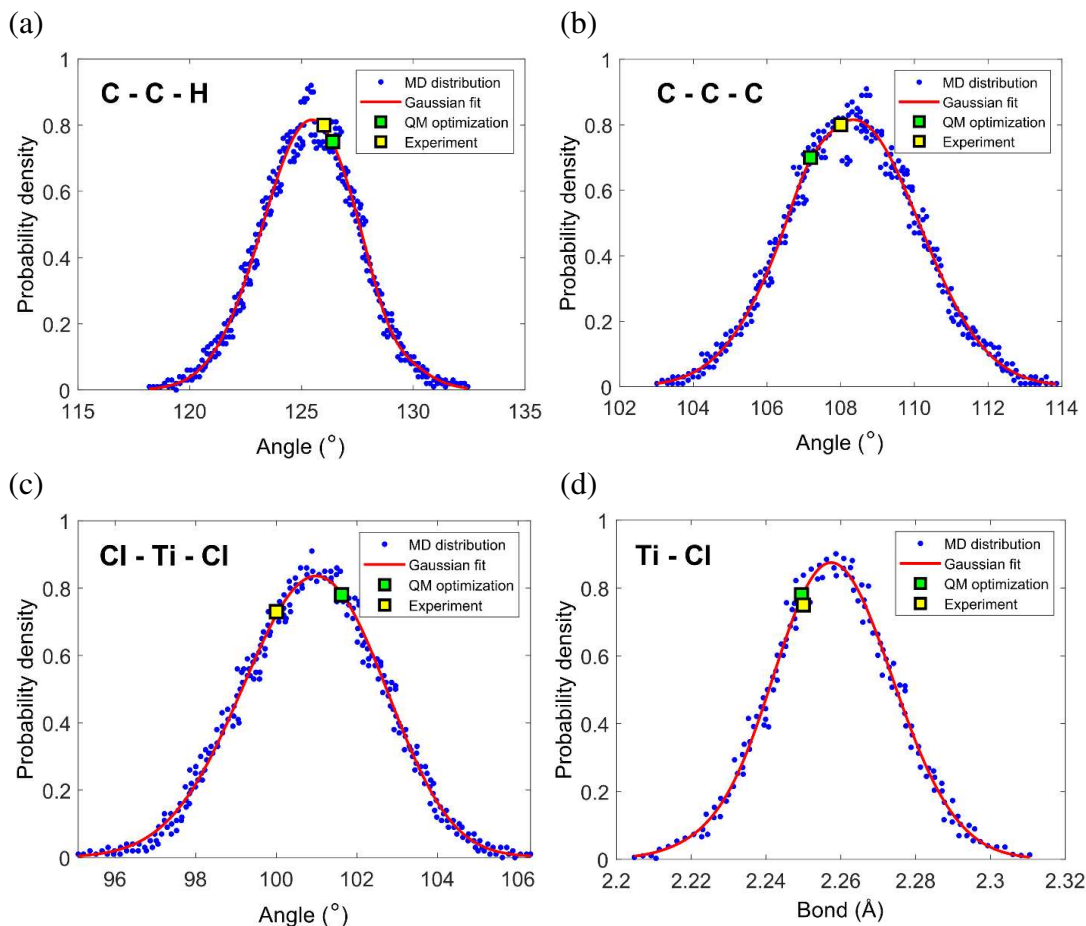


**Figure 8.** Ti - Cl bond angle (d) and three angle values with the distances (a)(b)(c) were compared through a 10-ns explicit MD simulation to those resulting from QM optimum value and experimental data [48]. The horizontal axis displays the bond distance (in Å) or angle (in °) values, while the vertical axis shows 1000 instances of the probability density for a given measurement.

### 3.4.3. Normal mode analysis

Our final check for the optimized parameters' precision was through normal mode analysis. The method for obtaining the vibrational modes and frequencies differs from that used for the power spectrum, as it involves diagonalizing the mass-weighted Hessian  $H$  in Eq. (A.14)(A.15), the  $3N \times 3N$  matrix where  $N$  denotes the number of atoms.

$$\begin{aligned} R^T M^{-1/2} H M^{-1/2} R &= \text{diagonalization } (\lambda_1, \dots, \lambda_i) \\ \lambda_i &= (2\pi\omega_i)^2 \end{aligned} \quad (\text{A.14})$$

where  $T$  is the transpose, matrix  $R$  consists of eigenvectors represented by columns, while the corresponding frequencies are denoted by  $\omega_i$  and eigenvalues by  $\lambda_i$ , and  $M$  contains the atomic masses.

$$H_{ij} = \frac{\partial^2 V}{\partial x_i \partial x_j} \quad (\text{A.15})$$

The equation represents an element  $H_{ij}$  of the Hessian matrix, defined as the second-order partial derivative of a scalar function  $\partial^2 V$ , typically potential energy, with respect to the variables  $x_i$  and  $x_j$ . This matrix element provides information about how the potential energy changes as the variables change, reflecting the local curvature of  $V$ . The MM normal mode analysis [49] was performed on a TD using the series of steps of the GROMACS. The first step was to minimize the energy of the molecule. Then, the minimized conformation structure of the TD was used to calculate the Hessian matrix. The

diagonalization of the mass-weighted Hessian was then used to diagonalize and rank the normal modes according to their frequencies. Figure 7 depicts MM frequencies plotted against QM frequencies, with a red line of slope 1 indicating definitive agreement. The frequency of 69 MM was determined in the TD molecule with 23 atoms. As can be seen, most of the corresponding MM normal mode frequencies agree well with the QM normal mode frequencies; an agreement is less satisfactory for the high-frequency vibrations between  $3000\text{ cm}^{-1}$  and  $4000\text{ cm}^{-1}$ .

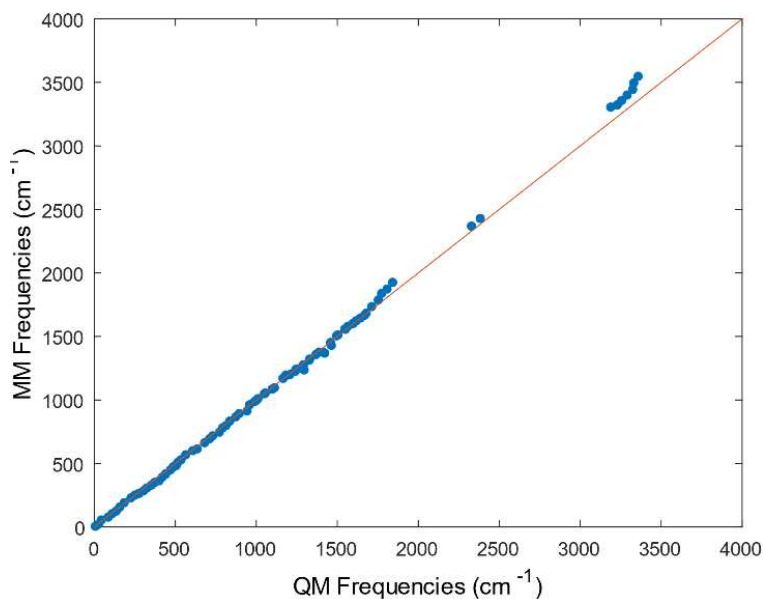


**Figure 9.** Comparison of normal mode analysis between frequencies produced by QM-APFD/6-31(d) and MM-CHARMM for titanocene dichloride.

The standard deviation and correlation coefficient ( $R^2$ ) between MM and QM were calculated to be 6.23% and 0.994, respectively. The standard deviation was calculated considering frequencies below  $3000\text{ cm}^{-1}$ . The error is below the threshold value of 6.4%, the deviation value reported by Vanommeslaeghe et al. [26] as CHARMM protocol in the literature.

## **Chapter 4: Force Field Parameter for Polytetrafluoroethylene**

### **4.1. Introduction**

In this chapter, we developed new transferable parameters for polytetrafluoroethylene (PTFE) compatible with the Assisted Model Building with Energy Refinement (AMBER) force field by including many conformational states to improve accuracy. The Austin-Frisch-Petersson functional with dispersion (APFD) hybrid density functional theory (DFT), advantageous for treating dispersion, was used to obtain quantum mechanical reference data. The restrained electrostatic potential (RESP) method was used to compute the partial charges. The bond, angle, and dihedral parameters were obtained via Paramfit software fitted to quantum mechanical data. The optimization of Van der Waals (vdW) parameters was obtained in the condensed phase through molecular dynamics simulations and the simplex method. These parameters were transferred to various molecular weights of PTFE assembly systems to calculate the density, radial distribution functions (RDFs), power spectrum, and specific heat capacity. The highest percent error in density was 1.4% for the modeled PTFE ensembles. The calculated vibrational spectrum peaks closely matched experimental peaks with a maximum wavenumber deviation of 19  $\text{cm}^{-1}$ . The



highest percent error to specific heat capacity was 5%. These results represent a significant improvement over pre-existing potentials in the literature and provide parameters that can be used to model PTFE in many existing simulation codes.

## 4.2. Parameterization methods

### 4.2.1. AMBER interaction model

The AMBER interaction model, presented below, describes the potential energy of a molecular system in Eq. (A.16) [19].

$$\begin{aligned}
 E = & \sum_{bond} K_r (r - r_{eq})^2 + \sum_{angle} K_\theta (\theta - \theta_{eq})^2 + \sum_{torsion} \frac{v_n}{2} [1 + \cos(n\phi - \gamma)] \\
 & + \sum_{nonbond}^{i < j} \varepsilon_{ij} \left[ \left( \frac{\sigma_{ij}}{r_{ij}} \right)^{12} - 2 \left( \frac{\sigma_{ij}}{r_{ij}} \right)^6 \right] + \sum_{nonbond}^{i < j} \frac{q_i q_j}{r_{ij}}
 \end{aligned} \tag{A.16}$$

$K_r$ ,  $K_\theta$  and  $v_n$  represent the force constants for the bonded terms.  $r_{eq}$  is the equilibrium bond length;  $\theta_{eq}$  is the equilibrium bond angle. The  $n$  is the multiplicity of the associated torsion angle,  $\gamma$  is the phase angle, and  $\phi$  is the equilibrium torsion angle.  $\varepsilon_{ij}$  is the energy well depth of the van der Waals (vdW) interaction,  $r_{ij}$  is the distance between non-bonded atoms  $i$  and  $j$ , and  $\sigma_{ij}$  is the distance parameter of the Lennard-Jones 12-6 function. In the final nonbonding term,  $q_i, q_j$  represent atomic charges. In brief, the parameterization was performed using the following procedure: preliminarily, the atom types and the  $n$ -C<sub>4</sub>F<sub>10</sub> reference molecule were modeled in .pdb format files using the Avogadro Molecular Editor [50]. Then, the parameter file for the force field was prepared, including all parameters to

be fitted. The conformational sets were generated using Gaussian 16 [32] by specifying which dihedral angle to scan while relaxing other coordinates from an optimized *n*-C<sub>4</sub>F<sub>10</sub> reference molecule; it was ensured that conformations spanned a considerable range in energy, including a few at high energy. The paramfit tool was employed to fit all the parameters in the conformational sets of bonded terms. Then, the Lennard-Jones (LJ) potentials were optimized using experimental data of the *n*-C<sub>4</sub>F<sub>10</sub> reference molecule. Details about each of these steps are provided in the following sections. The quality of the parameter set was thoroughly examined and evaluated to ensure reasonable accuracy was obtained for all generated structures across the sampled conformational space.

#### **4.2.2. Charge optimization**

The atomic partial charges were obtained from QM wave functions and fitted to electron density and potential. Gaussian 16 was utilized to generate the electron density and electrostatic potential (ESP) at various points around the structure of isolated *n*-C<sub>4</sub>F<sub>10</sub> molecule at the APFD\6-31G\* level model chemistry and the corresponding optimized structure was directed to Antechamber to produce charges. The APFD\6-31G\* method was chosen because it provides more reliable and superior performance for a range of compounds than B3LYP [51] [52].

#### **4.2.3. Bond, angle, and dihedral optimization**

The Paramfit program [53] was utilized to derive force field parameters for bonded interaction terms by employing the least squares method to minimize discrepancies between the molecular mechanics (MM) calculation using the present force field and QM

energies [54]. The sets of conformations formed by the  $n$ -C<sub>4</sub>F<sub>10</sub> structure in Figure 10a have thirteen bonds: three C-C bonds, ten C-F bonds, and three atom types assigned. The C-C bonds exhibit symmetry, while C-F bonds fall into two different groups, one corresponding to two fluorines bonded to the central carbon (CF<sub>2</sub>) and the other corresponding to three fluorines bonded to the triple carbons (CF<sub>3</sub>) [55].

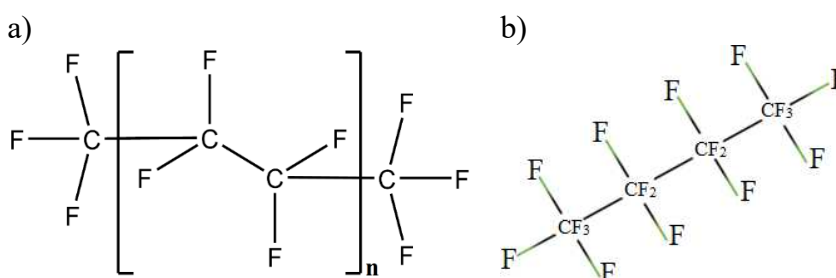


**Figure 10.** a) The molecular structure schematic of PTFE consists of long chains with repeating units of tetrafluoroethylene ( $n$  units), as indicated in parentheses. b) A bond schematic of the reference molecule to be parameterized.

The thirty-two sets of trans and gauche conformations of the  $n$ -C<sub>4</sub>F<sub>10</sub> structure were generated by sampling dihedral angles at 15° intervals. We performed relaxed sampling at each specified dihedral angle to obtain more precise potential energy profiles, permitting all other internal coordinates to relax. These angles, defined for the carbon atoms in the reference molecule, ranged from 0° to 180°. Next, calculations for single-point energy and energy gradients were conducted for these conformations using APFD\6-31G\* level theory. The conformations that result in duplicate QM energies were identified. Only one representative conformation was retained for further analysis; the others were excluded. This reduced the set of thirty-two to twenty-nine trans and gauche conformations. Twenty-

nine conformations combined 377 data points for bonds, 696 for angles, and 783 for dihedrals. The data points were employed to fit the AMBER energies to the quantum energies. The following minimization equation Eq. (A.17) was used:

$$\sum_{i=1}^N w_i \left[ \left( E_{MM}(i) - E_{QM}(i) \right)^2 + K \right] = 0 \quad (\text{A.17})$$

where  $K$  represents the internal inconsistency between quantum and AMBER energies for the system, and  $N$  stands for the number of data points corresponding to bonds, angles, and dihedrals, respectively.  $w_i$  is a weight set to 1 by default. The goal is to iteratively solve Eq. (A.17) while minimizing each value of  $K$  (i.e.,  $K_{\text{bonds}}$ ,  $K_{\text{angles}}$ , and  $K_{\text{dihedrals}}$ ). During each iteration of the minimization process, Paramfit optimized the objective functions with the combination of  $K_{\text{bonds}}$ ,  $K_{\text{angles}}$ , and  $K_{\text{dihedrals}}$  to determine  $K$  values for bonds, angles, and dihedrals, respectively, aiming to minimize potential energy errors across conformational sets compared to quantum reference data. Then, the determined  $K_{\text{bonds}}$ ,  $K_{\text{angles}}$ , and  $K_{\text{dihedrals}}$  values were used for the entire data sets for bonds, angles, and dihedrals to fit the force field parameters. These minimization steps quantified the fit quality of MM equilibrium bonds, angles, and dihedral values, enabling the force field to provide reliable predictions for all 29 conformational sets. The conformational energies computed from the MM force field were compared to QM reference values to measure the accuracy of the final bonded interaction parameter values. Additionally, all bond lengths, angles, and dihedral angles obtained from the MM force field were compared to their QM counterpart values. The

average absolute deviation (AAD) was computed for all quantities or traits, compared in Eq. (A.18):

$$AAD = \frac{\sum_{t=1}^N |QM_t - \overline{MM_t}|}{N} \quad (\text{A.18})$$

The root-mean-square deviation (RMSD) was also calculated in Eq. (A.19).

$$RMSD = \sqrt{\frac{\sum_{t=1}^N (QM_t - \overline{MM_t})^2}{N}} \quad (\text{A.19})$$

Four pairs of AAD and RMSD values were computed, one pair each from the conformational energies, bond lengths, bond angles, and dihedral angles. In the two preceding equations,  $QM_t$  is a quantum mechanics reference value for the given trait  $t$ ,  $MM_t$  is the corresponding molecular mechanics calculated value, and  $N$  denotes the total number of data points for each trait ( $N = 29$  for conformation energies, 377 for bond lengths, 696 for bond angles, and 783 for dihedral angles).

#### 4.2.4. Van der Waals optimization

We employed a combination of MD simulations using the GROMACS simulation package [42] and a simplex fitting procedure to optimize the vdW parameters for the PTFE reference molecule in condensed phases. The optimization process utilized experimental data on liquid density as 1.6 g/cm<sup>3</sup> [15] [56] and heat of vaporization as 5.46 kcal/mol [15] [56]; the former property is highly sensitive to vdW length parameters, and the latter to the

energy parameters. In all fluid simulations, cubic boxes with periodic boundary conditions were used, and each cell contained 50 reference molecules of  $n$ -C<sub>4</sub>F<sub>10</sub>. The dimensions of the cubic box were set to have cell sides measuring 25 Å, and then the cell and coordinates were compressed to give experimental density. Once the initial configurations of the fifty reference molecules of  $n$ -C<sub>4</sub>F<sub>10</sub> to be simulated were established, the optimization of the vdW was performed using the following procedure.

The fitting process involves creating a simplex with  $N$  vertices in an  $n$ -dimensional parameter space. Each vertex is represented by a vector  $\mathbf{x}_i = (x_{i1}, x_{i2}, \dots, x_{in})$ , where  $i$  ranges from 1 to  $N$ . The six Lennard-Jones force field parameters ( $\epsilon_F, \sigma_F, \epsilon_{CF_2}, \sigma_{CF_2}, \epsilon_{CF_3}, \sigma_{CF_3}$ ) for three atom types (F, CF<sub>2</sub>, and CF<sub>3</sub>) means that, here,  $n = 6$ . In that 6-dimensional parameter space, an initial simplex with seven vertices (see Table 1) was formed using the Nelder-Mead algorithm [25]. Each parameter was bounded as (0, 5) for all vertices defined. These bounds also define the range within which the parameters can be adjusted during optimization.

**Table 9.** The initial simplex has seven vertices in the parameter space.

Vertex 1:	$(\epsilon_F, \sigma_F, \epsilon_{CF_2}, \sigma_{CF_2}, \epsilon_{CF_3}, \sigma_{CF_3})$
Vertex 2:	$(\epsilon_F + \delta, \sigma_F, \epsilon_{CF_2}, \sigma_{CF_2}, \epsilon_{CF_3}, \sigma_{CF_3})$
Vertex 3:	$(\epsilon_F, \sigma_F + \delta, \epsilon_{CF_2}, \sigma_{CF_2}, \epsilon_{CF_3}, \sigma_{CF_3})$
Vertex 4:	$(\epsilon_F, \sigma_F, \epsilon_{CF_2} + \delta, \sigma_{CF_2}, \epsilon_{CF_3}, \sigma_{CF_3})$
Vertex 5:	$(\epsilon_F, \sigma_F, \epsilon_{CF_2}, \sigma_{CF_2} + \delta, \epsilon_{CF_3}, \sigma_{CF_3})$
Vertex 6:	$(\epsilon_F, \sigma_F, \epsilon_{CF_2}, \sigma_{CF_2}, \epsilon_{CF_3} + \delta, \sigma_{CF_3})$
Vertex 7:	$(\epsilon_F, \sigma_F, \epsilon_{CF_2}, \sigma_{CF_2}, \epsilon_{CF_3}, \sigma_{CF_3} + \delta)$

In Table 9,  $\delta$  is a small perturbation from the initial values and is set to 0.1 in this study. The optimization process has the following steps: 1: The system energy was minimized by employing the vertex 1 parameter set for 10000 steps using the steepest descent algorithm, followed by 1 ns NVT (constant number of particles N, volume V, and temperature T = 273 K) simulation to further equilibrate the system. 2: The equilibrated system was subsequently run in a sequence of short (20 ps) NVT simulations to test whether thermodynamic properties converged. 3: This was followed by a final data production NVT simulation for 100 ps, during which heat of vaporization was computed every 20 ps to allow for time averaging. These three steps were performed for each vertex. 4: The objective function shown in equation 5 from ref [57] was used to quantify the discrepancy between computed and target values of the heat of vaporization for each vertex in Eq. (A.20).

$$f_{target}(\{Vertex_n\}) = \left( w \left( 1 - \frac{\Delta H_{vap}(\{Vertex_n\})}{\Delta H_{vap,target}} \right)^2 \right)^{1/2} \quad (A.20)$$

where the  $w$  is the weight factor (set equal to 1 throughout this process). The  $\Delta H_{vap,target}$  is the experimental value of heat of vaporization. The  $\Delta H_{vap}(\{Vertex_n\})$  is the heat of vaporization value obtained from the parameters at that  $Vertex_n$ .

The heat of vaporization was calculated from in Eq. (A.21)

$$\Delta H_v = E_i + RT \quad (A.21)$$

where  $E_i$  represents the total internal energy of the system for the  $i$ th vertex,  $R$  is the gas constant, and  $T$  is the temperature.

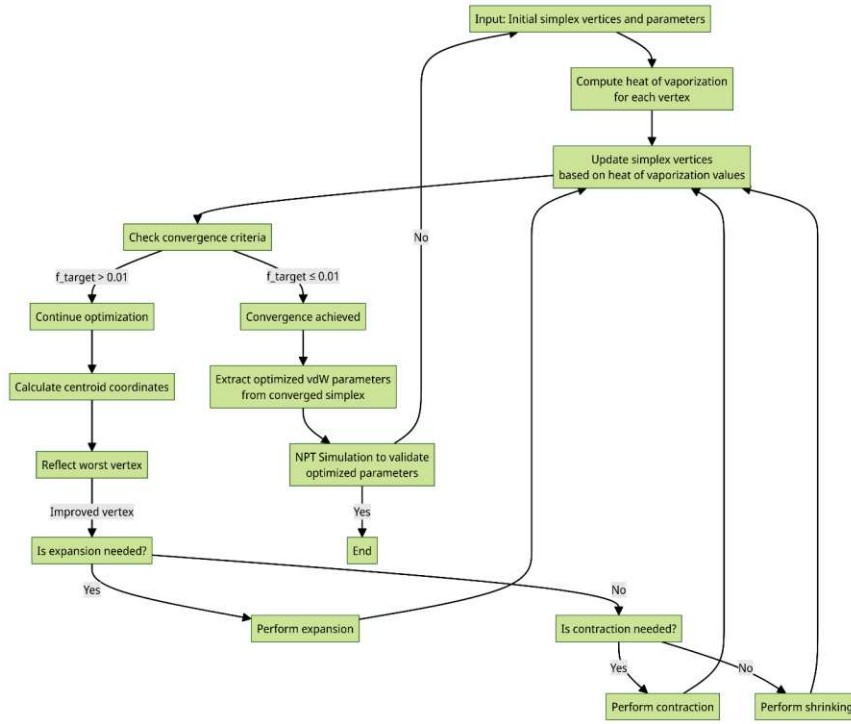


**Figure 11.** A schematic representation of the update mechanisms within the simplex optimization algorithm.

The process of simplex optimization is depicted schematically in Figure 11. The vertices except the vertex with the highest objective function value (the worst vertex) were modified based on their objective function values and using the reflection, expansion, contraction, and shrinking operations [25] [57] [58] described below; all six parameters in the vertices were adjusted simultaneously. The next step is a production stage to define new parameters for the vertices. These update operations continue the movement of the vertices in the parameter space until the convergence criteria ( $f_{target}(\{Vertex_n\}) \leq 0.01$ ) is achieved. The simplex update procedures carried out in these operations can be shown in Table 10.



It is important to note that the system box, previously equilibrated with the old parameters at each production stage, is no longer equilibrated with the new parameters. Thus, the system box must be re-equilibrated using the newly obtained vertex parameter sets to achieve a stable configuration.

**Table 10.** The simplex update operations and their equations in the parameter space.

Operations:	Equations
Centroid ( $c_j$ ):	$c_j = (x_{1j} + x_{2j} + \dots + x_{\{N-1\}j}) / (N - 1)$
Reflection ( $r_j$ ):	$r_j = c_j + (c_j - x_{wj})$
Expansion ( $e_j$ ):	$e_j = \gamma * r_j + (1 - \gamma) * c_j$
Contraction ( $co_j$ ):	$co_j = \beta * x_{wj} + (1 - \beta) * c_j$
Shrinking ( $s_{ij}$ ):	$s_{ij} = \delta * x_{bj} + (1 - \delta) * x_{ij}$

The simplex update procedure is iterative;  $j$  in Table 10 refers to the iteration number. First, the centroid coordinates are calculated by averaging the coordinates of all vertices except the worst vertex coordinates denoted as  $x_w = (x_{w1}, x_{w2}, \dots, x_{w6})$ . Here, we consider a simplex with  $N$  vertices in a 6-dimensional parameter space; each vertex is represented by a vector  $x_i = (x_{i1}, x_{i2}, \dots, x_{i6})$ , where  $i$  ranges from 1 up to  $N$ , where  $N$  denotes the total number of vertices in the simplex. In the centroid coordinate equation illustrated in Table A.2, the sum of the coordinate values for all vertices except the worst vertex (the highest objective function value) is divided by  $(N - 1)$ . Applying the equation to each coordinate  $j$ , we can compute the centroid coordinates as  $(c = (c_1, c_2, \dots, c_n))$  for the simplex. Then, each operation continues with the reflection of the vertex with the highest objective value. For each coordinate  $j$ , the reflected coordinate  $r_j$  can be computed using the equation in Table 10. Applying the equation to each coordinate  $j$ , we can compute the reflected point

coordinates  $r = (r_1, r_2, \dots, r_n)$  for the worst vertex. An expansion operation is performed if the reflected vertex has a lower objective function value (i.e., better). For each coordinate  $j$ , the expanded coordinate  $e_j$  can be computed using the equation in Table 10. In this equation,  $\gamma$  represents the expansion coefficient, dictating the magnitude of the expansion. Typically,  $\gamma$  is chosen to be greater than 1 (the value is set to  $\gamma=2$  in this research) to move the expanded point further away from the centroid. Applying this equation to each coordinate  $j$ , we can compute the expanded point coordinates  $e = (e_1, e_2, \dots, e_n)$  based on the reflected point and centroid. If the expanded point (or vertex) does not improve significantly or has a higher objective function value than the second-worst vertex, the contraction operation was performed according to the equation in Table 10. In this equation,  $\beta$  is the contraction coefficient, which determines the extent of the contraction. Typically,  $\beta$  is chosen to be less than 1 ( $\beta = (\pm)0.5$  in this research) to move the contracted point closer to the centroid. Applying this equation to each coordinate  $j$ , we can compute the contracted point coordinates  $c_o = (c_{o1}, c_{o2}, \dots, c_{on})$  based on the worst vertex and centroid. The shrinking operation is performed if none of the above operations result in a better vertex. To do this, we shrink all vertices of the simplex towards the best vertex (the vertex with the lowest objective function value). We consider the best vertex coordinates as  $x_b = (x_{b1}, x_{b2}, \dots, x_{b6})$  and the coordinates of each vertex in the simplex as  $x_i = (x_{i1}, x_{i2}, \dots, x_{i6})$ . For each vertex  $i$  and coordinate  $j$ , the shrunk coordinate  $s_{ij}$  can be computed using the equation in Table 10. In this equation,  $\delta$  is the shrinking coefficient, which determines the extent of the shrinking; note that  $\delta$  used in shrinking is distinct from  $\delta$  in Table 9. Typically,  $\delta$  is chosen to be less than 1 (we set it to  $\delta = 0.015$ ) to move the vertices closer

to the best vertex. Applying this equation to every vertex  $i$  and coordinate  $j$ , we can determine the shrunk coordinates  $s_{ij}$  for all the simplex vertices.

This optimization process involves iteratively updating the vertices of the simplex based on the objective function evaluations until the convergence criteria ( $f_{target}(\{Vertex_n\}) \leq 0.01$ ) was achieved. Then, the final simplex vertex is determined by the coordinates of each parameter ( $\epsilon$  and  $\sigma$ ) for each atom type (F, CF<sub>2</sub>, CF<sub>3</sub>). The optimized force field parameters were extracted from the converged simplex. These parameters represent optimal values aimed at minimizing the discrepancy between the calculated and reference values of the heat of vaporization. Following acquiring vdW parameters, an NPT simulation lasting 200 ps, reached equilibrium after 50 ps at a temperature of 273 K and a pressure of 1 bar. This simulation aimed to assess the density and heat of vaporization to validate the optimized parameters.

### 4.3. Parameterization results

#### 4.3.1. Charge parameters

We successfully determined the RESP charge parameters for the *n*-C<sub>4</sub>F<sub>10</sub> reference molecule for the F, CF<sub>3</sub>, and CF<sub>2</sub> atom types. The RESP charge fitting process involved two main steps: QM calculations and charge optimization. We used APFD/6-31G\* QM calculations to generate the ESP. Then, we used the Antechamber program to reproduce the same potential at the MM level by fitting the MM ESP to the QM ESP to minimize the deviation between the computed and target ESP values. Antechamber subsequently generated a file containing the RESP charges for each atom in the *n*-C<sub>4</sub>F<sub>10</sub> reference molecule, shown in Table 11. The RESP charge parameters indicate that F in the *n*-C<sub>4</sub>F<sub>10</sub>

molecule is negatively charged with  $q = -0.11018$ . This result is consistent with the electronegativity of F [59]. On the other hand,  $\text{CF}_3$  groups are positively charged with  $q = 0.33040$ , while  $\text{CF}_2$  groups are also positively charged with  $q = 0.22050$ .

**Table 11.** Optimized charge parameters for PTFE.

Charge	Types	$q(e^-)$
F	F	-0.11018
C	$\text{CF}_3$	0.33040
C	$\text{CF}_2$	0.22050

#### 4.3.2. Bond, angle, and dihedral parameters

Paramfit software minimizes the objective function, deriving MM bond, angle, and dihedral parameters relative to QM reference data. The optimization iterations were performed until the best combination of  $K_{\text{bonds}}$ ,  $K_{\text{angles}}$ , and  $K_{\text{dihedrals}}$  were obtained (i.e., when the objective function provided the lowest potential energy error across all data compared to the previous one). The convergence criterion proposed in Paramfit was used to validate the quality of the entire data parameter set at the final target  $K$  values. Figure 12a compares the MM energies of the 29 conformational sets obtained with the QM energies. These results were then compared to their QM-derived counterpart values. The MM bond length values exhibited excellent agreement with the QM values, with all cases not exceeding 0.1 Å difference Figure 12b. Similarly, for the bond angles in Figure 12c, discrepancies between MM and QM results did not exceed  $\pi/20$  radians. Furthermore, the MM dihedrals data sets in Figure 12d showed agreement within  $\pi/10$  radians across all data and conformational sets compared to the quantum reference data.

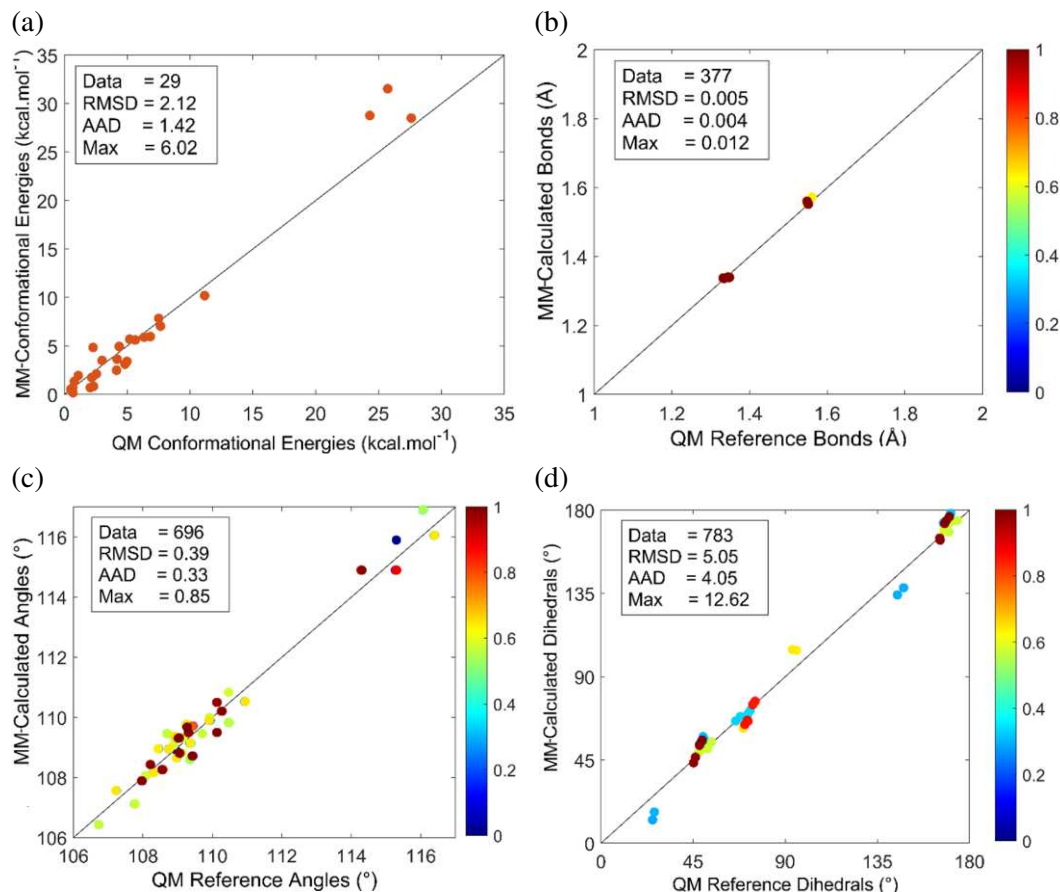


**Figure 12.** (a) The comparison between MM-calculated results and QM conformational energies across 29 conformational sets is presented. The comparison of bond lengths (b), bond angles (c), and dihedral angles (d) between MM-calculated results and QM reference values are shown, along with the total number of data points (Data), root mean square deviation (RMSD), average absolute deviation (AAD), and maximum value differences (Max).

Given the overall satisfactory agreement between MM and QM calculations across such a wide range of conformations, the final equilibrium bond length  $r_{eq}$  and bond force constant  $K_r$ , equilibrium angle  $\theta_{eq}$  and angle force constant  $K_\theta$ , dihedral barrier height  $v_n$ , dihedral phase  $\gamma$  and periodicity  $n$  shown in Tables 12, 13, and 14 were then calculated.

**Table 12.** Optimized bond parameters for PTFE.

Bond	$K_r \left( \text{kcal}(\text{mol} \cdot \text{\AA}^2) \right)^{-1}$	$r_{eq} (\text{\AA})$
CF <sub>2</sub> – CF <sub>2</sub>	251.4064	1.5898
CF <sub>2</sub> – CF <sub>3</sub>	251.4064	1.5898
CF <sub>2</sub> – F	361.8779	1.3363
CF <sub>3</sub> – F	361.8779	1.3363

**Table 13.** Optimized angle parameters for PTFE.

Angle	$K_\theta (\text{kcal}/(\text{mol} \cdot \text{radian}^2))$	$\theta_{eq} (^\circ)$
CF <sub>2</sub> – CF <sub>2</sub> – CF <sub>2</sub>	85.7729	110.9681
F – CF <sub>3</sub> – F	99.9229	109.3269
CF <sub>2</sub> – CF <sub>3</sub> – F	69.8039	108.5623
CF <sub>3</sub> – CF <sub>2</sub> – F	69.8039	108.5623
CF <sub>2</sub> – CF <sub>2</sub> – F	69.8039	108.5623
CF <sub>2</sub> – CF <sub>2</sub> – CF <sub>3</sub>	85.7729	110.9681
F – CF <sub>2</sub> – F	99.9229	109.3269

**Table 14.** Optimized dihedral parameters for PTFE.

Dihedral	Divider	$v_n (\text{kcal/mol})$	$\gamma$	$n$
CF <sub>2</sub> – CF <sub>2</sub> – CF <sub>2</sub> – CF <sub>2</sub>	1	-1.1301	0.0	-3.0
CF <sub>2</sub> – CF <sub>2</sub> – CF <sub>2</sub> – CF <sub>2</sub>	1	0.3810	0.0	-1.0
CF <sub>2</sub> – CF <sub>2</sub> – CF <sub>2</sub> – CF <sub>2</sub>	1	4.3339	180.0	2.0
CF <sub>2</sub> – CF <sub>2</sub> – CF <sub>2</sub> – CF <sub>3</sub>	1	-1.1301	0.0	-3.0
CF <sub>2</sub> – CF <sub>2</sub> – CF <sub>2</sub> – CF <sub>3</sub>	1	0.3810	0.0	-1.0
CF <sub>2</sub> – CF <sub>2</sub> – CF <sub>2</sub> – CF <sub>3</sub>	1	4.3339	180.0	2.0
CF <sub>2</sub> – CF <sub>2</sub> – CF <sub>2</sub> – F	1	-0.3651	0.0	-3.0
CF <sub>2</sub> – CF <sub>2</sub> – CF <sub>2</sub> – F	1	13.2574	0.0	-1.0
CF <sub>2</sub> – CF <sub>2</sub> – CF <sub>2</sub> – F	1	0.9940	180.0	2.0
CF <sub>2</sub> – CF <sub>2</sub> – CF <sub>3</sub> – F	1	-0.3651	0.0	-3.0
CF <sub>2</sub> – CF <sub>2</sub> – CF <sub>3</sub> – F	1	13.2574	0.0	-1.0
CF <sub>2</sub> – CF <sub>2</sub> – CF <sub>3</sub> – F	1	0.9940	180.0	2.0
CF <sub>3</sub> – CF <sub>2</sub> – CF <sub>2</sub> – F	1	-0.3651	0.0	-3.0
CF <sub>3</sub> – CF <sub>2</sub> – CF <sub>2</sub> – F	1	13.2574	0.0	-1.0
CF <sub>3</sub> – CF <sub>2</sub> – CF <sub>2</sub> – F	1	0.9940	180.0	2.0
F – CF <sub>2</sub> – CF <sub>2</sub> – F	1	0.0469	0.0	-3.0
F – CF <sub>2</sub> – CF <sub>2</sub> – F	1	18.2421	0.0	-1.0
F – CF <sub>2</sub> – CF <sub>2</sub> – F	1	1.1050	180.0	2.0
F – CF <sub>2</sub> – CF <sub>3</sub> – F	1	0.0469	0.0	-3.0
F – CF <sub>2</sub> – CF <sub>3</sub> – F	1	18.2421	0.0	-1.0
F – CF <sub>2</sub> – CF <sub>3</sub> – F	1	1.1050	180.0	2.0

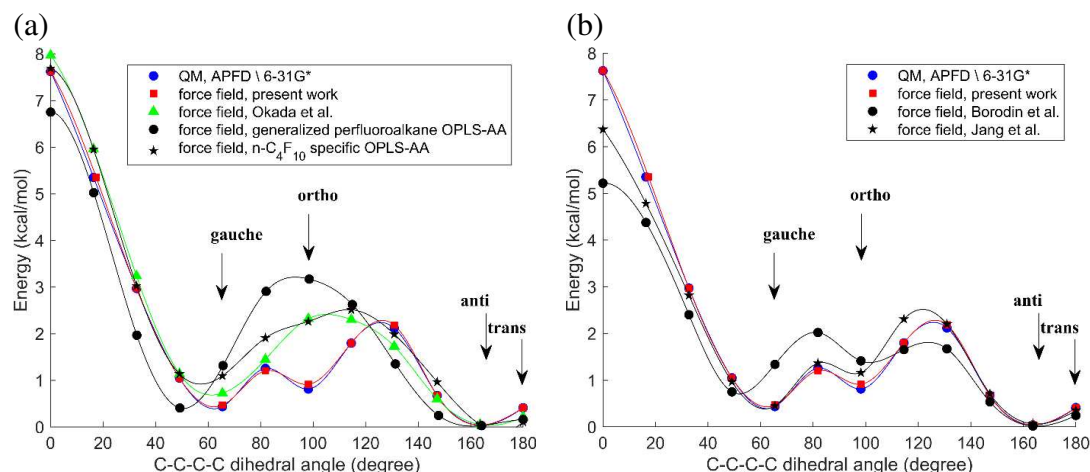


**Figure 13.** Torsional energy versus C-C-C-C dihedral angle for  $n\text{-C}_4\text{F}_{10}$  (a) from QM APFD/6-31G\* calculations (the present work) and calculations using the Okada et al., generalized perfluoroalkane OPLS-AA, and  $n\text{-C}_4\text{F}_{10}$  specific force fields. (b) from QM APFD/6-31G\* calculations (the present work) and calculations using the force fields from Borodin et al. and Jang et al.

The energy plots for the trans conformation ( $t^+$ ) from Okada et al. [7] and the  $n\text{-C}_4\text{F}_{10}$  specific and generalized perfluoroalkane OPLS-AA force field [15] agree with the QM results. However, both approaches failed to accurately reproduce the gauche conformations barrier ( $g^+$ ,  $g^-$ ). Okada et al.'s force field calculated higher energy for the gauche conformer (0.73 kcal/mol) and significantly higher energy differences, shown in Table 15, at the barriers for  $g \leftrightarrow o$  (0.79 kcal/mol) and  $o \leftrightarrow a$  (0.72 kcal/mol), indicating a less favorable description of the potential energy surface compared to other methods. Watkins and Jorgensen [15] extended HF/6-31G model chemistry to derive  $n\text{-C}_4\text{F}_{10}$  specific force field parameters by including polarization functions (indicated by the asterisk "\*"). They also used LMP2/cc-pVTZ(-f) model chemistry to derive generalized perfluoroalkane parameter sets. Their force field performance for  $n\text{-C}_4\text{F}_{10}$  was better than that of Okada et al. in terms of energy differences.

However, both parameter sets failed to reproduce conformation barriers accurately, as shown in Figure 13a.

**Table 15.** Comparison of the relative conformational energy differences (kcal/mol) of gauche (g), ortho (o), anti (a), trans (t) for C<sub>4</sub>F<sub>10</sub> as a function of the C-C-C-C torsional angle, using various force fields and their QM-derived counterpart values, including those from the present work [a], Okada et al. [7], the *n*-C<sub>4</sub>F<sub>10</sub> specific and generalized perfluoroalkane OPLS-AA force field [15], Jang et al. [10], and Borodin et al [17].

Model Chemistry (QM)							
& Force Fields (FF)	Ref.	gauche	g ↔ o	ortho	o ↔ a	anti	trans
QM→ APFD/6-31G*	[a]	0.44	1.24	0.91	2.14	0.00	0.41
FF→ Present work	[a]	0.46	1.21	0.84	2.18	0.00	0.40
QM→ HF/6-31G	[10]	0.76	2.25	2.05	2.45	0.00	0.14
FF→ Okada et al.	[10]	0.73	1.46	2.33	1.73	0.00	0.11
QM→ HF/6-31G*	[18]	0.80	2.10	1.90	2.40	0.00	0.10
FF→ OPLS-AA <sup>#</sup>	[18]	1.10	1.91	2.27	1.97	0.00	0.06
FF→ OPLS-AA	[18]	1.31	2.91	3.17	1.35	0.00	0.16
QM→ B3LYP/6-31G*	[13]	0.50	1.42	1.17	2.06	0.00	0.39
FF→ Jang et al.	[13]	0.45	1.37	1.16	2.19	0.00	0.36
QM→ MP2/aug-cc-pvDz	[20]	1.18	1.95	1.55	1.92	0.00	0.11
FF→ Borodin et al.	[20]	1.32	2.02	1.42	1.68	0.00	0.25

ref.: reference number, gauche (g): gauche energy. g ↔ o: energy difference between gauche and ortho, ortho (o): ortho energy. o ↔ a: energy difference between ortho and anti, anti (a): anti-energy, trans (t): trans energy, <sup>a</sup> present work. <sup>#</sup> *n*-C<sub>4</sub>F<sub>10</sub> specific

Jang et al.'s [10] force field sets, determined using the Dreiding-type valence potential, provided a satisfactory description of the lower energy differences and barriers, with gauche at 0.45 kcal/mol and barriers (g ↔ o: 0.05 kcal/mol), suggesting good accuracy. However, they reported that the g<sup>+</sup> and g<sup>-</sup> conformational sets were unstable at the onset of bending torsion angle values for longer polytetrafluoroethylene chains. This raises doubts about the transferability of these parameters and their reproduction of macroscopic



properties. Borodin et al.'s [17] parameter sets also described the  $g^+$ ,  $g^-$ , and  $t^+$  conformations for  $n\text{-C}_4\text{F}_{10}$ , reproducing torsional energy compared to QM calculations. However, their thermodynamic data, including density and heat of vaporization, were less precise (In the following Van der Waals parameters section) compared to the present work.

### 4.3.3. Van der waals parameters

We utilized simplex geometric transformation equations to refine six Lennard-Jones force field parameters ( $\epsilon_F$ ,  $\sigma_F$ ,  $\epsilon_{CF_2}$ ,  $\sigma_{CF_2}$ ,  $\epsilon_{CF_3}$ ,  $\sigma_{CF_3}$ ) based on the results of MD simulations. Seven vertices in the parameter space represented the six Lennard-Jones force field parameters associated with the atomic types F, CF<sub>2</sub>, and CF<sub>3</sub>. All but the worst of the seven vertices in Table 1 were updated using simplex geometric transformation equations. Among the six vertices, the vertex planes with the least objective function values are depicted in Figure 14.

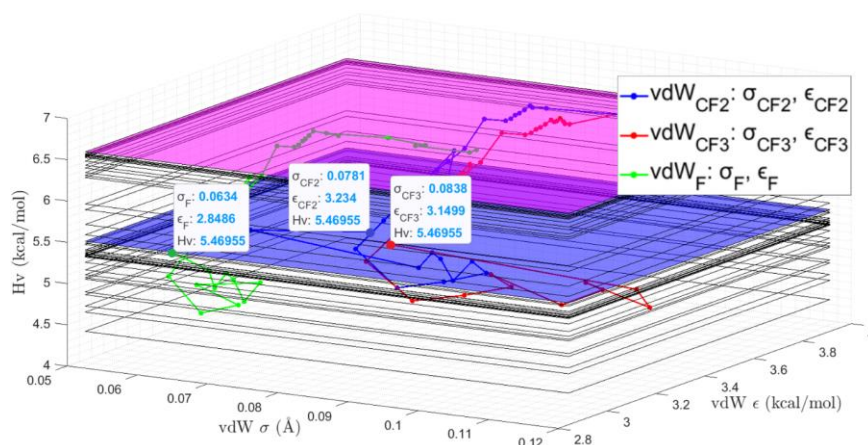


**Figure 14.** The iterative simplex update procedure starts with the first peak values in the plane highlighted in pink and ends in blue.

For each plane, six Lennard-Jones force field parameters intersected the plane, denoted by a dot. These simplex iteration steps started the creation of a total of 44 planes, each generated according to the heat of vaporization values associated with the vertices. As the procedure progressed through successive iterations, the arrangement of the vertices changed and was progressively aligned to the optimal configuration. This progressive adaptation of the simplex configuration created a dynamic framework for fine-tuning the model parameters and ultimately improved the model's predictive capacity and agreement with experimental results. The convergence criteria ( $f_{target}(\{Vertex_n\}) \leq 0.01$ ) was achieved with the force field parameters that form the final plane shown in blue, and values are presented in Table 16.

**Table 16.** Optimized vdW parameters for PTFE.

vdW	$\epsilon(\text{kcal/mol})$	$\sigma(\text{nm})$
F	2.8486	0.0634
CF <sub>3</sub>	3.1499	0.0838
CF <sub>2</sub>	3.2340	0.0781

After vdW parameters were optimized, the heat of vaporization was calculated in Eq. (A.22):

$$\Delta H_{vap}(T, P) = \langle H_{gas}(T, P) \rangle - \langle H_{liq}(T, P) \rangle + RT \quad (\text{A.22})$$

where  $\langle H_{gas}(T, P) \rangle$  represents the average total energy of the system in the vapor phase,  $\langle H_{liq}(T, P) \rangle$  represents the average total energy of the system in the liquid phase,  $R$  denotes the ideal gas constant, and  $T$  is the absolute temperature. The total energy included

contributions from bonded and nonbonded interactions and kinetic energy. NPT simulations were conducted at 200, 273, and 298 K with a pressure of 101.3 kPa to calculate the average total energy in both liquid and gas phases, with 50 molecules in the liquid phase and one in the gas phase. Our results for the heat of vaporization and density were compared with experimental data and results from other force fields in Figure 15.

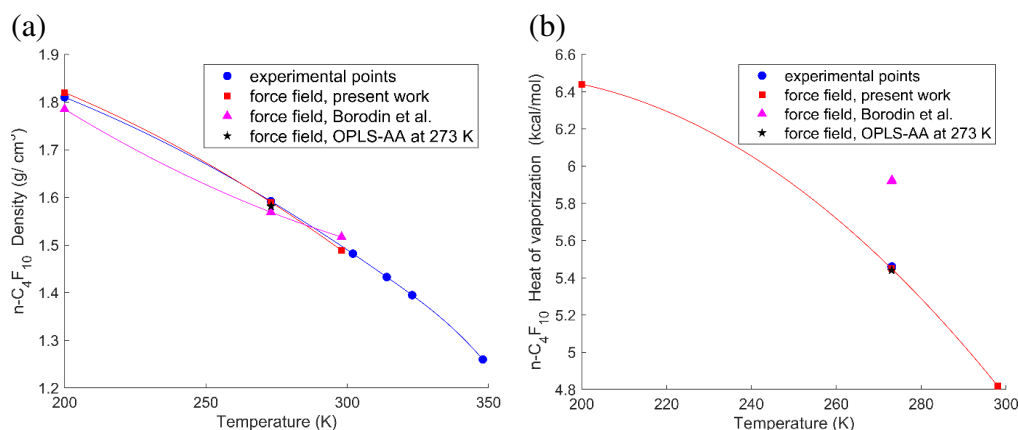


**Figure 15.** Variation of density (a) and heat of vaporization (b) with temperature for  $n\text{-C}_4\text{F}_{10}$ .

The density of  $n\text{-C}_4\text{F}_{10}$ , as presented in Figure 15a (in  $\text{g/cm}^3$ ), found at 273 K is 1.591. This performs better than the parameter sets from Jang et al. (1.650) [10], Borodin et al. (1.569) [17], and OPLS-AA (1.581) [15] but is nearly identical to the experimental value of 1.592 reported in reference [56]. At another temperature point, 200 K, the density we obtained is 1.820, compared with the experimental density of 1.810 [56]. This is better than the value from Borodin et al. (1.785) [17]. Our result for the heat of vaporization ( $\text{kcal/mol}$ ), as presented in Figure 15b, is 5.450 at a temperature of 273 K. This value is in close agreement with the experimental value of 5.460, as referenced in [56]. This level of accuracy signifies an improvement over the results obtained using the parameter sets

reported by Okada et al. (5.540) [7] and Borodin et al. (5.920) [17], indicating that our methodology provides a more precise match to the heat of vaporization data. However, even though the density is improved, the calculated heat of vaporization value at 273 K is the same as that obtained using the OPLS-AA force field. At 200 K and 298 K, we were not able to make a comparison between the values we calculated due to a lack of experimental and previous force field data.

#### **4.4. Validation methodologies and results**

Validations described in this section involved executing molecular dynamics (MD) simulations in NPT or NVT equilibrium ensembles. For all of these simulations, the time step used was 2.0 femtoseconds (fs), and short-range interactions were computed using Lennard-Jones potentials with a 10 Å cutoff, supplemented with a dispersion correction to account for contributions to energy and pressure from long-range interactions. Arithmetic (for length parameters) and geometric (for energy parameters) averaging rules were used to calculate LJ interactions. The simulation utilized the particle mesh Ewald (PME) [60] method to handle electrostatic interactions, coupled with the Nose-Hoover thermostat [44] [61] to maintain the desired temperature (unless specified otherwise, simulations below were at  $T = 300$  K). The Parrinello-Rahman approach [45] to regulate pressure at 1 bar was used in NPT ensembles.

##### **4.4.1. Density distribution**

This validation aims to transfer the derived AMBER force field parameters to PTFE models with varying molecular weights to determine the average density distribution in specific

regions of these models and compare them against experimental density data to evaluate the accuracy and reliability of the derived force field parameters. Therefore, the QuantumATK molecular simulation software [62] was first utilized with the Monte Carlo method using the OPLS Potential Builder tool [63] to create PTFE models in varying sizes:  $[\text{CF}_3-(\text{C}_2\text{F}_4)_{20}-\text{CF}_3]_{20}$  (this chemical configuration describes a polymer made up of 20 repeating units of a  $(\text{CF}_3-(\text{C}_2\text{F}_4)_{20}-\text{CF}_3)$  chain. Each chain consists of a  $\text{CF}_3$  group, followed by 20 repeating units of  $\text{C}_2\text{F}_4$  (tetrafluoroethylene), and another  $\text{CF}_3$  group at the other end),  $[\text{CF}_3-(\text{C}_2\text{F}_4)_{40}-\text{CF}_3]_{40}$ ,  $[\text{CF}_3-(\text{C}_2\text{F}_4)_{50}-\text{CF}_3]_{50}$ , and  $[\text{CF}_3-(\text{C}_2\text{F}_4)_{100}-\text{CF}_3]_{100}$ . Then, the Force-Capped Molecular Dynamics technique implemented in the QuantumATK software [62] was selected to model PTFE, aiming to mitigate concerns regarding atom overlap or artificially closed atoms within the system. Once the models with variable weights were created, the ACPYPE [64], a Python 3 tool, was employed to convert the force field from AMBER to GROMACS topology files. Then, all MD simulations were executed using GROMACS [42] to obtain the densities and radial distribution function (RDF) from well-equilibrated GROMACS trajectories. The density was first computed by dividing each system into slabs along the z-direction to probe if density variations existed within each molecular weight ensemble. Density in each slab was computed as  $\rho = m/V$ , where  $\rho$  is the density,  $m$  is the total mass of the atoms in that slab, and  $V$  is the volume of the slab. The average density in different sub-regions of each ensemble was compared, and no systematic variations were detected. For each ensemble, slab density data were averaged to determine the final density for that molecular weight. The results were compared with experimental data and previous simulations. Visualizations and results are presented in Figure 16 and Table 17, respectively.

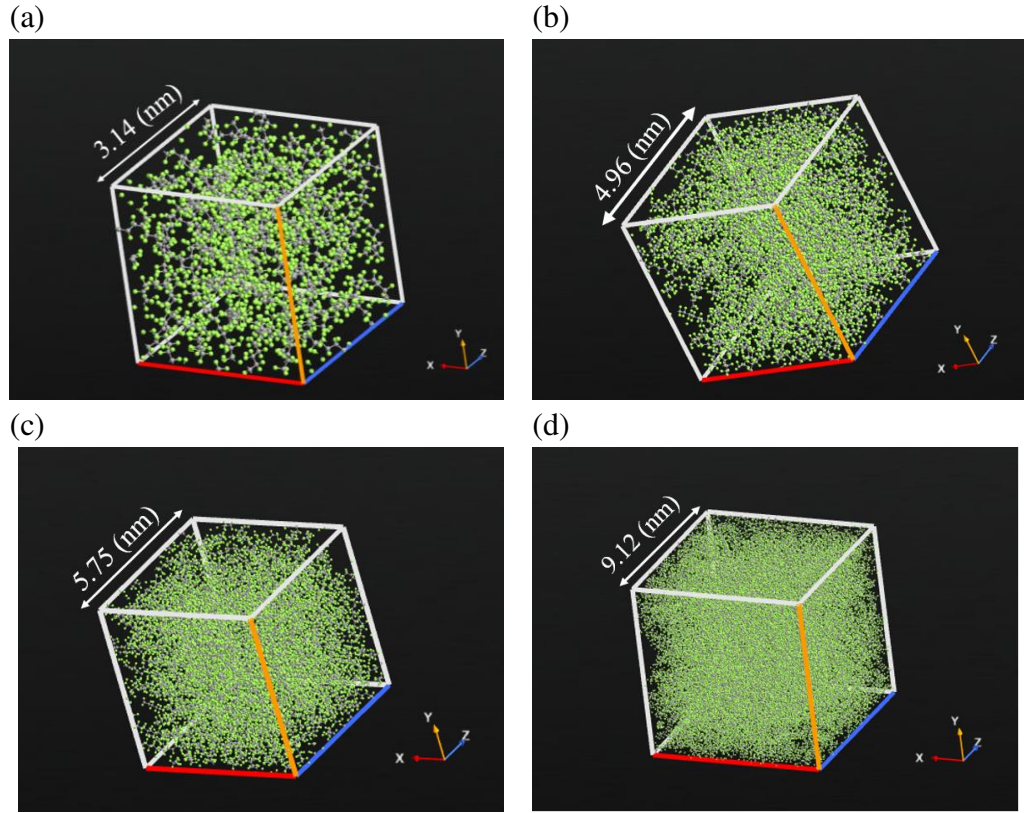


**Figure 16.** The equilibrated cubic PTFE ensembles of varying size: (a)  $[\text{CF}_3-(\text{C}_2\text{F}_4)_{20}-\text{CF}_3]_{20}$ , (b)  $[\text{CF}_3-(\text{C}_2\text{F}_4)_{40}-\text{CF}_3]_{40}$ , (c)  $[\text{CF}_3-(\text{C}_2\text{F}_4)_{50}-\text{CF}_3]_{50}$ , and (d)  $[\text{CF}_3-(\text{C}_2\text{F}_4)_{100}-\text{CF}_3]_{100}$ .

**Table 17.** Comparison of our density ( $\text{kg/m}^3$ ) and percent error (%) from MD simulations of various-sized PTFE ensembles, with MD simulations using Okada [7] and GAFF force field parameters [19], with the experimental density at 300 K reported in reference [65].

Molecular weights	$[\text{CF}_3-(\text{C}_2\text{F}_4)_{20}-\text{CF}_3]_{20}$	$[\text{CF}_3-(\text{C}_2\text{F}_4)_{40}-\text{CF}_3]_{40}$	$[\text{CF}_3-(\text{C}_2\text{F}_4)_{50}-\text{CF}_3]_{50}$	$[\text{CF}_3-(\text{C}_2\text{F}_4)_{100}-\text{CF}_3]_{100}$	Okada Force Field	GAFF Force Field	Expt.
Density	2,151	2,201	2,171	2,161	1,900	1,820	2,180
Error (%)	1.4%	0.9%	0.4%	0.8%	13%	17%	0%

Rahul et al. [20] conducted MD simulations of PTFE using GAFF parameters [19] for five chain lengths and reported a predicted density of  $1,820 \text{ kg/m}^3$ . Okada et al. [7] performed

MD simulations on amorphous PTFE assemblies and observed a predicted density of 1,900 kg/m<sup>3</sup>. The percentage of errors reported by Rahul et al. and Okada et al. was significantly higher than that of the present study.

#### 4.4.2. Radial distribution function

The pair-specific spherical atomic radial distribution functions  $g_{CF}(r)$  were calculated to determine the coordination of fluorine (F) atoms around carbon (C) atoms over a GROMACS trajectory using the VMD GUI Plugin [66]. The RDF is determined by measuring the distances between atoms or particles within specified groups. This distance data is then converted into a histogram, where the occurrences of particles at various distances are counted. To obtain the RDF, the counts in the histogram are divided by the average density. The mathematical expression in Eq. (A.23) for the RDF,  $g_{CF}(r)$ :

$$g_{CF}(r) = \frac{\rho_{CF}(r)}{\rho_C \cdot \rho_F \cdot (4\pi r^2) \cdot \Delta r} \quad (\text{A.23})$$

The  $g_{CF}(r)$ , characterizes the spatial arrangement of  $F$  atoms around  $C$  atoms in a given system. It represents the probability of encountering an  $F$  atom located at a specific distance ' $r$ ' from a  $C$  atom, normalized based on the system's average  $C$  and  $F$  atom density. The number density of  $F$  atoms around a  $C$  atom at distance ' $r$ ' is denoted by  $\rho_{CF}(r)$ , while  $\rho_C$  and  $\rho_F$  refer to the densities of  $C$  and  $F$  in the assembled system. The width of the spherical shell (bin size), denoted as  $\Delta r$ , is used to accumulate atoms within a distance range from ' $r$ ' to ' $r + \Delta r$ ', and the surface area of this shell is given by  $4\pi r^2$ . RDF

results depicted in Figure 15 show that atomic interactions and structural properties of the PTFE system remain relatively consistent and do not significantly alter with changes in ensemble size and/or molecular weight. Xu et al. [67] observed that the amorphous PTFE peaks appear around  $2\Theta = 10^\circ$ ,  $20^\circ$ ,  $33^\circ$ , and  $40^\circ$  in X-ray diffraction experiments using Cu-K $\alpha$  radiation. These peaks match those in the radial distribution function at 8.851 Å, 4.285 Å, 2.722 Å, and 2.2515 Å, respectively. These peak values were compared with the calculated ones shown in Figure 17.

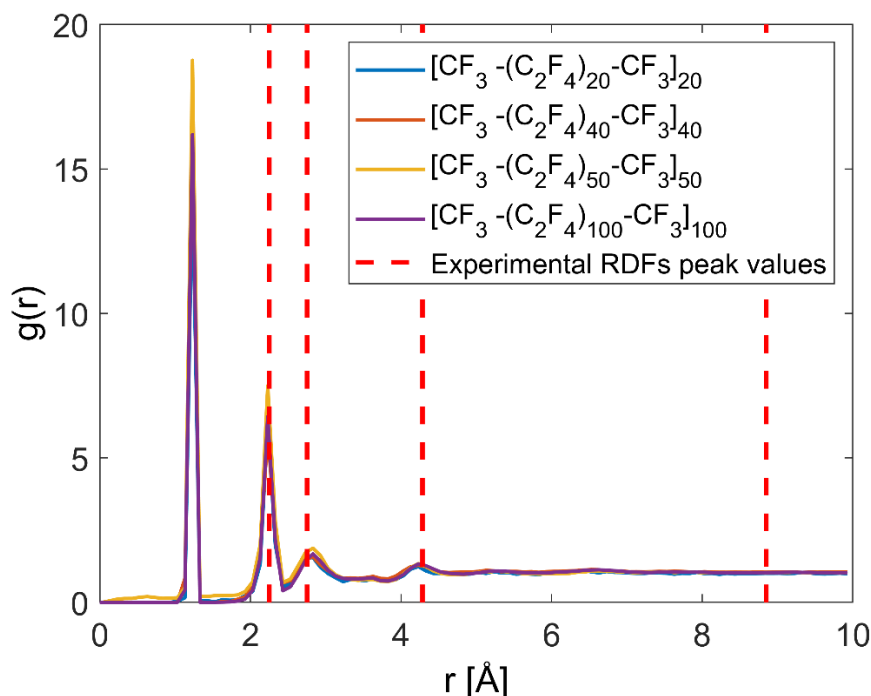


**Figure 17.** Comparison of experimental RDF peak values with RDFs for equilibrated cubic PTFE ensembles of various sizes:  $[\text{CF}_3-(\text{C}_2\text{F}_4)_{20}-\text{CF}_3]_{20}$ ,  $[\text{CF}_3-(\text{C}_2\text{F}_4)_{40}-\text{CF}_3]_{40}$ ,  $[\text{CF}_3-(\text{C}_2\text{F}_4)_{50}-\text{CF}_3]_{50}$ , and  $[\text{CF}_3-(\text{C}_2\text{F}_4)_{100}-\text{CF}_3]_{100}$ .

In Figure 17, the initial peak calculated at around  $\sim 1$  Å does not match any experimental peak. Several factors can explain this discrepancy. Experimental methods like X-ray



diffraction or neutron scattering, used to obtain the RDF, may not have the resolution or sensitivity to detect short-range interactions. These techniques are usually optimized for capturing broader, more averaged interactions within the material, possibly overlooking fine details at such short distances [68] [69].

#### 4.4.3. Power spectrum

The power spectrum or velocity density of states (VDOS) is calculated using data from an MD simulation according to [41] as following Eq. (A.24):

$$P(\omega) = \int_{-\infty}^{+\infty} C(t) e^{i\omega t} dt \quad (\text{A.24})$$

where  $C(t)$  is the normalized velocity autocorrelation function (VACF). The calculation of the  $C(t)$  is explained below in Eq. (A.25):

$$C(t) = \sum_{i=1}^m v_k(i) v_k(i+n) / \sum_{i=1}^m v_k(i) v_k(i) \quad (\text{A.25})$$

The  $v_k(i) v_k(i+n)$  term represents the correlation between the velocity at the time  $i \cdot \Delta t$  and the velocity at the time  $(i+n) \cdot \Delta t$ . The  $v_k(i) v_k(i)$  is the correlation of the velocity with itself, and  $m$  is the total number of time steps over which the correlation will be computed. The  $v_k$  is the velocity associated with a specific wave vector in Fourier space defined in Eq. (A.26):

$$v_k(t) = \sum_j u_j(t) e^{ikx_j^0} \quad (\text{A.26})$$

The  $u_j(t)$  is the velocity vector of the  $j$ -th atom at time  $t$ . The  $e^{ikx_j^0}$  is the complex exponential function, where  $k = \frac{2\pi}{\lambda}$  is the wave vector,  $x_j^0$  is defined as the initial position or reference position of the  $j$ -th atom. The wave vector ( $k$ ) specifies the wave's spatial frequency and is inversely related to the wavelength ( $\lambda$ ) of the wave. By summing over all particles and multiplying each particle's displacement  $u_j(t)$  by the complex exponential factor  $e^{ikx_j^0}$ , one can obtain the combined effect of each particle's contribution to the velocity associated with wave vector  $k$  at time  $t$  [40]. To compute the power spectrum from the VACF, MD simulations were performed using periodic boundary conditions in a cubic box with an edge length of 200 Å using GROMACS software [42]. The simulations included a chain composed of 50  $n$ -C<sub>4</sub>F<sub>10</sub> reference molecules. The system's energy was first minimized over 10000 steps using the steepest descent algorithm. Then, an NPT simulation ran for 1.2 ns (nanoseconds) to adjust box length/density. Next, NVT simulations at  $T = 300$  K were conducted using a box size from the previous NPT step to further equilibrate the system. After NVT equilibration, power spectra were calculated over 200 ps of analysis time. The temporal variation of the VACF results can be observed in Figure. 18a. In Figure 18b, we compared the VDOS results with the experimental infrared spectrum. The peak positions of the calculated VDOS closely correspond to those observed in the experimental infrared spectrum obtained from a reference source [70].

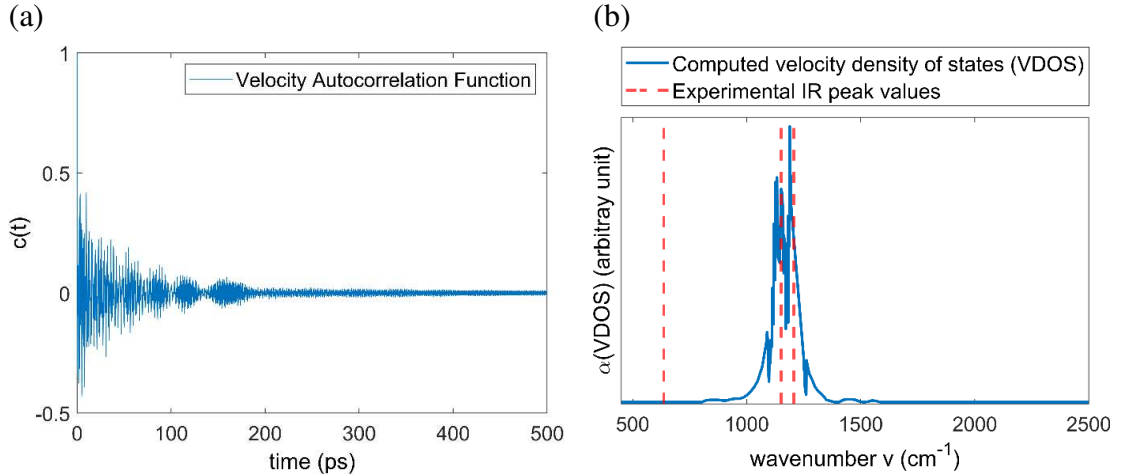


**Figure 18.** (a) Temporal variation of the velocity autocorrelation function. (b) VDOS or power spectrum of the PTFE chain (500 to 2500  $\text{cm}^{-1}$ ) with experimental peak points shown by the red dashed lines.

The temporal variation of the VACF (Figure 16a) illustrates the evolving correlation between velocities over time. Experimental peak values, indicated by red dashed lines in Figure 18b, were compared with values obtained from MD simulations. Four prominent peaks were observed at wavenumbers 1207, 1151, 638, and 626  $\text{cm}^{-1}$  in the experimental infrared spectrum of PTFE fibers [70]. The peak at 638  $\text{cm}^{-1}$  in the experimental spectrum was attributed to a regular helix structure. In contrast, the peak at 626  $\text{cm}^{-1}$  was linked to a helix-reversal defect in PTFE fibers, which was not observed in the MD simulation results [71]. The bands at 1207 and 1151  $\text{cm}^{-1}$  were previously considered insensitive to the crystallinity level [72]. These bands have been attributed to the symmetric and asymmetric stretching vibrations of  $\text{CF}_2$  and C-C groups within the PTFE fibers. The computed peak positions of 1189 and 1132  $\text{cm}^{-1}$  closely matched the experimental study's peak positions of 1207 and 1151  $\text{cm}^{-1}$ , with deviations of 18 and 19  $\text{cm}^{-1}$ , respectively.

#### 4.4.4. Specific heat capacity

The specific heat ( $C_p(T)$ ), or heat capacity per mass unit, was calculated based on the PTFE assemblies' vibrational modes at constant volume across temperatures using QuantumATK.

The expression of  $C_p(T)$  is described by the following in Eq. (A.27) formula [73]:

$$C_p(T) = \frac{h^2}{mk_B T^2} \int_0^\infty \frac{v^2 \exp(hv/k_B T)}{(\exp(hv/k_B T) - 1)^2} g(v) dv \quad (\text{A.27})$$

where  $T$  represents the temperature,  $v$  denotes the vibrational frequency,  $h$  stands for Planck's constant,  $m$  indicates the total mass of the atoms in the unit cell,  $k_B$  represents Boltzmann's constant, and  $g(v)$  symbolizes the vibrational density of states, which describes how energy is distributed among vibrational modes [74]. The integral in the formula calculates the contribution of each vibrational mode to the specific heat, weighted by the  $g(v)$ . The fraction within the integral represents the population of each vibrational mode at temperature  $T$ , as described by the Bose-Einstein distribution. The factor,  $h^2/(2\pi mk_B T)^2$ , positioned outside the integral, normalizes the units and scales the result appropriately. For this analysis, after NPT equilibration described in the preceding section, MD simulations were executed under the NVT ensemble, wherein the temperature ranged from 0 to 800 K in increments of 100 K over a total duration of 3 ns, followed by a 1 ns duration at 800 K. After that, the temperature decreased to 300 K with the cooling rate of 4 K/ps and held for another 1 ns. Specific heat capacity was calculated during this entire MD trajectory using QuantumATK [62]. Our calculations yielded a heat capacity of 1.15 ( $\text{J}\cdot\text{g}^{-1}\cdot\text{K}^{-1}$ ) with a percent error of 4.5% based on molecular dynamics (MD) simulations

performed on four distinct assemblies of PTFE. This result closely aligns with the experimental finding of  $1.10 \text{ (J.g}^{-1}.\text{K}^{-1})$  reported by G. T. Furukawa et al. [75] (see Figure 19). Additionally, Rahul et al. [20] conducted MD simulations using standard GAFF parameters [19] to predict the specific heat across various sizes of PTFE ensembles at only 300 K. Therefore, only 300 K comparisons were made. Their computational estimate was  $1.37 \text{ (J.g}^{-1}.\text{K}^{-1})$ , with a reported percent error of 24.5%, significantly higher than our calculated value.

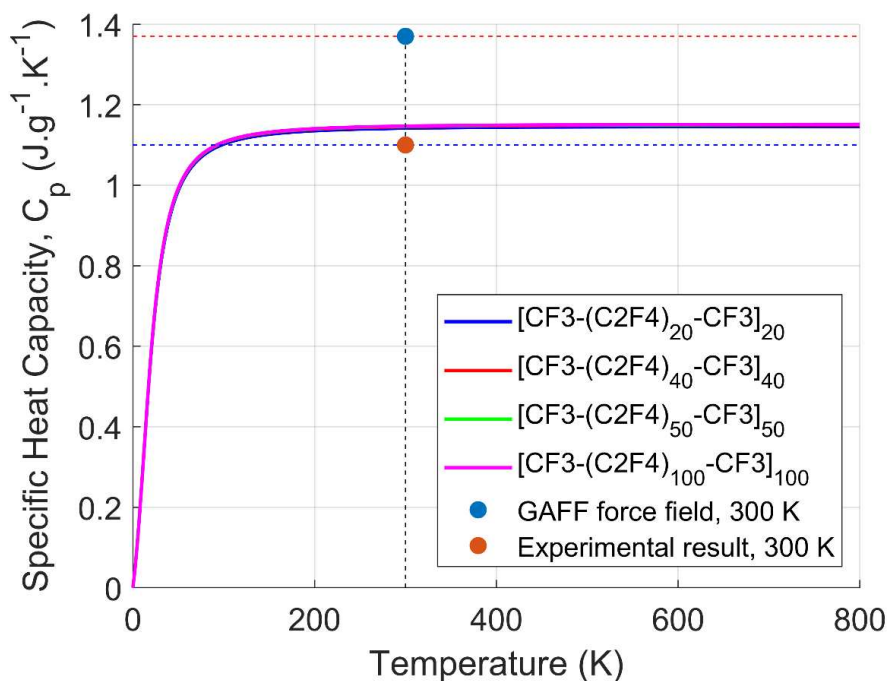


**Figure 19.** Comparison of computed and experimental specific heat capacity vs. temperature for different ensembles of various sizes:  $[\text{CF}_3-(\text{C}_2\text{F}_4)_{20}-\text{CF}_3]_{20}$ ,  $[\text{CF}_3-(\text{C}_2\text{F}_4)_{40}-\text{CF}_3]_{40}$ ,  $[\text{CF}_3-(\text{C}_2\text{F}_4)_{50}-\text{CF}_3]_{50}$ , and  $[\text{CF}_3-(\text{C}_2\text{F}_4)_{100}-\text{CF}_3]_{100}$ .

## **Chapter 5: Effects of Salinity and Temperature on Droplet Wettability on Hydrophobic Surface**

### **5.1. Introduction**

In this chapter, we examine the influence of salinity and temperature on the wettability of water nanodroplets on a realistically modeled hydrophobic PTFE surface. The primary focus is how sodium chloride (NaCl) concentrations and varying temperatures (25°C and 80°C) affect the contact angles of water droplets, as modeled through MD simulations. Most studies have been limited to smooth surfaces and hydrophilic materials. This study addresses that gap by providing a comprehensive analysis of droplet wettability, revealed by examining contact angle, ion concentration, density distribution at the interfacial area, and the radial distribution function.

### **5.2. Methods**

#### **5.2.1. Simulation setting and molecular interactions**

MD simulations were performed using the LAMMPS [76] software package to investigate the contact angle of NaCl-water nanodroplets on a PTFE surface. The open visualization (OVITO) [77] and visual molecular dynamics (VMD) [66] tools were used for post-

processing atomistic data obtained from MD trajectories. The simulations employed actual units, a full atom style, and periodic boundaries in three dimensions. As described in Eq. (A.28), interactions between atoms were modeled using the Lennard-Jones and Coulombic potentials, both specified with a cutoff of 10 Å and utilized the lj/cut/coul/long pair style. Long-range electrostatic interactions were calculated using the Particle-Particle Particle-Mesh (PPPM) method [60] with a  $10^{-5}$  precision and a fourth-order accuracy in the k-space interpolation.

$$u_{ij}(r) = 4\epsilon_{ij} \left[ \left( \frac{\sigma_{ij}}{r} \right)^{12} - \left( \frac{\sigma_{ij}}{r} \right)^6 \right] + \frac{1}{4\pi\epsilon_0} \frac{q_i q_j}{r} \quad (\text{A.28})$$

where  $r$  indicates the distance between positions  $i$  and  $j$ ,  $q_i$  and  $q_j$  refer to the electric charge at sites  $i$  and  $j$ , respectively. The  $\epsilon_0$  is the vacuum permittivity,  $\epsilon_{ij}$  represents the well depth of the LJ potential, and  $\sigma_{ij}$  is the characteristic diameter. The mixed pair coefficients were generated between atoms of type  $i$  and  $j$  using the arithmetic mixing combination rule:  $\epsilon_{ij} = \sqrt{\epsilon_i \epsilon_j}$ , and  $\sigma_{ij} = (\sigma_i + \sigma_j)/2$ . The system was composed of F (fluorine), C (carbon) in  $\text{CF}_3$  groups, C in  $\text{CF}_2$  groups for PTFE,  $\text{H}_2\text{O}$  (water),  $\text{Na}^+$  (sodium ions), and  $\text{Cl}^-$  (chloride ions). The transferable bonded, Lennard-Jones, and charge parameters for PTFE, as obtained in reference [78] [79], were used in both the assembly of PTFE and the MD simulations. The SPC/E (extended) water model [80] was used to establish a nanoscale bulk water system. The OPLS-derived [81] Lennard-Jones and charge parameters for the  $\text{Na}^+$  and  $\text{Cl}^-$  were obtained from the GROMACS software [42]. Non-bonded parameters are in Table 18.

**Table 18.** Lennard-Jones parameters and partial charges for PTFE, water, and ions.

Pair Coeffs	$\sigma(\text{nm})$	$\epsilon(\text{kJ/mol})$	$q(e)$
F <sub>(PTFE)</sub>	2.5378	0.0634	-0.11018
CF <sub>3</sub> <sub>(PTFE)</sub>	2.8062	0.0838	0.33040
CF <sub>2</sub> <sub>(PTFE)</sub>	2.8812	0.0781	0.22050
O <sub>(water)</sub>	3.1655	0.1554	-0.84760
H <sub>(water)</sub>	0.0	0.0	0.42380
Na <sup>+</sup> <sub>(ion)</sub>	3.3304	0.0027	1
Cl <sup>-</sup> <sub>(ion)</sub>	4.4172	0.1177	-1

The system dynamics were stabilized using the Nosé-Hoover thermostat set [82] at different temperatures, i.e.,  $T = 298.15$  and  $353.15$  K across all groups, with individual control for each group to simulate the thermal environment accurately. Bond and angle potentials were maintained using harmonic constraints [83], and dihedral interactions followed the OPLS style [15]. The velocity-verlet algorithm was used to integrate the atomic velocities and positions with a time step of 2.0 femtoseconds (fs).

### 5.2.2. Constructing the simulation model

The construction of the amorphous PTFE model is schematically illustrated in Figure 20. The PTFE polymer chain was initially constructed with repeating units arranged as CF<sub>3</sub>-(C<sub>2</sub>F<sub>4</sub>)<sub>n</sub>-CF<sub>3</sub>, based on the force field parameters data [79] developed by Orhan Kaya et al. [78]. In this arrangement, 'n' represents the number of tetrafluoroethylene (C<sub>2</sub>F<sub>4</sub>) units and is set at 50. Trifluoromethyl groups (CF<sub>3</sub>) cap the chain at both ends, as shown in Figure 20a. After the initial polymer chain was constructed using Avogadro [27], it was duplicated to create 50 identical chains, as illustrated in Figure 20b. These were then randomly positioned within a cubic lattice to mimic an amorphous PTFE polymer's disordered,



tangled nature. Subsequently, energy minimization was conducted to eliminate any unrealistic overlaps between atoms that might have arisen during the random arrangement of the chains. Finally, a 5 ns MD simulation with an NPT (constant number of Particles (N), Pressure (P), and Temperature (T)) thermostat was used in the equilibration phase to stabilize the system at 298.15 K and 101.325 kPa, ensuring the experimental density value of 2,180 (kg/m<sup>3</sup>) [65] was achieved using LAMMPS, as displayed in Figure 20c. After achieving the desired experimental density with the cubic PTFE assembly, the simulation lattice was replicated, as shown in Figure 20d, six times along the x-axis, six times along the y-axis, and twice along the z-axis in LAMMPS to increase the size of the system. Then, the replicated amorphous PTFE model was equilibrated for 1 ns using an NVT thermostat (constant number of particles (N), volume (V), and temperature (T)) at two different temperatures, 298.15 K and 353.15 K, to establish the equilibrated conditions for merging with pure and saline water lattices.

For constructing the pure and saline water models, initial cubic lattices with edge lengths of 16, 20, and 24 nm were built to contain SPC/E water molecules. We established a minimum edge length of 16 nm based on findings by Giovambattista et al. [84], who determined that line tension has only a minor effect on edge lengths larger than 3.25 nm. Packmol [85] positioned water molecules in each lattice with a 2.0 Å spacing and a 1.5 Å safety margin to avoid boundary artifacts.

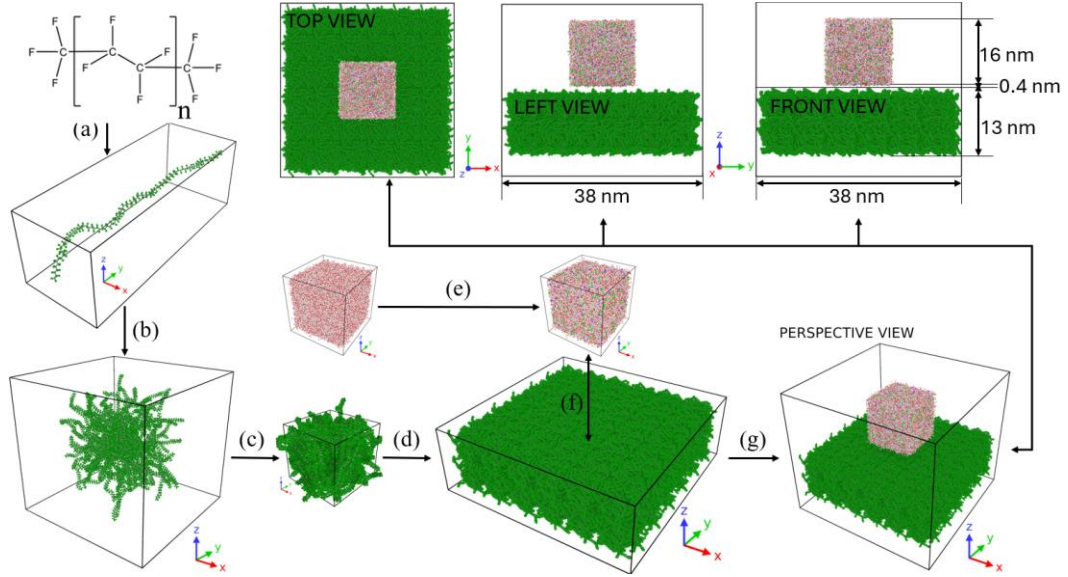


**Figure 20.** Simulation model construction workflow: (a) Initial PTFE chain with  $n = 50$  tetrafluoroethylene units. (b) Replication into 50 chains in a cubic lattice. (c) Energy minimization and 5 ns MD simulation at 298.15 K and 101.325 kPa. (d) Lattice replication to enlarge amorphous PTFE for analysis. (e) Integration of  $\text{Na}^+$  and  $\text{Cl}^-$  ions into an SPC/E water lattice. (f) Final merging of equilibrated saline and pure water lattices with PTFE at 298.15 K and 353.15 K. (g) Visualization of lattice configurations in 3D isometric and 2D orthographic projections.

It was then used to delete water molecules and insert  $\text{Na}^+$  and  $\text{Cl}^-$  ions, as illustrated in Figure 20e, to achieve the target NaCl mass concentration ( $C_{\text{NaCl}}$ ) using Eq. (A.29).

$$C_{\text{NaCl}} = \frac{m_{\text{Na}^+} + m_{\text{Cl}^-}}{m_{\text{water}} + m_{\text{Na}^+} + m_{\text{Cl}^-}} \times 100\% \quad (\text{A.29})$$

where  $C_{\text{NaCl}}$  represents the mass concentration of the solution in percentage.  $m_{\text{Na}^+}$  and  $m_{\text{Cl}^-}$  are the masses of sodium and chloride ions, respectively, and  $m_{\text{water}}$  is the mass of the water in the solution. Table 19 details the quantities of water molecules, the added  $\text{Na}^+$  and  $\text{Cl}^-$  ions, and  $C_{\text{NaCl}}$  for each of the three cubic lattices.

**Table 19.** The configuration of six different cubic saline cases.

Lattice edge-length (nm)	N <sub>water</sub>	N <sub>Na<sup>+</sup></sub>	N <sub>Cl<sup>-</sup></sub>	C <sub>NaCl</sub>
16 (equal 20nm sphere)	130600	3700	3700	8.45%
20 (equal 25nm sphere)	253546	7227	7227	8.45%
24 (equal 30nm sphere)	440024	12488	12488	8.45%

A total of 6 cubic configurations of pure and saline water were generated, including three saline cases, as detailed in Table 19, and three pure cases. These configurations underwent a 1 ns NVT equilibration simulation at two different temperatures, 298.15 K and 353.15 K, to establish equilibrium and ensure the absence of non-physical interactions in the simulation results before merging with an amorphous PTFE model, as depicted in Figure 20f. A total of 12 cubic configurations, including variations in two temperatures, were accurately positioned 0.4 nm above the highest (in z) atom of PTFE and centered on the amorphous PTFE surface for both saline and pure lattices. The 12 nm lattice edge-length droplet is merged and shown in Figure 20g from perspective views and Figure 20i from the top, left, and front views. After the merged systems were constructed, the 12 cubic configurations of pure and saline water were accurately established and then prepared for the equilibration process.

### 5.2.3. Measurement of surface roughness and contact angle

The 12 cubic configurations were equilibrated—droplets with 20, 25, and 30 nm diameters were formed, as listed in Table 19. Figure 21 depicts the equilibration process from panels a to d for a 20 nm droplet. In panels f, e, and g, the time-dependent growth of the interfacial area on PTFE for 20, 25, and 30 nm droplets, respectively, was shown. At 0 nanoseconds (ns), the droplet starts in a compact, square configuration, indicating no initial interaction

with the surface. As time progresses towards 0.32 ns, the droplet spreads and flattens, transitioning towards a spherical shape due to surface tension and adhesive forces.

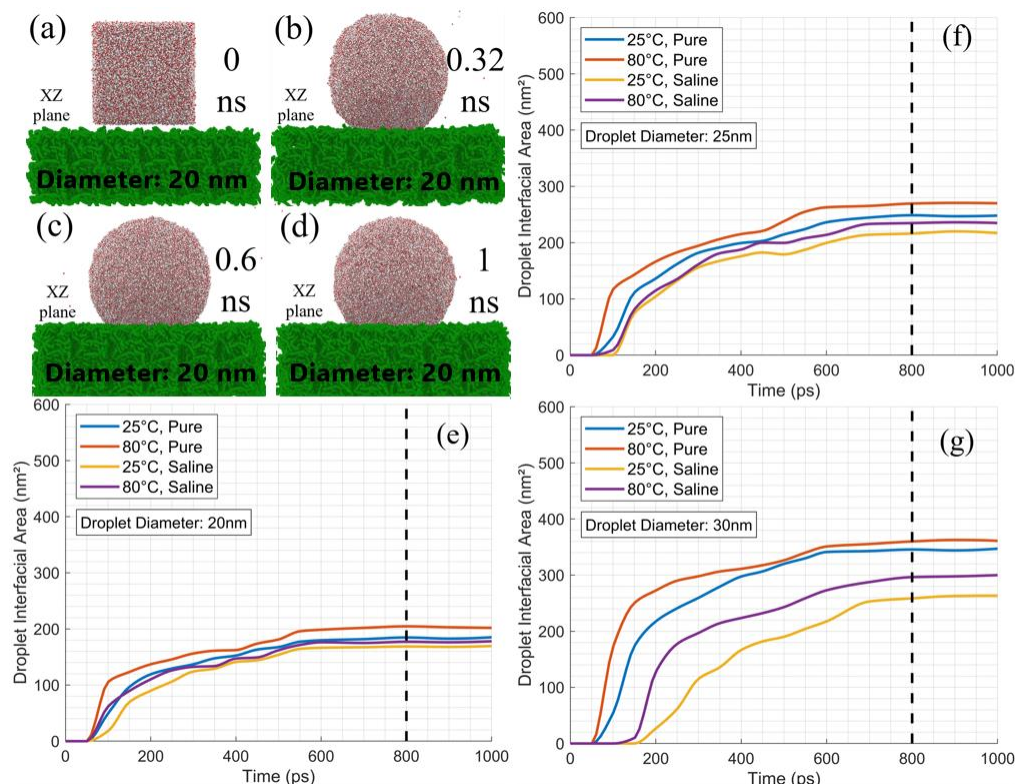


**Figure 21.** The equilibration of a 20 nm pure droplet on the PTFE surface at 25°C is shown in MD snapshots (a)–(d) at (a) 0 ns, (b) 0.32 ns, (c) 0.6 ns and (d) 1 ns in the XZ plane. (f), (e), and (g) display the interfacial area growth over time for 20 nm, 25 nm, and 30 nm droplets, respectively. (Note: dashed lines mark stabilization points.)

By 0.32 ns, the interaction becomes more pronounced, and the droplet flattens further against the surface. The process stabilized between 0.6 ns and 1 ns, where the droplet reached an equilibrium state, maintaining a consistent spherical cap with a constant volume (V) and strong surface adhesion. The total energies of the systems in Figure 22 were

observed to stabilize after initial fluctuations, indicating that equilibrium had been reached for each droplet size and condition, including variations in temperature and salinity.

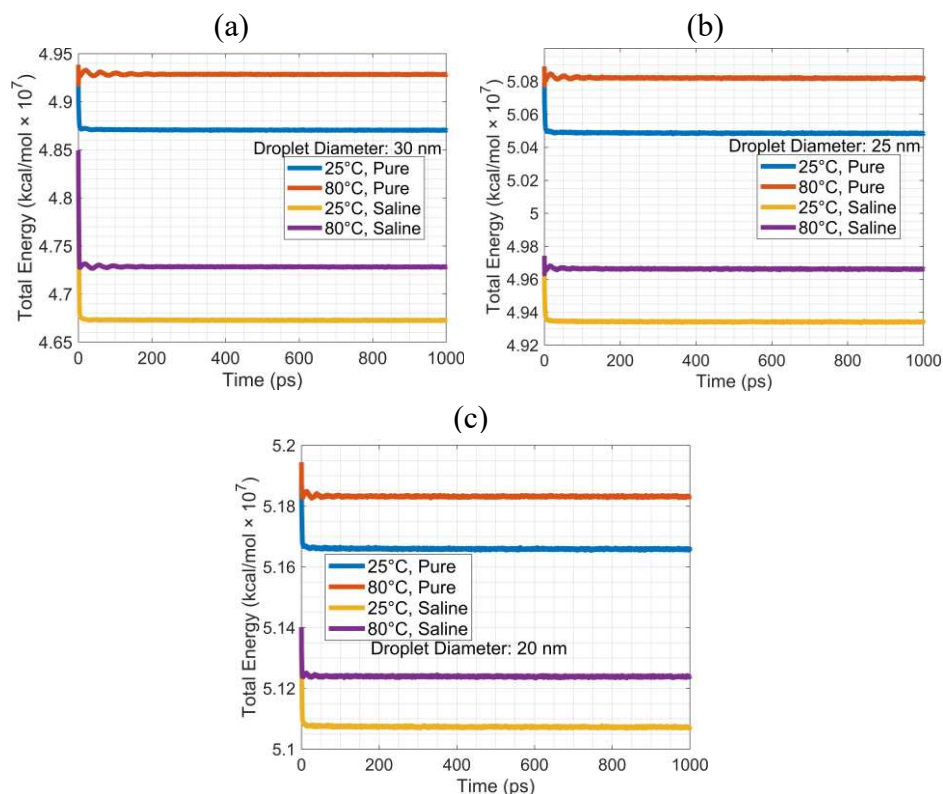


**Figure 22.** The total energies of the (a) 30 nm, (b) 25 nm, and (c) 20 nm droplet size as a function of simulation time.

Once the system had reached equilibrium, theoretical methods of the wetting process were used to calculate the contact angle. At equilibrium, the molecular dynamics data were stable. The wetting process, in equilibrium, was described by the molecular-kinetic theory (MKT) of Blake and Haynes [86] and was explained in terms of molecular interactions at the three-phase contact line, where the liquid, solid, and vapor phases meet, using the Eq. (A.30):

$$\frac{dR}{dt} = 2 K \lambda \sinh \left[ \frac{\gamma_{LV} (\cos \theta_0 - \cos \theta)}{2nk_B T} \right] \quad (A.30)$$

The friction coefficient for the motion of the contact line is given by the expression  $\zeta_0 = nk_B T / K\lambda$ , where  $n$  denotes the density of adsorption sites on the surface,  $k_B$  is Boltzmann's constant,  $K$  represents the displacement frequency, and  $\lambda$  is the spacing between adsorption sites. The  $\cos \theta_0$  represents the equilibrium contact angle, while  $\cos \theta$  is the current contact angle. For a droplet characterized by a spherical cap of volume  $V$ , the change of the contact angle  $\theta(t)$  was introduced by Blake and Haynes [86] and later formulated in Eq. (A.31) by Webb III et al. [87].

$$\frac{d\theta}{dt} = - \left( \frac{\pi}{3V} \right)^{1/3} \frac{(2 - 3 \cos \theta + \cos^3 \theta)^{4/3}}{(1 - \cos \theta)^2} \frac{dR}{dt} \quad (A.31)$$

where  $R$  is the radius of the droplet interfacial area ( $S$ ) of the spherical cap. The widely used MKT of wetting assumes a uniform surface with consistent liquid-solid interactions. Nevertheless, in practice, most surfaces displayed varying degrees of heterogeneity, including chemical irregularities, fouling, or surface roughness, which could influence wetting behavior [88]. Thus, the MKT was limited by often overlooking surface roughness. Hautman and Klein [89] introduced a method in Eq. (A.32) to relate the droplet's center of mass  $\langle z_{com} \rangle$  to the contact angle, assuming constant droplet density and using the equation  $\cos \theta = (1 - h/r)$ .

$$\langle z_{com} \rangle = 2^{-4/3} R_0 \left( \frac{1 - \cos \theta}{2 + \cos \theta} \right)^{1/3} \frac{3 + \cos \theta}{2 + \cos \theta} \quad (A.32)$$

where  $h$  is the height and  $r$  is the radius of the spherical cap. The  $z_{\text{com}}$  represents the  $z$ -coordinate of the droplet's center of mass relative to the solid surface, while  $\langle \dots \rangle$  indicates the time-averaged value. The  $R_0 = 3N / 4\pi\rho_0$  refers to the radius of the free sphere drop that best fits the droplet. The  $N$  represents the total number of molecules in the droplet, and  $\rho_0$  is the number density of the bulk liquid, which is  $0.033 \text{ \AA}^{-3}$  for water. Eq. (A.32) was applied to a pure droplet with a 20 nm, 25 nm, and 30 nm diameter at  $25^\circ\text{C}$ , as shown in Figure 23 (a,b,c), resulting in contact angles between 132-135 degrees, which is 11-14 degrees higher than the value obtained experimentally by Yijie Xiang et al. [90].

New methodologies have been developed to improve contact angle estimation from instantaneous droplet geometries due to inaccuracies in the MKT and center of mass formulations. The method proposed by Hautman and Klein [88] was improved by Fan and Cagin [91], who incorporated a more accurate approach for determining the center of mass of the droplet, thus eliminating prior assumptions about density uniformity. The height ( $h$ ) and radius ( $r$ ) of the optimal partial sphere fitting the droplet were determined, and the contact angle was directly calculated using the relationship  $\cos \theta = (1 - h/r)$ , based on the geometry of the spherical cap. Ruijter et al. [92] introduced a new technique to determine the best-fitted partial sphere by utilizing the droplet's density profile to pinpoint the liquid-gas interface. Although this technique was widely used for calculating the contact angle in MD simulations, it was noted that inconsistent results could arise, particularly for small droplets [93] and inhomogeneous surfaces [94]. To address these issues, a surface meshing technique was proposed by Santiso et al. [93], which estimated the local contact angle at various points along the three-phase contact line, calculated from the 3D structure of a droplet. However, it was acknowledged that the accuracy of this method, like other

methods relying on interface recognition, was heavily dependent on the density profile used to identify the contact layer. Their study highlighted that a fine mesh might mistakenly classify density fluctuations within the droplet as part of the interface.

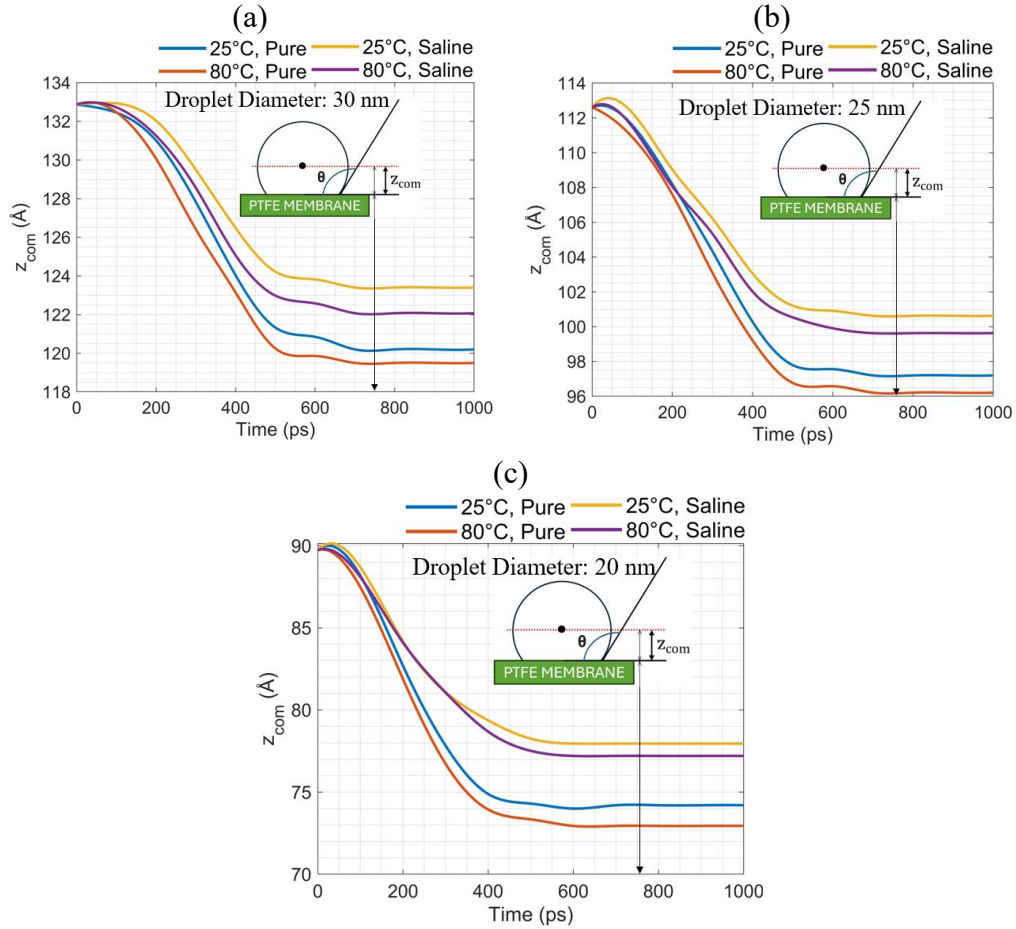


**Figure 23.** The effect of temperature and salinity on the height of the droplet mass center (a) 30 nm, (b) 25 nm, and (c) 20 nm droplets on a PTFE surface.

Khalkhali et al. [95] employed a convex hull algorithm to represent the droplet surface using triangles, with the angles between vectors normal to these triangles and the solid surface being calculated, without requiring any prior assumptions about the shape of the liquid droplet or reliance on the density profile. Considering that rough surfaces led to more



complex contact line geometries, the nuances of contact angle hysteresis or local variations due to surface roughness might not have been fully captured by this method. Considering all this, our approaches were applied to measure the equilibrium contact angle schematically shown in Figure 24. After reaching equilibrium, as shown in Figure 24a, Planes, each 3 nm thick, were defined and oriented perpendicular to the xz and yz planes. Areas outside the specified center planes, highlighted in red in Figure 24b, were removed. In the remaining part of the simulation model, the measurements of root mean square roughness ( $R_q$ ) and average roughness ( $R_a$ ) measurements were performed first. Mathematically,  $R_q$  and  $R_a$  are defined in Eq. (A.33):

$$R_q = \sqrt{\frac{1}{N} \sum_{i=1}^N (z_i - \bar{z})^2}, \quad R_a = \frac{1}{N} \sum_{i=1}^N |z_i - \bar{z}| \quad (\text{A.33})$$

where  $N$  is the total number of surface points analyzed,  $z_i$  represents the height of the  $i$ -th point on the surface and  $\bar{z}$  is the average height of all points. Once the  $z$ -axis values for all droplet configurations were adjusted to the same baseline, the data below this  $z$ -axis, highlighted in red in Figure 24c, were excluded from the analysis. The resulting rough PTFE surface was filtered to include only the  $x$  and  $y$  ranges corresponding to the droplet's spreading area contact. Following this, the roughness parameters  $R_q$  and  $R_a$  were calculated using the adjusted and filtered  $z$ -values. This adjustment ensured the contact angle calculations were based on PTFE baselines with consistent roughness across all configurations analyzed.

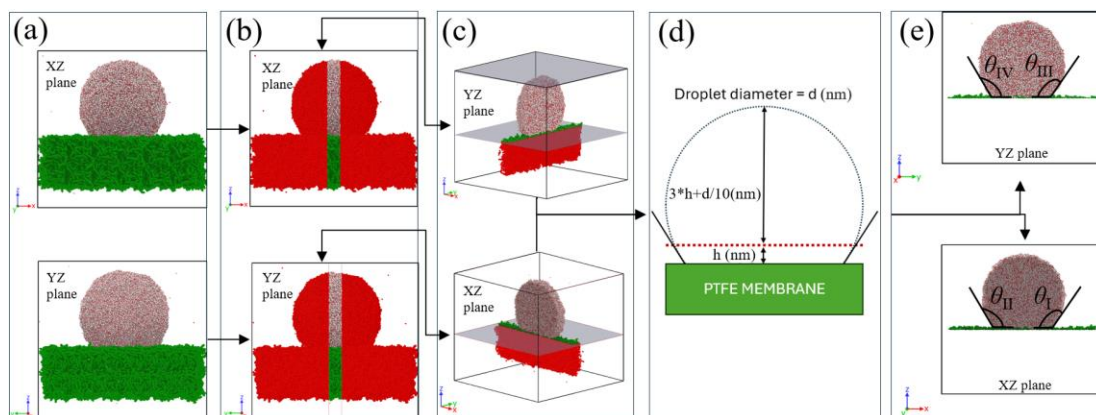


**Figure 24.** Methodology for 20 nm droplet contact angle measurement: (a) Equilibration at 25°C in XZ and YZ views, (b) 30 Å central section removed, (c) Cross-sections post-removal, (d) Contact angle equation, (e) Tangent-based angle determination with PTFE surface.

The density contours of the droplet were generated for each configuration using the data from Figure 24c by dividing the space within the droplet into small, distinct bins: in the xz plane ( $\Delta x = 0.3$  nm,  $\Delta z = 0.3$  nm,  $\Delta y = 3$  nm) and in the yz plane ( $\Delta y = 0.3$  nm,  $\Delta z = 0.3$  nm,  $\Delta x = 3$  nm). Each bin collected water molecule data to identify the water/vapor boundary, where the water density reached 0.5 g/cm<sup>3</sup> [21]. Once the droplet's water/vapor boundary, depicted by the dashed semicircular line in Figure 24d, was established, the vertical distance from the PTFE membrane surface to the apex of the droplet was measured using MD trajectory data. This distance remains constant throughout all MD simulations at different times depending on the droplet size, but in all cases, equilibrium was achieved after the simulation time reached 0.8 ns. Thus, the value of  $h$  in the equation shown in Figure 24d was proportional across all droplet configurations. Once the boundary was established, data points along the water/vapor interface in the XZ and YZ planes were extracted. These data points ideally captured the curvature of the droplet at its edges, where it met the PTFE surface. At the points where the droplet interface met the PTFE surface, a

curve-fitting approach was used to approximate the slope. This process involved fitting a circular arc to the extracted boundary points, after which the slope was calculated at the contact points to the height  $h$ . The tangent lines were defined by the slope at these contact points. The contact angles ( $\theta_I$ ,  $\theta_{II}$  on the xz plane and  $\theta_{III}$ ,  $\theta_{IV}$  on the yz plane), as shown in Figure 24e, the contact angles were measured between tangent lines and then averaged. Plane views of 30, 25, and 20 nm droplets at 1 ns are in Figures 25, 26, and 27. The study examined salinity and temperature effects on contact angle variation using 30 nm droplets with 8.45% salinity, pure droplets at 25°C and 80°C on PTFE, and free-floating droplets. Ion concentration and water density profiles were plotted, with discrepancies further analyzed using the radial distribution function (RDF), which quantified NaCl spatial distribution and revealed impacts on interfacial properties and contact angles.

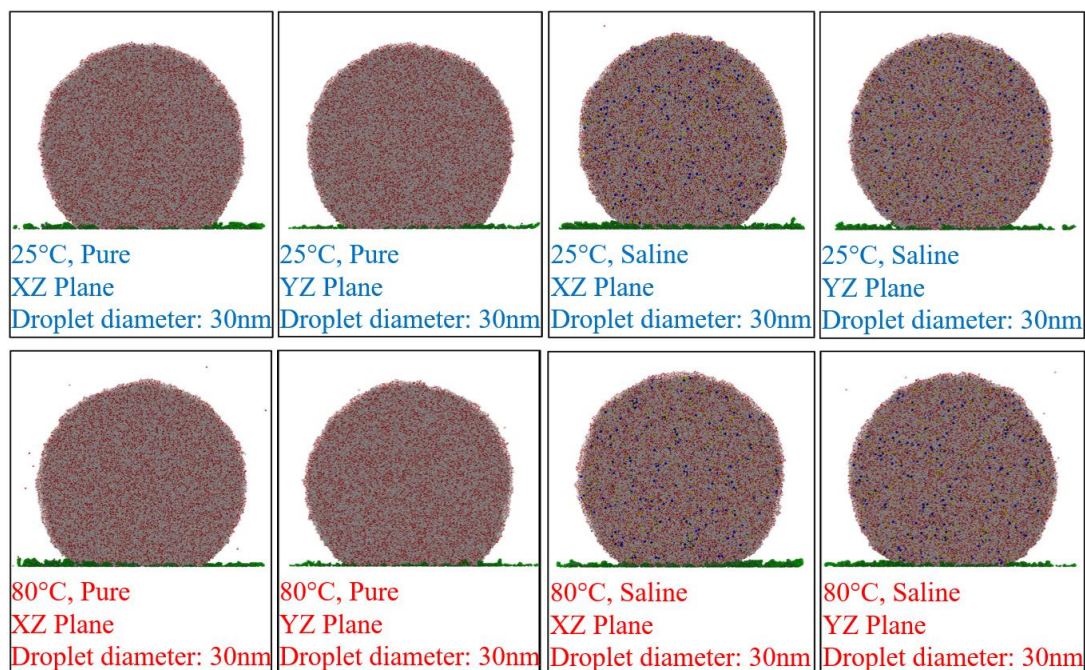


**Figure 25.** This figure illustrates the interaction of 30 nm droplets with rough, amorphous PTFE surfaces at two temperatures (25°C and 80°C) and two salinities (pure water and saline) across different planes (XZ and YZ).

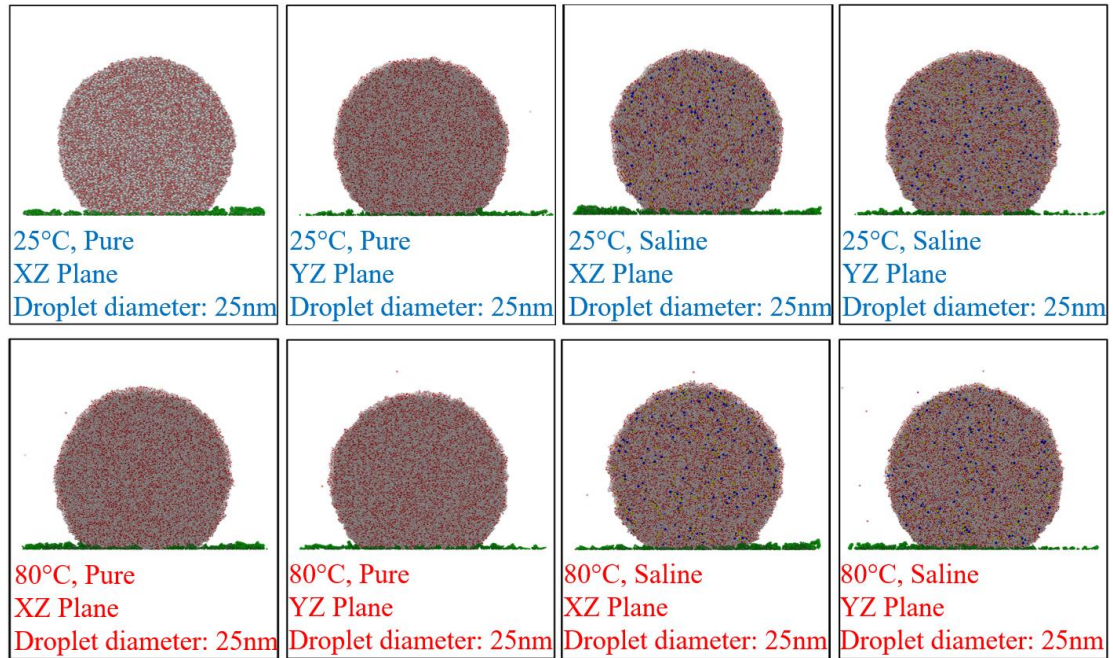


**Figure 26.** This figure illustrates the interaction of 25 nm droplets with rough, amorphous PTFE surfaces at two temperatures (25°C and 80°C) and two salinities (pure water and saline) across different planes (XZ and YZ).

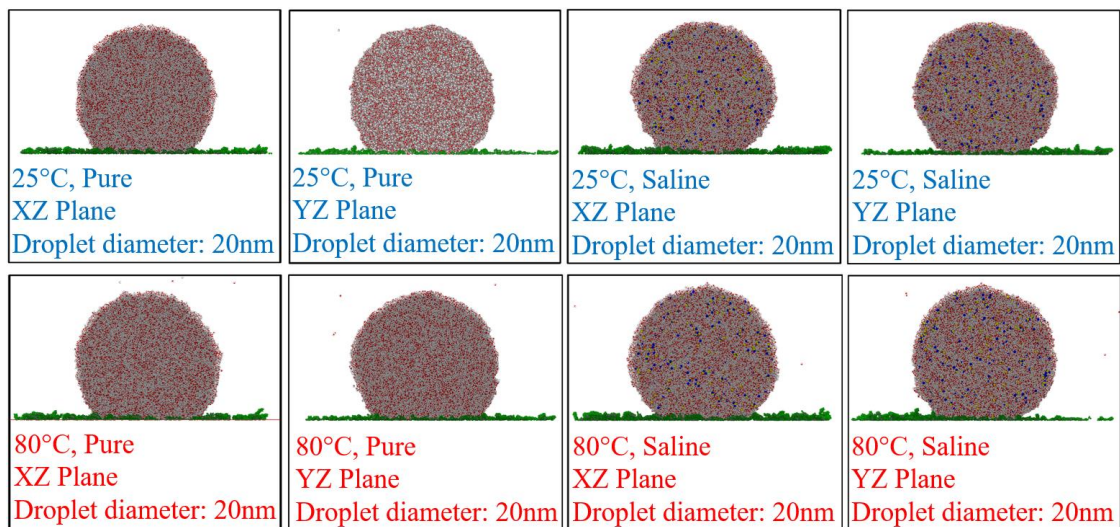


**Figure 27.** This figure illustrates the interaction of 20 nm droplets with rough, amorphous PTFE surfaces at two temperatures (25°C and 80°C) and two salinities (pure water and saline) across different planes (XZ and YZ).



### 5.3. Results and discussion

In Figures 28a and 28b, the density contour was refined by excluding bins with densities above 0.5 g/cm<sup>3</sup> [21], effectively isolating the water phase and enabling precise definition of the water/vapor interface. The relationship derived from Figure 24d was then systematically applied to each equilibrated cubic configuration to calculate the contact angle, ensuring consistency across different droplet setups.

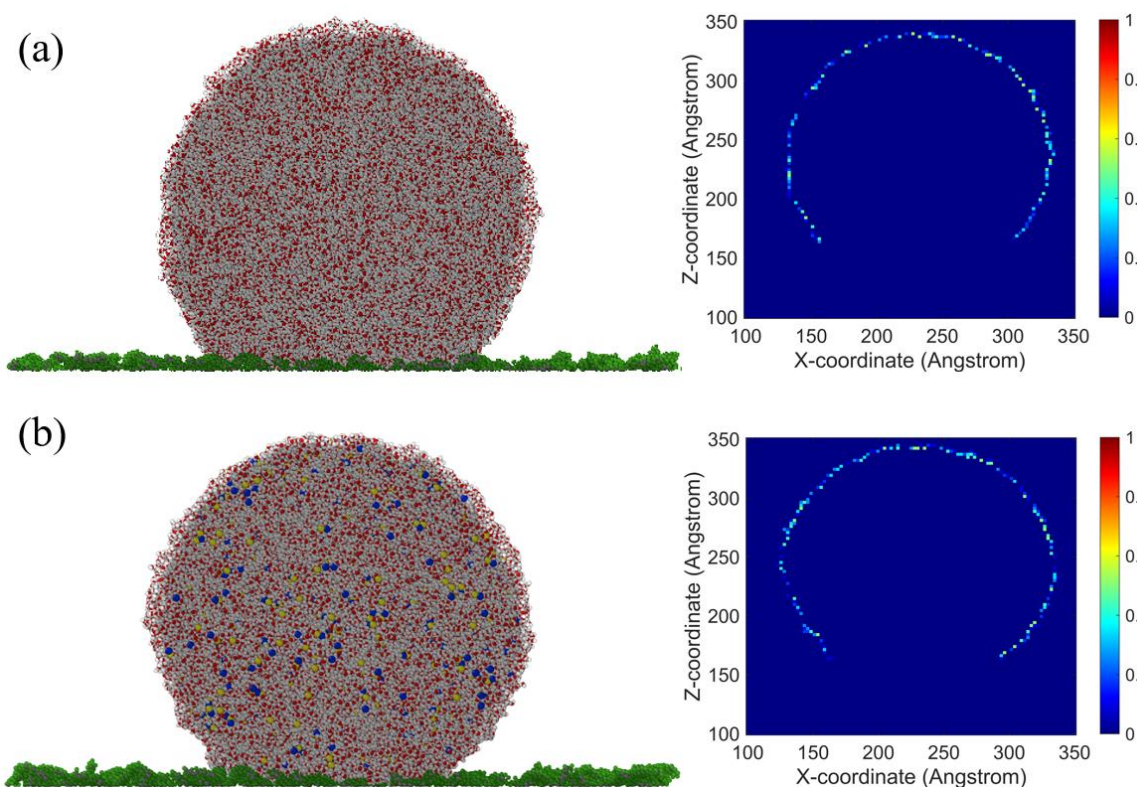


**Figure 28.** Effect of salinity on the contact angle of droplets on a PTFE surface: Visualization of 20 nm diameter pure (a) and 8.45% saline (b) water droplets, each 3 nm thick, on a PTFE surface at 25°C in the XZ plane, including density contours.

Detailed measurements for each droplet configuration, capturing variations in size and interfacial characteristics, are presented in Figures 29, 30, 31, 32, 33, and 34, illustrating how these conditions influence interfacial properties and the resulting contact angles.

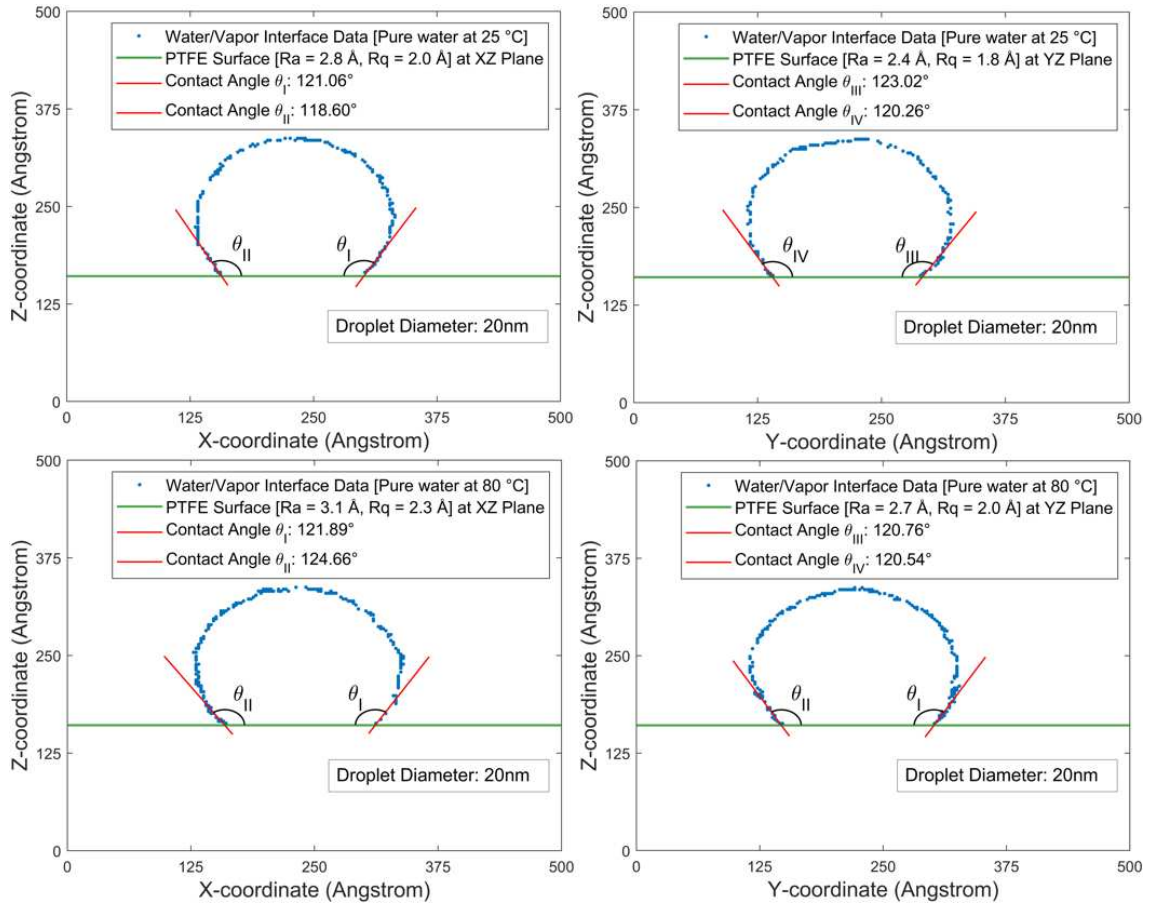


**Figure 29.** This figure shows contact angle measurements of 20 nm pure droplets on rough, amorphous PTFE surfaces, including water/vapor interface data, PTFE surface roughness (Ra, Rq), and calculated contact angles ( $\theta_{xz}$ ,  $\theta_{yz}$ ).

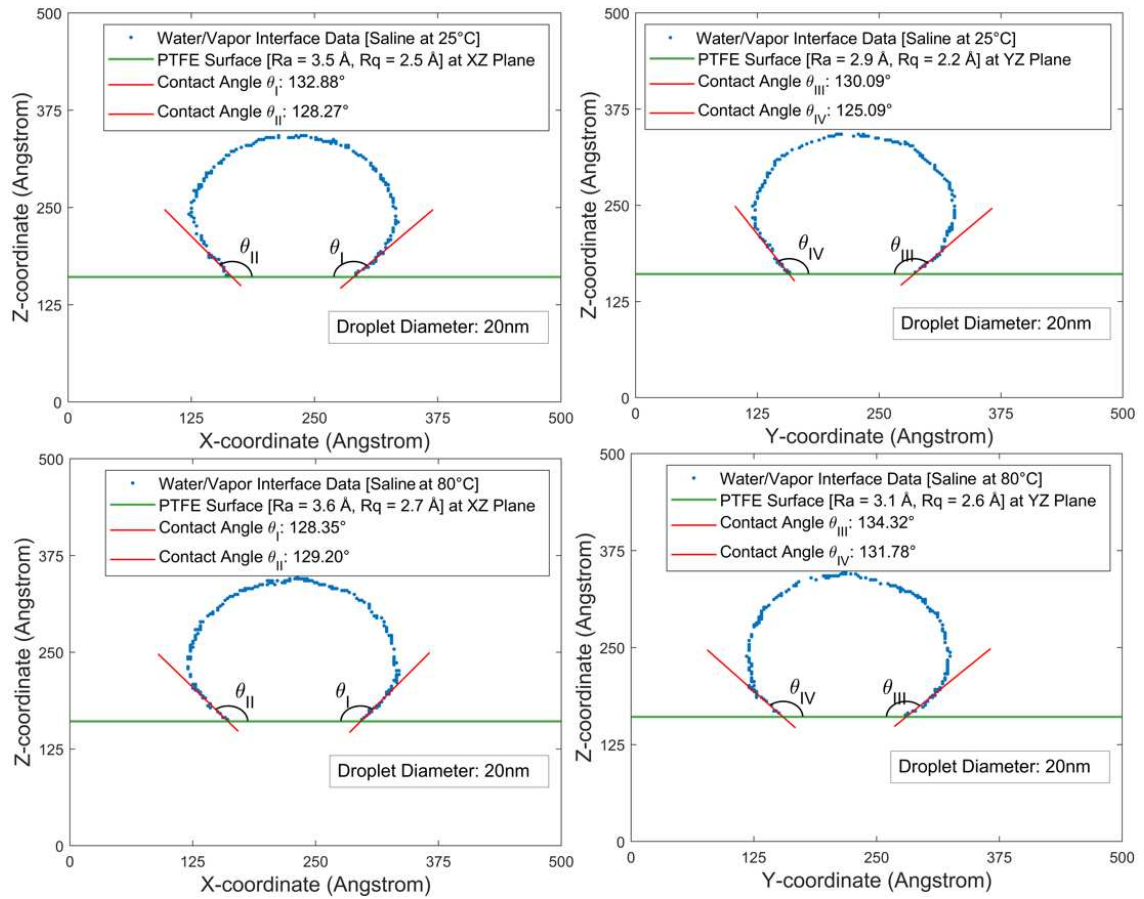


**Figure 30.** This figure shows contact angle measurements of 20 nm saline droplets on rough, amorphous PTFE surfaces, including water/vapor interface data, PTFE surface roughness (Ra, Rq), and calculated contact angles ( $\theta_{xz}$ ,  $\theta_{yz}$ ).

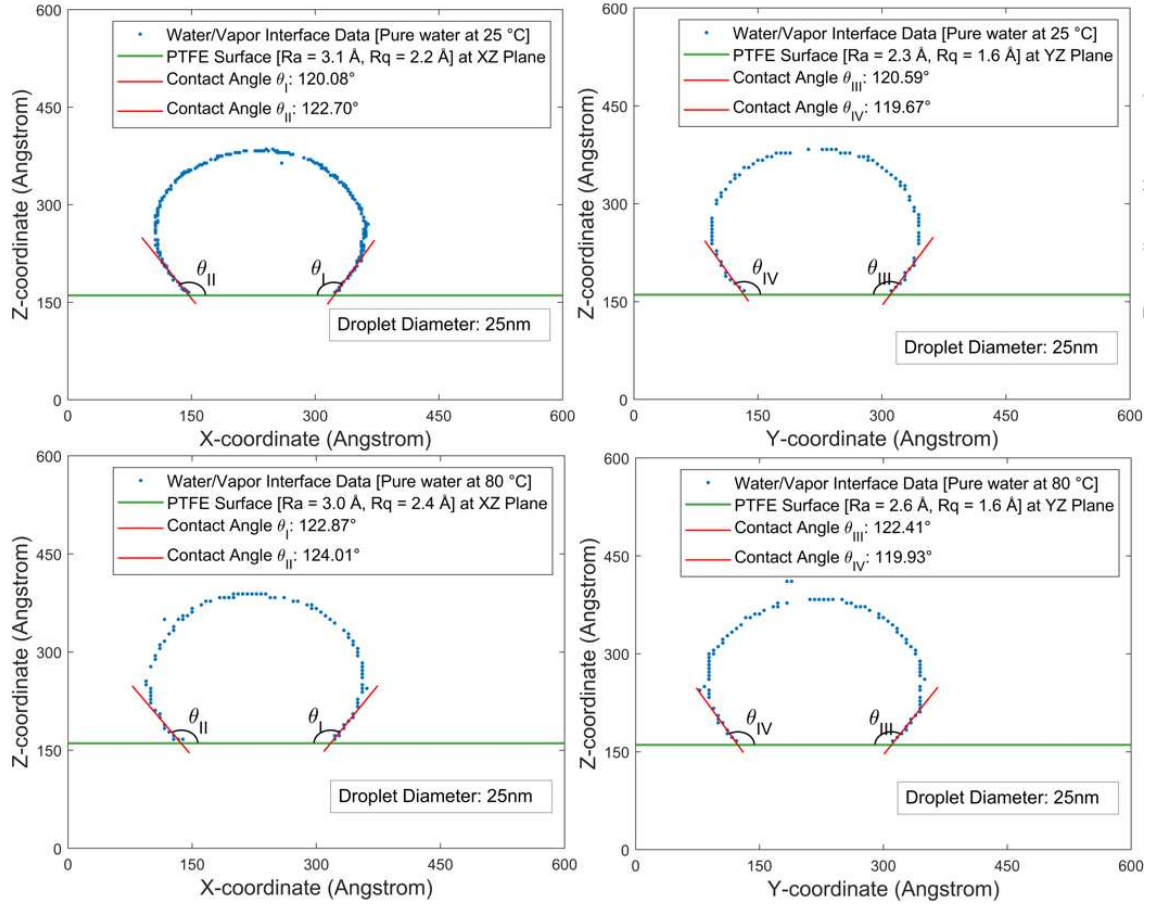


**Figure 31.** This figure shows contact angle measurements of 25 nm pure droplets on rough, amorphous PTFE surfaces, including water/vapor interface data, PTFE surface roughness ( $Ra$ ,  $Rq$ ), and calculated contact angles ( $\theta_{xz}$ ,  $\theta_{yz}$ ).



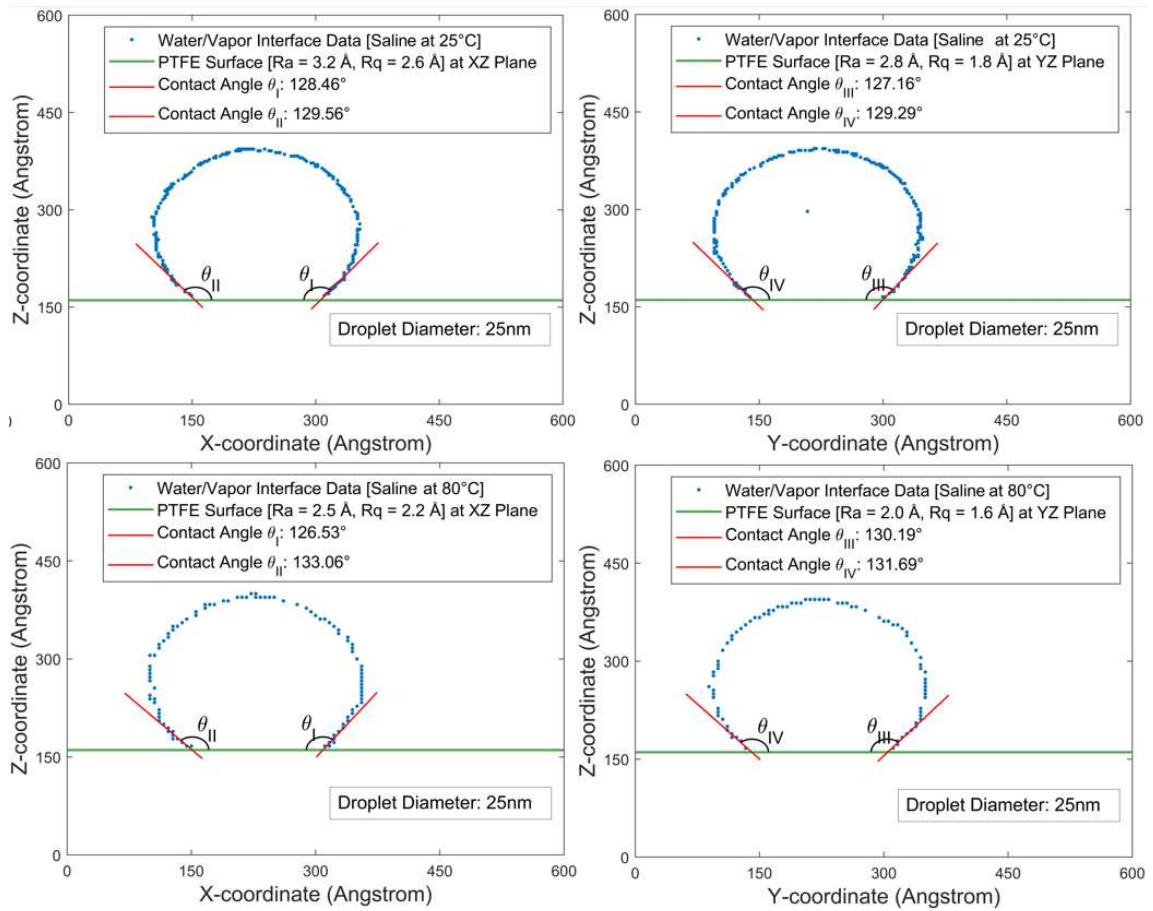


**Figure 32.** This figure shows contact angle measurements of 25 nm saline droplets on rough, amorphous PTFE surfaces, including water/vapor interface data, PTFE surface roughness (Ra, Rq), and calculated contact angles ( $\theta_{xz}$ ,  $\theta_{yz}$ ).

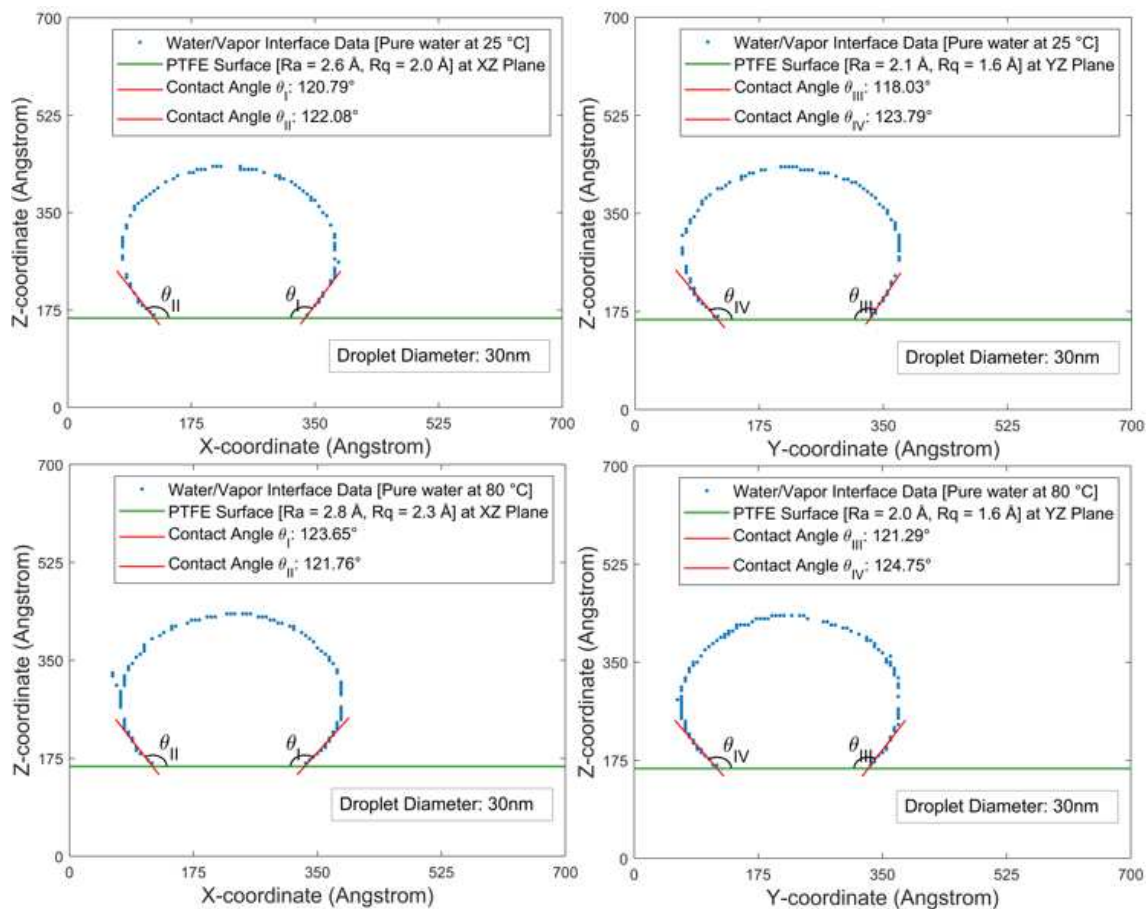


**Figure 33.** This figure shows contact angle measurements of 30 nm pure droplets on rough, amorphous PTFE surfaces, including water/vapor interface data, PTFE surface roughness ( $Ra$ ,  $Rq$ ), and calculated contact angles ( $\theta_{xz}$ ,  $\theta_{yz}$ ).

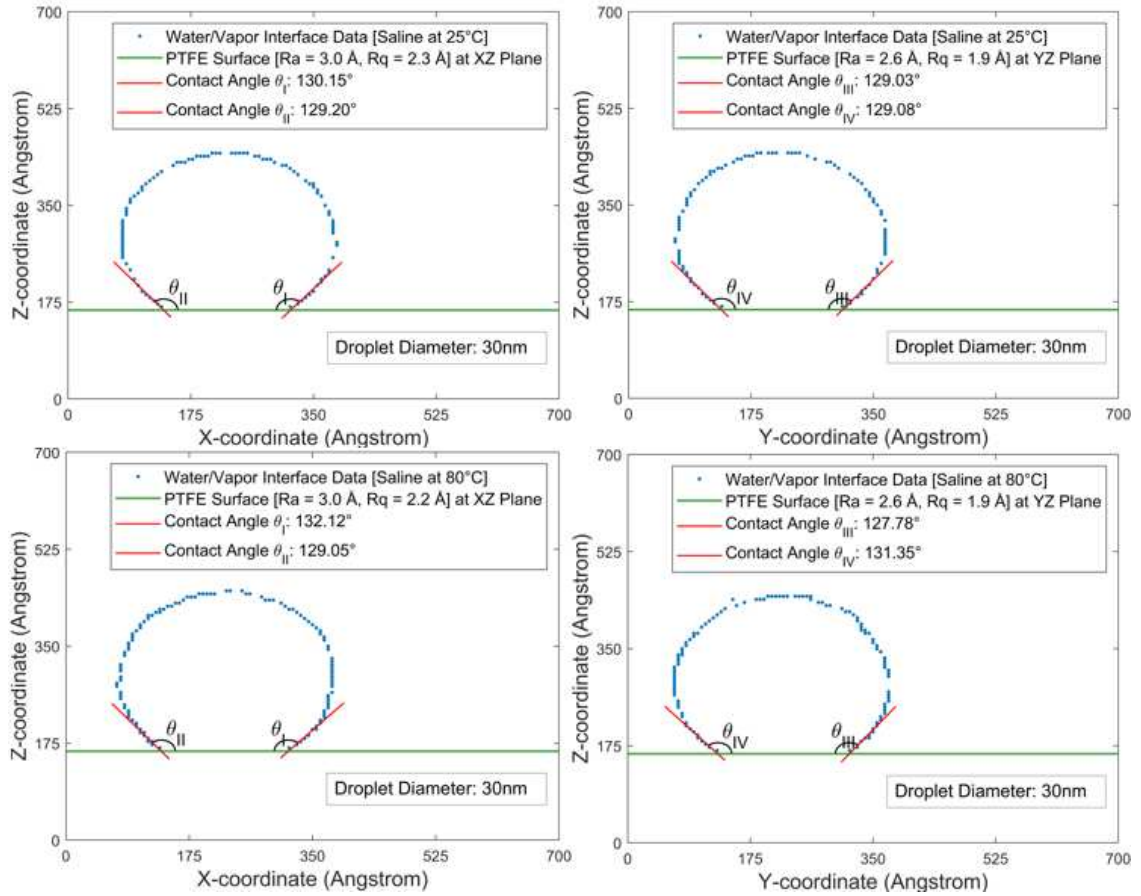


**Figure 34.** This figure shows contact angle measurements of 30 nm saline droplets on rough, amorphous PTFE surfaces, including water/vapor interface data, PTFE surface roughness (Ra, Rq), and calculated contact angles ( $\theta_{xz}$ ,  $\theta_{yz}$ ).

All these detailed measurements, including the surface roughness values, are presented comprehensively in Table 20. This table compares the data highlighting the variations and trends observed across different samples.

**Table 20.** This table presents the contact angles measured for droplets of various diameters (ranging from 20 nm to 30 nm) interacting with rough, amorphous PTFE surfaces. The data includes the effects of different temperatures (25°C and 80°C) and salinities (pure water and saline).

Case	Roughness ( Å )	$\theta_I^\circ$	$\theta_{II}^\circ$	$\theta_{III}^\circ$	$\theta_{IV}^\circ$	Contact Angle°
30 nm	XZ: Ra:2.6, Rq:2.0	120.79	122.08			121.17
25°C, Pure	YZ: Ra:2.1, Rq:1.6			118.03	123.79	
30 nm	XZ: Ra:2.8, Rq:2.3	123.65	121.76			122.86
80°C, Pure	YZ: Ra:2.0, Rq:1.6			121.29	124.75	
30 nm,	XZ: Ra:3.0, Rq:2.3	130.15	129.20			129.37
25°C, Saline	YZ: Ra:2.6, Rq:1.9			129.03	129.08	
30 nm	XZ: Ra:3.0, Rq:2.2	132.12	129.05			130.08
80°C, Saline	YZ: Ra:2.6, Rq:1.9			127.78	131.35	
25 nm	XZ: Ra:3.1, Rq:2.2	120.08	122.70			120.76
25°C, Pure	YZ: Ra:2.3, Rq:1.6			120.59	119.67	
25 nm	XZ: Ra:3.0, Rq:2.4	122.87	124.01			122.31
80°C, Pure	YZ: Ra:2.6, Rq:1.6			122.41	119.93	
25 nm	XZ: Ra:3.2, Rq:2.6	128.46	129.56			128.62
25°C, Saline	YZ: Ra:2.8, Rq:1.8			127.16	129.29	
25 nm	XZ: Ra:2.5, Rq:2.2	126.53	133.06			130.37
80°C, Saline	YZ: Ra:2.0, Rq:1.6			130.19	131.69	
20 nm	XZ: Ra:2.8, Rq:2.0	121.06	118.60			120.74
25°C, Pure	YZ: Ra:2.4, Rq:1.8			123.02	120.26	
20 nm	XZ: Ra:3.1, Rq:2.3	121.89	124.66			121.96
80°C, Pure	YZ: Ra:2.7, Rq:2.0			120.76	120.54	
20 nm	XZ: Ra:3.5, Rq:2.5	132.88	128.27			129.08
25°C, Saline	YZ: Ra:2.9, Rq:2.2			130.09	125.09	
20 nm	XZ: Ra:3.6, Rq:2.7	128.35	129.20			130.91
80°C, Saline	YZ: Ra:3.1, Rq:2.6			134.32	131.78	

The saline mass concentrations were changed at the end of the 1 ns due to vaporization. Thus, mass concentrations had been measured for all droplet cases in Table 21. The 1 ns results were shown to be comparable to each other, as the 30 nm case was only 0.01% higher, which was considered a negligible difference.

**Table 21.** Comparison of NaCl concentration changes for different sizes of nanodroplets at the end of 1 ns at 25°C and 80°C.

Configurations	C <sub>NaCl</sub> (%)		Configurations	C <sub>NaCl</sub> (%)	
	0 ns	1 ns		0 ns	1 ns
30 nm (25 °C)	8.45%	8.47%	25 nm (80 °C)	8.45%	8.50%
30 nm (80 °C)	8.45%	8.51%	20 nm (25 °C)	8.45%	8.46%
25 nm (25 °C)	8.45%	8.46%	20 nm (80 °C)	8.45%	8.50%

Two distinct effects were observed when the contact angle values from all equilibrated cubic configurations were plotted, including the lowest and highest measured contact angle values, as shown in Figure 35. **Temperature effect:** A slight increase in the contact angle with increased temperature was observed for all saline and pure droplets. Higher contact angles were shown by both pure and saline droplets at 80°C compared to 25°C, indicating that the wettability of the hydrophobic surface was indeed influenced by temperature. **Salinity Effect:** The contact angle was consistently larger for saline systems than pure water systems across all droplet sizes (20, 25, and 30 nm). The effect of salinity on contact angle was more pronounced, increasing approximately 8-9 degrees, suggesting that the presence of salt in the water significantly altered the interaction between the droplet and the surface, leading to a higher contact angle. The impact of salinity and temperature on a 30 nm droplet was further investigated in the following section.

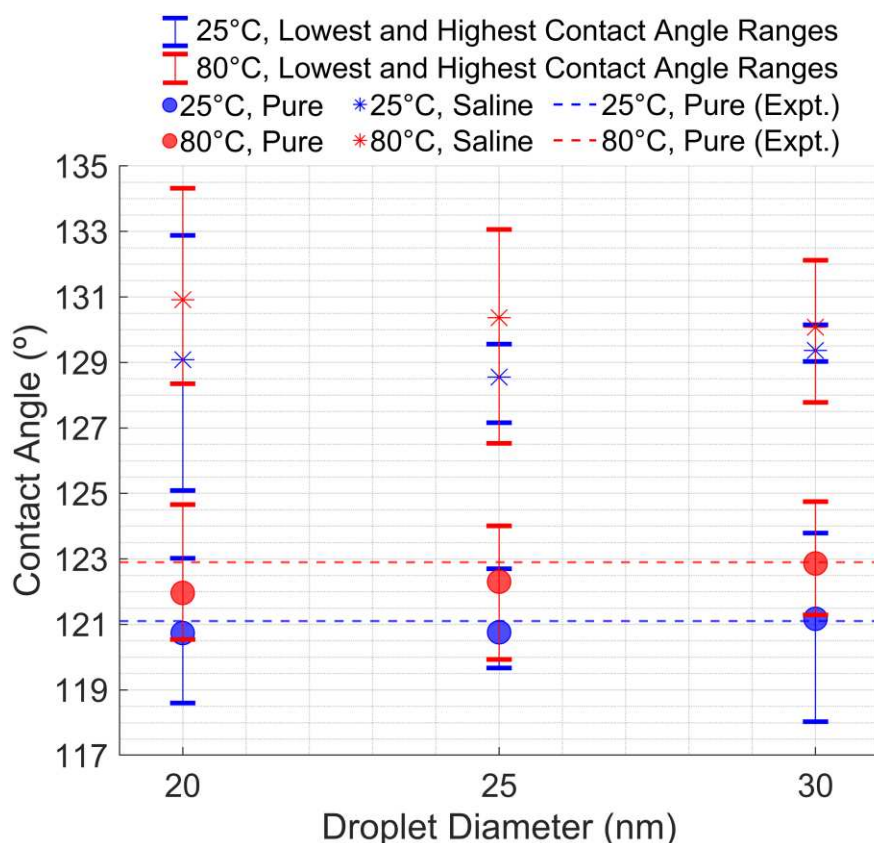


**Figure 35.** The graph shows contact angle variation with size, salinity, and temperature. Dashed red and blue lines mark the experimental 2 mm droplet angles, as referenced [90].

### 5.3.1. Salinity and temperature effects

The impact of salinity and temperature on contact angle variation was studied using 30 nm droplets with 8.45% salinity, pure droplets on PTFE at 25°C and 80°C, and free-floating droplets at the same temperatures. The initial analysis involved dividing the free-floating droplets into spherical shells 0.25 nm thick, starting from 1.5 nm away from the center of mass (COM) and extending outward, with the region within 1.5 nm of the COM considered the bulk. A detailed analysis of a NaCl nanodroplet, including ion mass concentration and water density at 25°C and 80°C over timescales of 1 ns and 2 ns, is presented in Figure 34a and Figure 36b. Saturated vapor pressures were calculated using the ideal gas law, reaching

equilibrium between 0.4 and 1 ns at 80°C and between 0.3 and 1 ns at 25°C, as shown in Figure 36c.

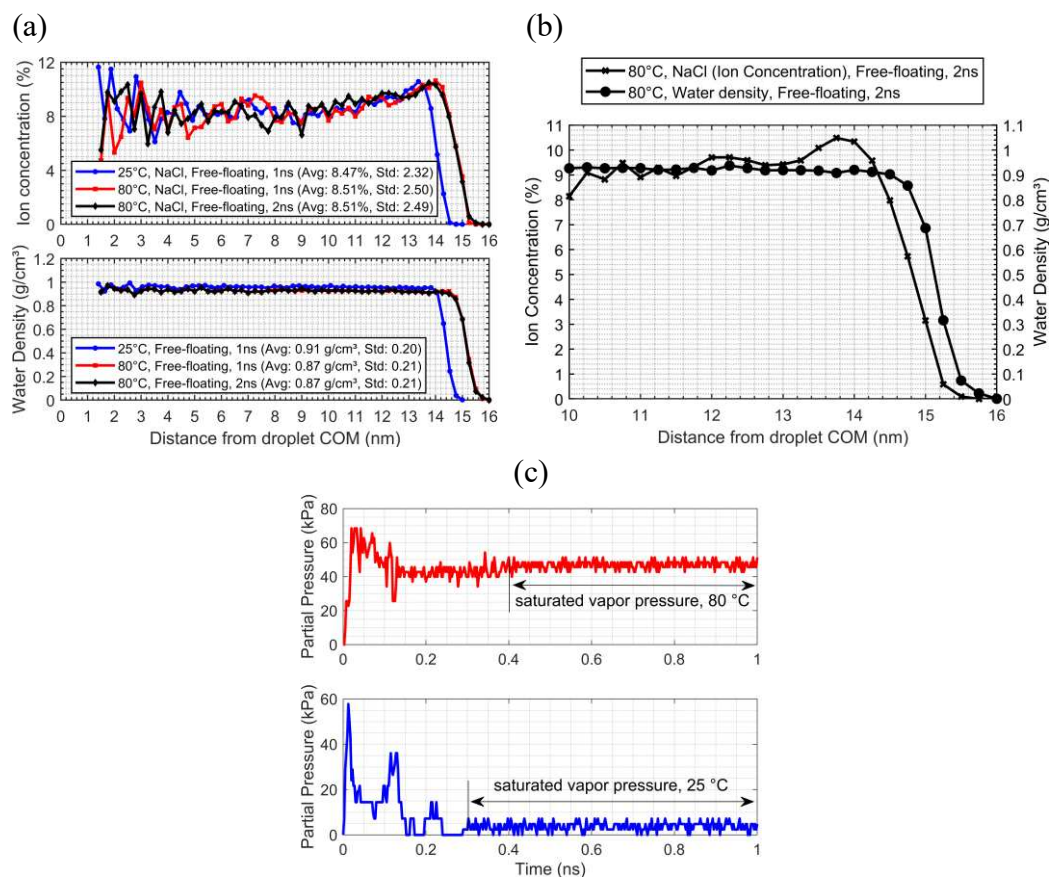


**Figure 36.** (a) Ion mass concentration and water density profiles, and (c) partial pressure of a NaCl nanodroplet at 25°C and 80°C over time. (Note: Avg is average intensity and Std is standard deviation).

At equilibrium, the rates of evaporation and condensation were found to be equal, stabilizing the system. Ion mass concentration in the free-floating droplets progressively migrated toward the surface, indicating surface segregation in Figures 37a and b. At 80°C, the peak shifted outward compared to 25°C, consistent with thermal expansion. Surface segregation in the 80°C, 2-ns simulation aligned with the 1-ns run. The ion concentration



curve increased from around 13 nm to a peak at 13.8-14 nm, then declined sharply, showing that NaCl ions tended to accumulate near the droplet surface. Meanwhile, water density remained constant until 13.8-14 nm, after which it dropped sharply, marking the liquid-vapor transition and confirming surface segregation. This methodology was applied to 30 nm droplets at 25°C on PTFE. However, the droplet could not maintain its spherical shape on the surface, complicating direct comparison with a free-floating droplet due to the lack of symmetry needed for spherical shell analysis, as shown in Figure 37a. This non-uniformity required a different approach, so the cylindrical segments method was applied to determine z-profiles, as illustrated in Figure 35. The first center of mass (COM) was identified, and the  $R_{\text{analyze}}$  radius was determined based on the droplet's  $R_{\text{base}}$  radius, shown in Figure 37b.

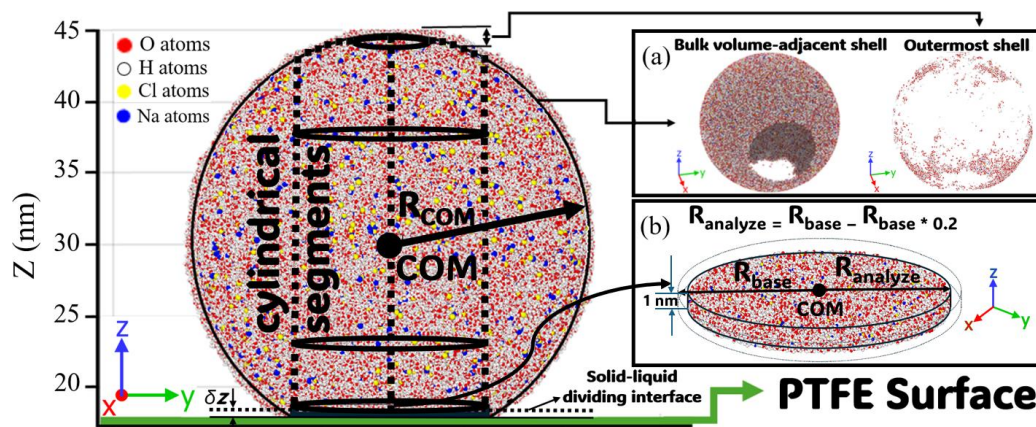


**Figure 37.** Visualization of the analysis setup for a 30 nm diameter droplet at 25°C in the YZ plane, used to assess the effects of salinity and temperature.

The PTFE and free-floating droplets were then segmented along the area defined by  $R_{\text{analyze}}$  and divided into 0.3 nm thick sections along the z-axis to analyze NaCl mass concentration and density distributions in Figure 38a.



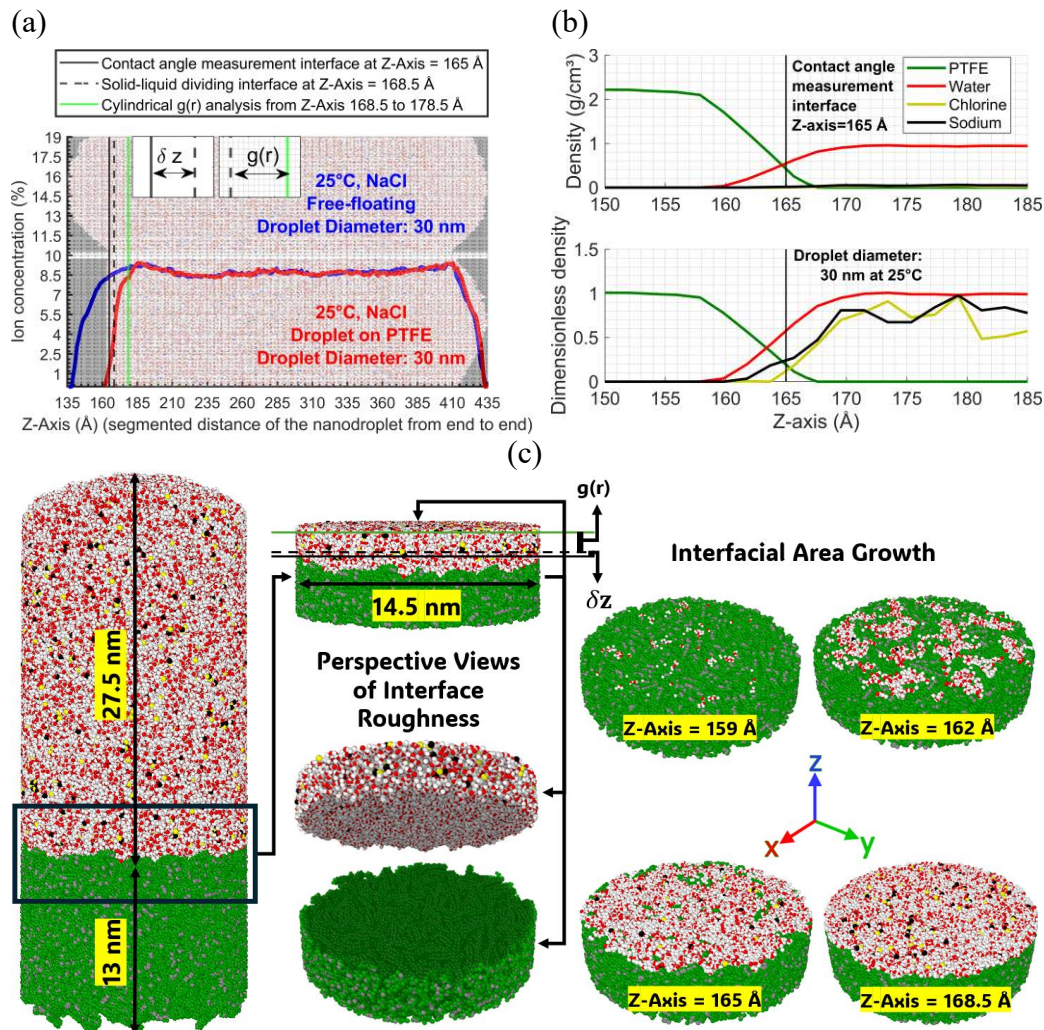


**Figure 38.** Ion mass concentration and density profiles of 30 nm NaCl nanodroplets: (a) Comparison between Free-floating and PTFE-adsorbed droplets, and (b) density and dimensionless density distributions near the PTFE Interface. (Note: The densities in the droplets have been normalized using the reference densities of PTFE, water, Na, and Cl.) (c) Visualization of interfacial roughness and spreading area growth.

The ion concentration was approximately 1% below the contact angle measurement interface in Figure 38b, increasing to 4% at the solid-liquid dividing interface. At the upper limit of the cylindrical analysis assembly, the ion concentration reached 8.5%,

demonstrating significant segregation of ions away from the PTFE surface. In the intermediate regions, the ion concentration profiles for both the free-floating droplet and the droplet on PTFE showed similar behavior, suggesting that surface interactions primarily affected ions near the PTFE-liquid interface. Thus, this region was magnified in Figure 38b to show density and dimensionless density and visualized as a perspective view of the interface roughness and interfacial area growth in Figure 38c. The ion concentration distribution revealed discrepancies between the free-floating and PTFE droplets. These discrepancies were further examined using radial distribution function (RDF) analysis, focusing on  $g(r)$  for 1 nm-thick samples from the Z-axis range of 168.5 Å to 178.5 Å in Figure 38c to ensure that surface roughness ( $\delta z$ ) effects were excluded. This range also represents the spreading area at the solid-liquid interface, which determines the contact angle. Therefore, the RDF results were investigated for interactions between  $\text{Na}^+$  ions,  $\text{Cl}^-$  ions, and water molecules, along with temperature-related effects on the spreading area and contact angle.

The RDF results are presented in Figure 39 for sodium-oxygen ( $g_{\text{Na-O}}(r)$ ), chloride-oxygen ( $g_{\text{Cl-O}}(r)$ ), sodium-hydrogen ( $g_{\text{Na-H}}(r)$ ), and chloride-hydrogen ( $g_{\text{Cl-H}}(r)$ ) interactions for saline nanodroplets under different temperature conditions in the presence and absence of a PTFE membrane. These peaks were then matched with experimental data shown in Table 22. The analysis revealed distinct ion-specific hydration structures influenced by temperature and salinity. The 25°C, Saline, Free-floating condition exhibited the highest peak intensity in all cases. The 25°C, Saline, PTFE, and 80°C, Saline, Free-floating cases had equal intensities, while the 80°C, Saline, PTFE condition consistently showed the lowest peak. This trend was observed across all RDF plots, indicating stronger ion-water

interactions in free-floating droplets at 25°C and weaker interactions near the PTFE membrane, especially at 80°C.

**Table 22.** Comparison of the positions of the first peaks in the radial distribution functions of experimentally obtained NaCl solutions, their standard deviations (in parentheses), and the MD simulation in this study.

RDF pairs	Methods		
	x-ray spectra	neutron diffraction	MD (this study)
Na-O	2.35	2.34 (0.14)	2.35
Na-H	-----	2.97 (0.12)	3.05 (0.15)
Cl-O	3.20	3.16 (0.11)	3.25
Cl-H	-----	2.19 (0.16)	2.25 (0.10)

The X-ray spectra peaks were obtained from reference [96], with a spatial resolution of  $Q_{\text{Max}} = 24 \text{ \AA}^{-1}$ , and the neutron diffraction peaks were obtained from reference [97], with a spatial resolution of  $Q_{\text{Max}} = 16 \text{ \AA}^{-1}$ .

In Figure 39a, the primary peak  $g_{\text{Na-O}}$ , observed at  $r = 2.35 \text{ \AA}$ , was identified as corresponding to the first hydration shell of water molecules surrounding the sodium ion [96]. The lowest peak intensity was consistently observed in the PTFE case, indicating that weaker ion-water interactions occurred near the PTFE surface at elevated temperatures. Similar hydration behavior of sodium ions was observed at both 25°C, Free, and 80°C, PTFE, suggesting that the structural organization of water around sodium ions was comparably disrupted with temperature and membrane effects. Figure 39b displays the  $g_{\text{Cl-O}}(r)$  with a first peak at  $r=3.25 \text{ \AA}$ . Similar to in Figure 39a, the 25°C, Saline, and Free-floating cases demonstrated the highest peak intensity, while the 25°C, Saline, PTFE, and 80°C, Saline, and Free-floating cases exhibited equal intensities. The 80°C, Saline, PTFE condition exhibited the lowest peak intensity, indicating a reduction in ion-water structuring near the membrane at higher temperatures.

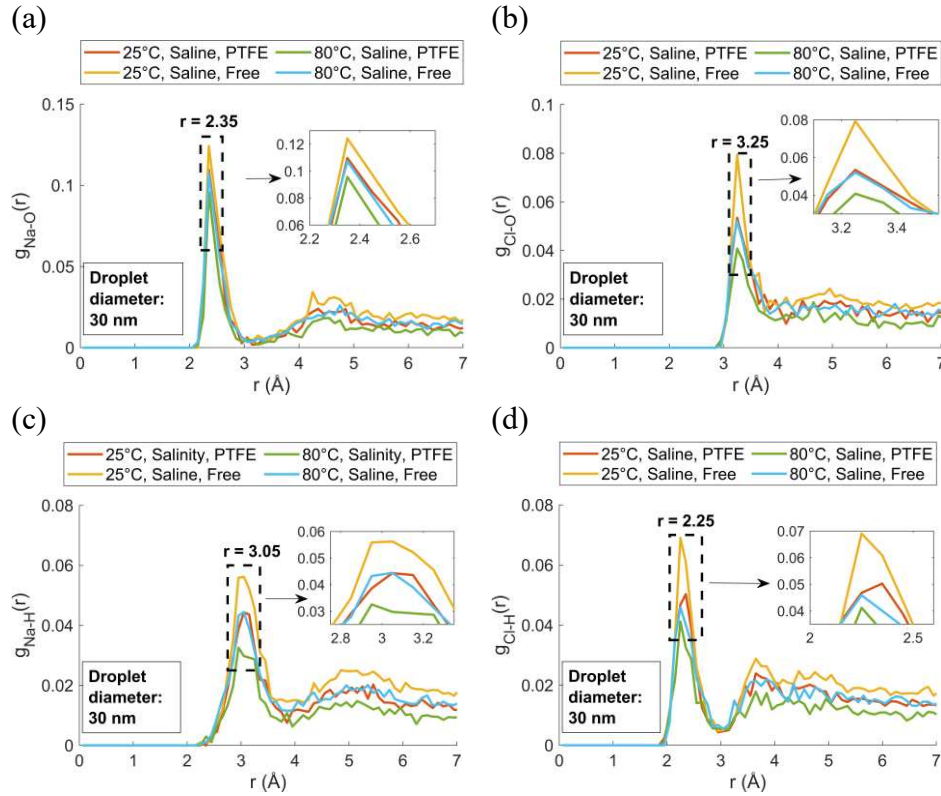


**Figure 39.** Radial distribution functions for atoms under different temperature and salinity conditions and in the presence (PTFE) or absence (Free) of a PTFE membrane: (a) sodium-oxygen, (b) chloride-oxygen, (c) sodium-hydrogen, and (d) chloride-hydrogen.

In Figure 39c, the  $g_{\text{Na-H}}(r)$  showed a peak at  $r=3.05 \text{ \AA}$ , where hydrogen atoms were positioned farther from sodium ions compared to the  $g_{\text{Cl-O}}(r)$  oxygen atoms. This indicated that oxygen atoms were more likely to be found around  $\text{Na}^+$  than hydrogen atoms, with water molecules tending to position their oxygen atoms rather than their hydrogen atoms toward  $\text{Na}^+$ , forming hydrated sodium ions. Figure 39d displays the  $g_{\text{Cl-H}}(r)$  with a first peak at  $r=2.25 \text{ \AA}$ . The  $g_{\text{Cl-H}}(r)$  showing the lowest peak than  $g_{\text{Cl-O}}(r)$ . This trend indicated that chloride ions consistently interacted more strongly with hydrogen atoms in free-

floating droplets at lower temperatures. In comparison, the PTFE surface and higher temperatures weakened these interactions.

The  $g_{O-O}(r)$  displayed a peak at 2.75 Å in Figure 40a, aligning with the oxygen–oxygen RDF of liquid water obtained through X-ray diffraction measurements [98].

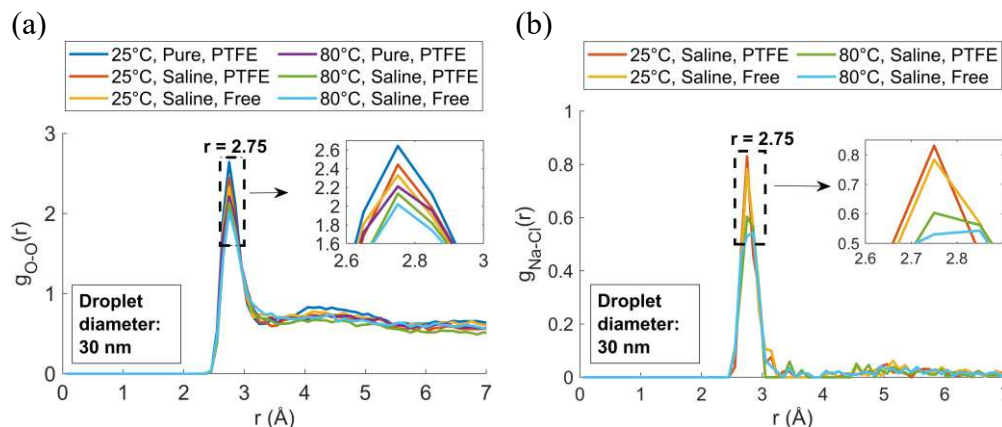


**Figure 40.** Radial distribution functions for atoms under different temperature and salinity conditions and in the presence (PTFE) or absence (Free) of a PTFE membrane: (a) oxygen-oxygen, and (b) chloride-sodium.

At 25°C, the interfacial area for the pure case was found to be higher  $g_{O-O}(r)$  peak at  $r = 2.75$  Å, indicating more substantial water structuring at this temperature. This enhanced structuring caused the droplet to expand to a moderate size, though not as much as at higher temperatures. In the 25°C saline case, the interfacial area was smaller than in the pure case, which was aligned with the reduced  $g_{O-O}(r)$  peak observed for saline droplets at this temperature. The presence of salt disrupted the water structure, reducing the droplet's ability to expand and resulting in a smaller interfacial area and larger contact angle. Observations for both saline and pure cases at 80°C were consistent with this trend. Therefore, a clear relationship was identified between the final interfacial area and the

$g_{O-O}(r)$  structuring: as water structuring weakened (as indicated by a lower  $g_{O-O}(r)$  peak), the droplet spread more, resulting in a larger interfacial area. Salinity further reduced this expansion by disrupting the water network.

In Figure 40b, Na-Cl interactions were shown to be more temperature sensitive, with more evident structure at lower temperatures, which diminished at higher temperatures, especially near the PTFE surface.

In conclusion, the natural structuring of water was significantly disrupted by the presence of salt, primarily through the weakening of its hydrogen bonding network, which limited the droplet's ability to spread over the PTFE surface. This reduction in spreading resulted in a smaller interfacial area and, consequently, a higher contact angle. Although elevated temperatures also contributed to some degree of disruption by promoting expansion and increasing the interfacial area, the effect of salinity on water structuring was more pronounced. Thus, salt-induced disruption played a dominant role in reducing water structuring and increasing the contact angle, with temperature having a secondary but notable impact on the droplet's behavior.

The results presented here suggest that the increase in contact angle with salinity could significantly impact membrane distillation processes, where control over wetting properties is critical for efficiency. Additionally, understanding the salt-induced disruption of water structuring provides valuable insights for designing hydrophobic surfaces in desalination and water treatment applications.

## Chapter 6: Interfacial Dynamics of Water Slabs on Hydrophobic Membrane

### 6.1. Introduction

Next, we used equilibrium MD simulations to investigate the interfaces between pure and saline water on porous and non-porous hydrophobic polytetrafluoroethylene (PTFE) surfaces. To the best of our knowledge, planar interfaces between pure and saline water on realistic hydrophobic surfaces had not been previously explored in atomistic modeling studies. However, the interfaces between water and quartz [99], graphite and silica [100], alumina [101], calcite [102], and graphene [103] have been studied through MD simulations, revealing that the interfacial structural and dynamic properties generally differed from those observed in bulk water. Research on the hydrophobic/water interface was generally focused on detecting low-density regions using X-ray [104] [106] and neutron scattering [105]. X-ray reflectivity [106] was used to investigate the low-density region between water and fluorinated SAMs (self-assembled monolayers) of FAS13 and FAS25. A low-density layer was observed, with widths around 9 Å and gap equivalent widths of approximately 7 Å for FAS25 and 4.5 Å for FAS13. A neutron scattering study [105] identified that the low-density distance for dodecanethiol SAMs was approximately

6.0 Å, while fully deuterated SAMs ranged from 2.1 to 2.7 Å, depending on the temperature. The thickness of the low-density region is debated due to challenges in preparing defect-free monolayers and limited instrument resolution. We initially investigated the equilibration process of pure and saline water slabs on porous and non-porous PTFE surfaces. Subsequently, we identified the density in wetting regions for pure water slabs on both porous and non-porous PTFE surfaces, and the PTFE surface deformations in detail. Finally, ion distributions were thoroughly analyzed for both porous and non-porous cases.

## 6.2. Methods

### 6.2.1. Simulation setting and molecular interactions

MD simulations using LAMMPS were performed to investigate water slab dynamics on a PTFE surface. OVITO [77] and VMD [66] were used for post-processing atomistic data. The simulations employed actual units, a full atom style, periodic boundaries in x and y, and reflective walls in z with a tilted simulation box. Atom interactions were modeled using Lennard-Jones and Coulombic potentials with a 12 Å cutoff and the lj/cut/coul/long pair style. Long-range electrostatics were calculated via the PPPM method [60] with a precision of  $10^{-5}$  and fourth-order accuracy in the k-space interpolation. At the same time, bonded interactions were treated using the harmonic style for bonds and angles [83] and the OPLS style [15] for dihedrals. Interactions between atoms were described in Eq. (A.34).

$$u_{ij}(r) = 4\epsilon_{ij} \left[ \left( \frac{\sigma_{ij}}{r} \right)^{12} - \left( \frac{\sigma_{ij}}{r} \right)^6 \right] + \frac{1}{4\pi\epsilon_0} \frac{q_i q_j}{r} \quad (\text{A.34})$$



where  $r$  indicates the distance between positions  $i$  and  $j$ ,  $q_i$  and  $q_j$  refer to the electric charge at sites  $i$  and  $j$ , respectively. The  $\epsilon_0$  is the vacuum permittivity,  $\epsilon_{ij}$  represents the Lennard-Jones well depth and  $\sigma_{ij}$  is the characteristic diameter. The mixed pair coefficients were generated between atoms of type  $i$  and  $j$  using the arithmetic mixing combination rule:  $\epsilon_{ij} = \sqrt{\epsilon_i \epsilon_j}$ , and  $\sigma_{ij} = (\sigma_i + \sigma_j)/2$ . The system consisted of F (fluorine) and C (carbon) in  $\text{CF}_3$  and  $\text{CF}_2$  groups (PTFE),  $\text{H}_2\text{O}$  (water),  $\text{Na}^+$  (sodium), and  $\text{Cl}^-$  (chloride). Transferable bonded, Lennard-Jones, and charge parameters for PTFE were taken from references [78] [79]. The SPC/E water model [80] was used for bulk water. Packmol [85] placed them and ions with 2.0 Å spacing. The  $\text{Na}^+$  and  $\text{Cl}^-$  parameters were OPLS-derived [81] from GROMACS [42]. Non-bonded parameters are listed in Table 23.

**Table 23.** Lennard-Jones parameters and partial charges for PTFE, water, and ions.

Pair Coeffs	$\sigma(\text{nm})$	$\epsilon$ (kJ/mol)	$q(\text{e})$
F (PTFE)	2.5378	0.0634	-0.11018
$\text{CF}_3$ (PTFE)	2.8062	0.0838	0.33040
$\text{CF}_2$ (PTFE)	2.8812	0.0781	0.22050
O (water)	3.1655	0.1554	-0.84760
H (water)	0.0	0.0	0.42380
$\text{Na}^+$ (ion)	3.3304	0.0027	1
$\text{Cl}^-$ (ion)	4.4172	0.1177	-1

The system was stabilized using the Nosé-Hoover thermostat [82] at 353.15 K, with group-specific control. The velocity-Verlet algorithm with a 2.0 fs time step was used to integrate atomic velocities and positions.

### 6.2.2. Constructing the simulation model

The simulation model assembly is illustrated in Figure 41. The PTFE polymer chain was constructed as  $\text{CF}_3-(\text{C}_2\text{F}_4)_n-\text{CF}_3$ , where 'n' was set to 50, using the force field parameters developed by Orhan Kaya et al. [78] [79]. In this configuration, 'n' represents 50 tetrafluoroethylene ( $\text{C}_2\text{F}_4$ ) units, with trifluoromethyl ( $\text{CF}_3$ ) groups capping both ends, as shown in Figure 41a. The initial chain, generated using Avogadro [27], was duplicated to form 50 identical chains in Figure 41b, and energy minimization was performed to remove atomic overlaps. The structure was then replicated four times along the z-axis, followed by a 5 ns MD simulation in an NPT ensemble at 353.15 K and 101.325 kPa to achieve the experimental density of 2,180 kg/m<sup>3</sup> [65] using LAMMPS in Figure 41c. After reaching the target density, the PTFE assembly was replicated eight times along the x-axis and eleven times along the y-axis in Figure 41d and equilibrated for 1 ns in an NVT ensemble at 353.15 K to prepare for merging with pure and saline water slab lattices. A 24 nm pore was generated at the center and designated porous PTFE. Porous and non-porous PTFE were merged with saline and pure water slabs, creating four configurations as shown in Figure 41 (e) (f) and listed in Table 24. The NaCl mass concentration of the saline water slab ( $C_{\text{NaCl}}$ ) was calculated using Eq. (A.29).

$$C_{\text{NaCl}} = \frac{m_{\text{Na}^+} + m_{\text{Cl}^-}}{m_{\text{water}} + m_{\text{Na}^+} + m_{\text{Cl}^-}} \times 100\% \quad (\text{A.35})$$

where  $C_{\text{NaCl}}$  represents the mass concentration of the solution in percentage.  $m_{\text{Na}^+}$  and  $m_{\text{Cl}^-}$  are the masses of sodium and chloride ions, respectively, and  $m_{\text{water}}$  is the mass of the water in the solution.

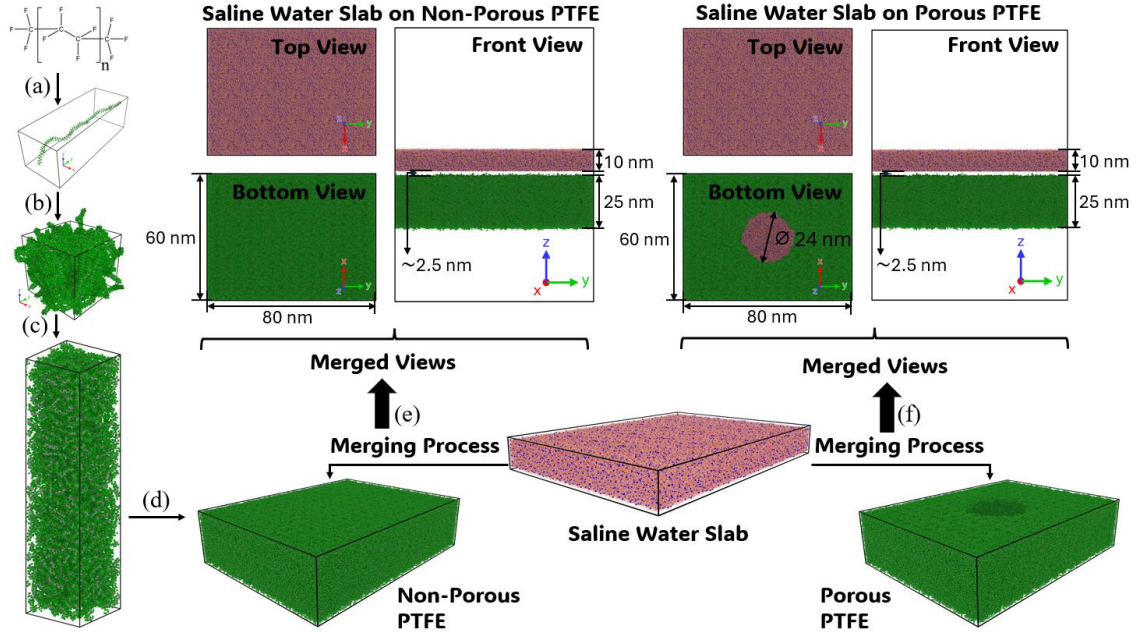


**Figure 41.** The figure shows the assembly of the PTFE polymer and its merging with saline water slabs. In (a), the PTFE chain is constructed as  $\text{CF}_3-(\text{C}_2\text{F}_4)_n-\text{CF}_3$  with 'n' set to 50. In (b) and (c), the chains are duplicated, minimized, and replicated along the z-axis. In (d), the PTFE chains are fully assembled along the x- and y-axes. Panels (e) and (f) depict the merging of saline water slabs with non-porous and porous PTFE, highlighting the 24 nm pore in the porous PTFE.

**Table 24.** Configurations of water and ion count with  $\text{C}_{\text{NaCl}}$  in saline and pure slabs on non-porous and porous PTFE.

Configurations	$N_{\text{water}}$	$N_{\text{Na}^+}$	$N_{\text{Cl}^-}$	$\text{C}_{\text{NaCl}}$
Saline slab on non-porous PTFE	1277150	36425	36425	8.47%
Saline slab on porous PTFE	1277150	36425	36425	8.47%
Pure slab on non-porous PTFE	1350000	0	0	0%
Pure slab on porous PTFE	1350000	0	0	0%

### 6.3. Results and discussion

The simulation results were divided into four phases. First, transient vapor bridges were formed in the gap - a crucial phase for contact. Next, the initial coalescence point was observed when the water slab first touched the PTFE surface, where vapor pressure peaked.

After this, contact nucleation expanded these coalescence points, moving the water slab's center of mass closer to the PTFE. Finally, equilibrium contact was achieved as the vapor bridges allowed full adherence of the water slab to the surface, creating a stable interface and minimizing potential energy for the system. The analyses were performed after the equilibration process was complete. These equilibration processes were illustrated by partial pressure variations Figure 42a and center of mass shifts Figure 42b over time.

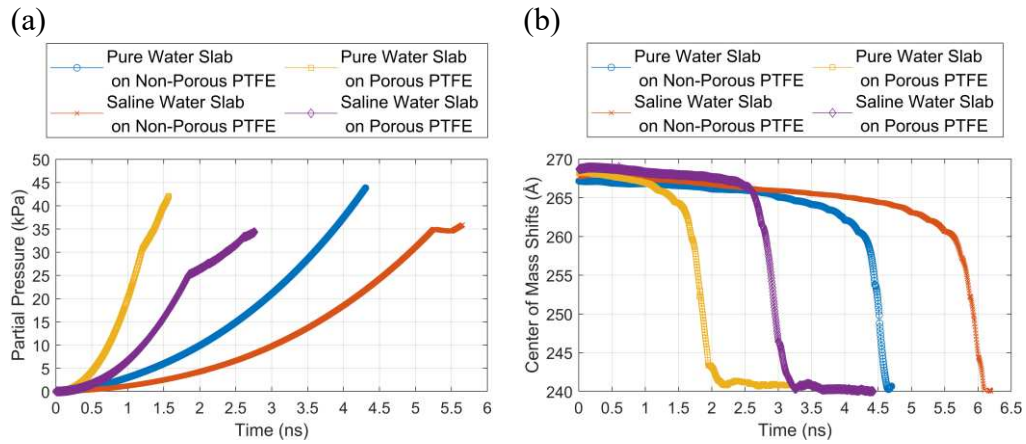


**Figure 42.** Center of mass shifts (a) and partial pressure variations (b) for pure and saline water slabs on porous and non-porous PTFE surfaces over time.

In Figure 42a, variations in partial pressure highlight the role of vapor-phase bridges in the contact process. Partial pressure increased steadily as more bridges formed while the slabs moved closer to the PTFE surface.

The instants where pressure peaked corresponded to the initial coalescence time in Figure 43, indicating that the vapor bridges had collapsed and contact nucleation had begun. After this point, the contact nucleation points were spread across the surface, very quickly drawing the water slab closer to the PTFE surface.

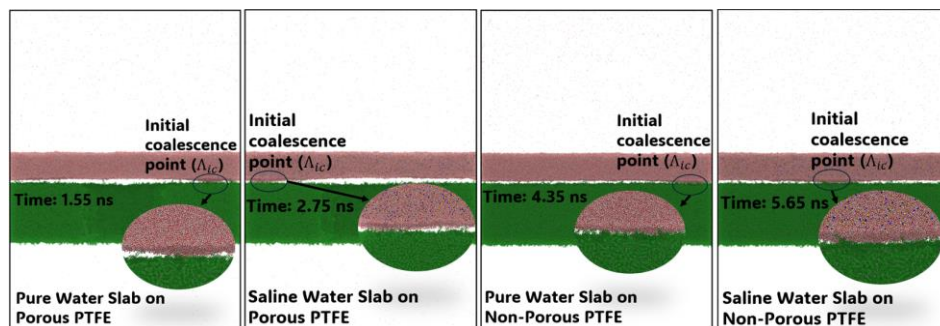


**Figure 43.** Initial coalescence points and time to contact for pure and saline water slabs on porous and non-porous PTFE surfaces

In Figure 42b, center of mass (CoM) shifts show that contact nucleation occurred more quickly on porous PTFE than on non-porous surfaces. The comparison between pure and saline water slabs also revealed that salinity slowed the contact process, likely by altering vapor-phase bridge dynamics and prolonging their persistence, making the interaction between saline water and hydrophobic surfaces more complex.

Density profiles and wetting interfaces for pure water slabs on non-porous and porous PTFE surfaces, as shown in Figure 44, were analyzed after achieving an equilibrated interface. The initial wetting interface and the solid-liquid dividing interface were defined for both cases. The initial wetting interface was identified as where wetting first occurred, while the solid-liquid dividing interface was defined as the location where the PTFE surface roughness ended and the surface became thoroughly wetted. On porous PTFE, the initial wetting position was observed earlier due to water bending around the pores, as seen in the visualization in Figure 44 (a) and (b). Wetting spread uniformly on non-porous PTFE but developed gradually around the pores on the porous surface, leading to broader wetting. This difference in wetting behavior is reflected in comparing the wetting range between the porous and non-porous cases in Figure 44 because the density matching points changed.

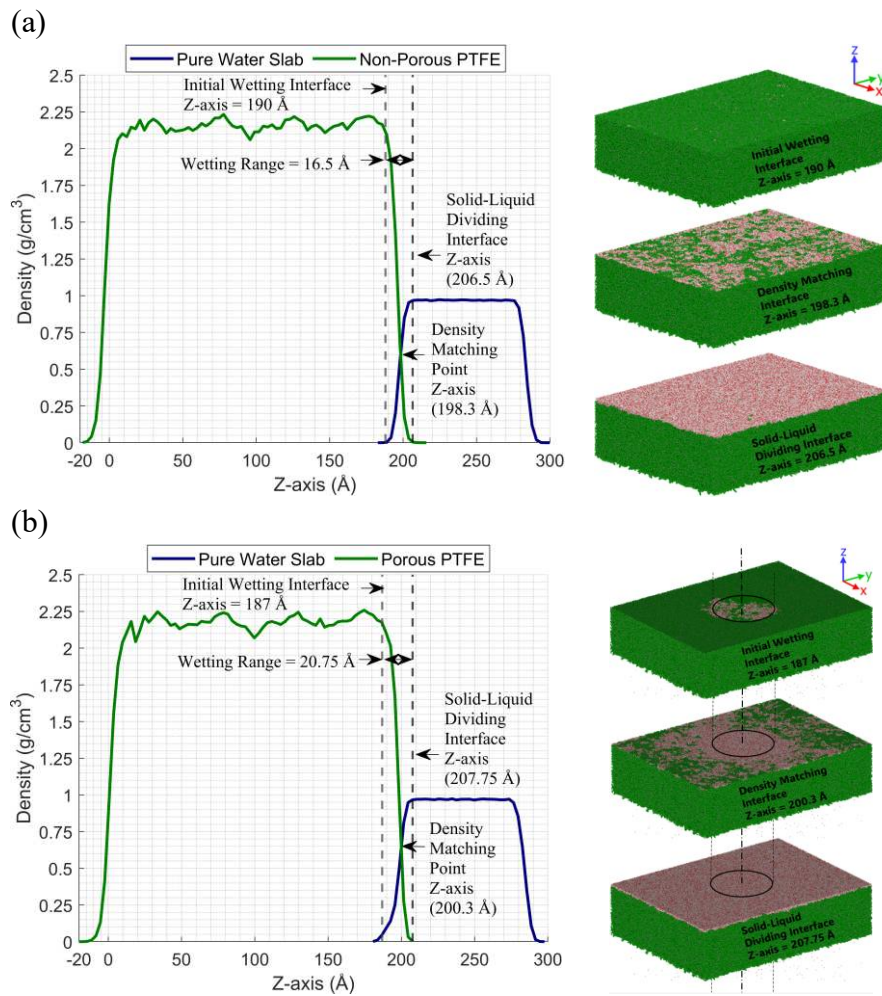


**Figure 44.** Comparison of density profiles and wetting interfaces between pure water slab on non-porous and porous PTFE surfaces.

The resulting change in PTFE's morphological structure is shown schematically in Figure 45a, with the initial and final deformation of the PTFE surface affected by the pure slab in Figure 45b and the saline slab in Figure 45c. OVITO's surface detection algorithm, utilizing an alpha shape method, a generalized version of the convex hull, was used to construct a surface mesh for analyzing and visualizing surface deformation. A triangular surface mesh was generated based on a given probe radius, which was then used for further



analysis, including the visualization of complex rough interfaces. When the initial and final deformations were analyzed, the pore contact and bending angles were observed as two critical structural changes in the PTFE surface.

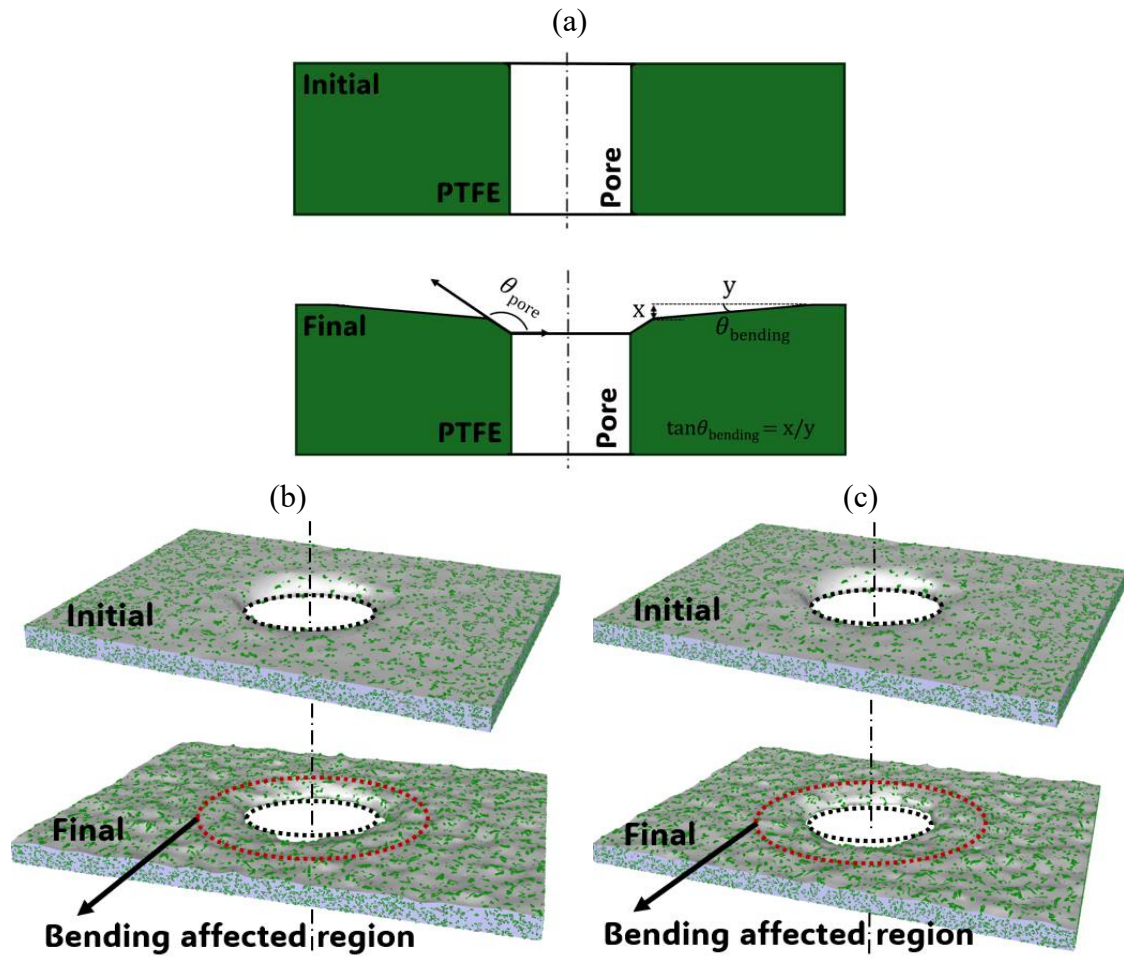


**Figure 45.** (a) Illustration of slab-induced bending and pore contact angles in PTFE before and after deformation. (b) Initial and final deformation of the PTFE surface affected by the pure slab. (c) Initial and final deformation of the PTFE surface affected by the saline slab.

The bending angle ( $\theta_{\text{bending}}$ ) reflected the overall bending or warping of the PTFE surface around the pore due to the applied forces from the slab. The angle was formed by the

curvature or bending of the PTFE surface around the pore region. It was generated due to the slab exerting a force on the PTFE, leading to surface deformation, typically expressed as a slope in the PTFE surface. In Figure 45a,  $\theta_{\text{bending}}$  is shown between the horizontal plane (x-axis) and the sloping surface of the PTFE after deformation. The provided equation ( $\tan(\theta_{\text{bending}}) = x/y$ ) describes the relationship between the horizontal distance (x) over which the surface deformed and the vertical distance (y) of the bending, which allowed the calculation of the bending angle from the trajectory file.  $\theta_{\text{bending}} \sim 8^\circ$  for the PTFE surface affected by the pure slab, and  $\theta_{\text{bending}} \sim 11^\circ$  for the PTFE surface affected by the saline slab. Pore contact angles ( $\theta_{\text{pore}}$ ) reflected the deformation of the pore's sidewalls. The angle was formed between the vertical axis of the pore (typically a line running through the center) and the sloping sidewalls of the pore after deformation. This angle indicated how much the sides of the pore had changed their orientation or 'tilt' due to the influence of the slab on the PTFE structure. Before deformation, the walls of the pore were typically vertical or nearly vertical (indicating little or no tilt). After deformation, the sidewalls were bent inwards or outwards, altering the angle between the vertical axis and the pore sidewalls. The pore contact angles were calculated by establishing a cylindrical coordinate system around the pore. The solid-liquid dividing interface becomes rougher. The cylindrical coordinate system was centered on the pore and extended in radial (r) and vertical (z) directions. The last interface point of the curvature of the water/vapor interface was used to define the edge of the water slab. The contact angle was determined by fitting a curve to the water/vapor interface near the pore and measuring the angle between the tangent at the pore edge and the solid-liquid interface.



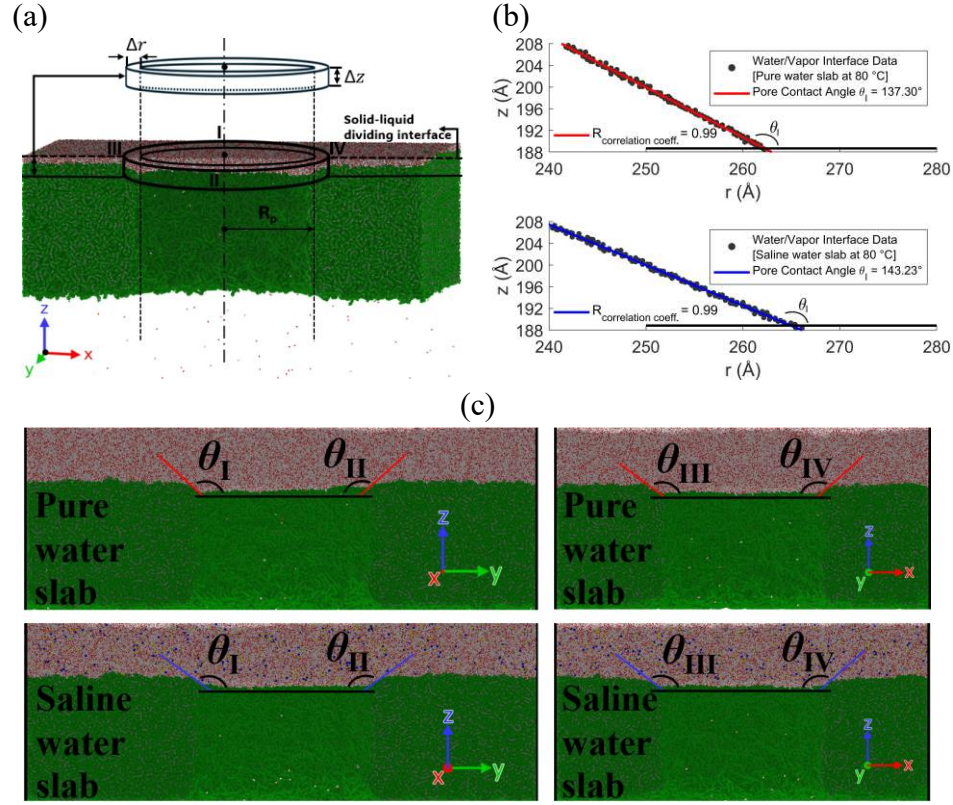


**Figure 46.** Calculation method for pore contact angles: (a) Establishment of the cylindrical coordinate system. (b) Water/vapor interface data and pore contact angle determination for pure and saline water slabs. (c) Comparison of contact angles ( $\theta$ ) at different pore regions for pure and saline water slabs.

Four different contact angles were measured in Table 25 for each slab at distinct points illustrated in Figure 46a around the pore, labeled  $\theta_I^\circ$ ,  $\theta_{II}^\circ$ ,  $\theta_{III}^\circ$ , and  $\theta_{IV}^\circ$  in Figure 46c. By averaging these angles, the contact angle for the pure water slab was calculated as  $\theta_{\text{pure}} = 139.94$  and for the saline water slab as  $\theta_{\text{saline}} = 142.86$ . The contact angle measurements revealed distinct differences between water slabs and droplets on PTFE surfaces emphasizing the effects of interface structure. Droplets exhibited lower contact angles, ranging from  $121^\circ$  for pure water to approximately  $130^\circ$  for saline water at  $80^\circ\text{C}$ , due to limited surface contact from their interfaces. In contrast, slabs showed higher contact

angles—139.94° for pure water and 142.86° for saline water—attributable to their broader, flatter contact regions that amplify the PTFE’s hydrophobicity. This difference underscores that slab configurations lead to a greater apparent hydrophobicity than droplets, resulting from the increased contact area.

**Table 25.** The averaged pore contact angle measurements for pure and saline water slabs.

Case	T ( °C )	$\theta_I^\circ$	$\theta_{II}^\circ$	$\theta_{III}^\circ$	$\theta_{IV}^\circ$	angle°
Pure water slab	80	137.30	139.08	144.58	138.79	139.94
Saline water slab	80	143.23	144.78	142.76	140.65	142.86

As a final analysis in this chapter, the ion concentration profiles of NaCl in saline water slabs on porous and non-porous PTFE surfaces were calculated. The simulation results in Figures 47a and 47b allowed distinct spatial regions to be examined: the Pore-Center and Pore-Away zones on the porous PTFE surface and the Surface-Wide distribution on the non-porous PTFE surface. The NaCl concentration profiles along the z-axis, shown in Figure 47c, revealed critical differences in ion behavior between the two surfaces. On the non-porous PTFE surface, the ion distribution remained relatively homogeneous, characterized by a gradual and smooth increase in NaCl concentration as the distance from the surface decreased. In contrast, the porous PTFE surface exhibited a more complex interaction. The NaCl concentration rose sharply and significantly at the Pore-Center, indicating considerable ion accumulation directly above the pore. The steep gradient observed in this region suggested that the pore acted as a focal point for ion adsorption, creating a localized zone of elevated salinity. This enhanced accumulation was maintained over a considerable range along the z-axis before tapering off, implying that the pore

strongly influenced ion behavior in the interfacial region. The Pore-Away region, though not directly above a pore, also displayed a modulated ion concentration profile. While the concentration increase was less steep than at the Pore-Center, a delayed and more gradual rise was observed, indicating that the pore influenced ion distribution even in regions not directly interacting with it. These findings suggest that surface porosity had a broader impact on ion behavior, extending its influence beyond the immediate vicinity of the pores.

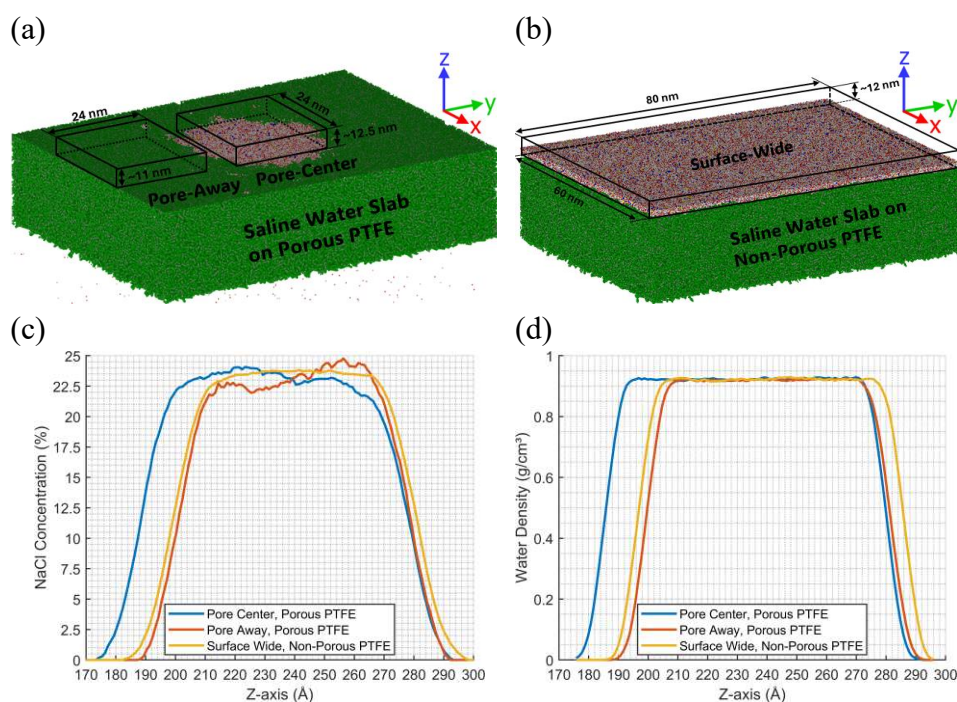


**Figure 47.** NaCl concentration and water density distribution in saline water slabs on porous and non-porous PTFE: (a) Pore-center and pore-away regions on porous PTFE. (b) Surface-wide sampling on non-porous PTFE. (c) NaCl concentration profiles along the Z-axis. (d) Water density profiles along the Z-axis.

Concentration polarization was demonstrated in the simulation results, particularly at the Pore-Center of the Porous PTFE surface and, to a lesser extent, at the Pore-Away region.

In contrast, the Non-Porous PTFE surface exhibited a more uniform ion distribution with less pronounced polarization. Ion accumulation near the surface was enhanced by pores, consistent with concentration polarization caused by restricted ion diffusion from the interfacial region.

In conclusion, this chapter presented several novel insights into the interfacial dynamics of water on hydrophobic PTFE surfaces, exploring complex interactions that have been underrepresented in molecular dynamics literature. First, transient water vapor bridges were observed as intermediate structures, providing a pathway that reduces the energy barrier for contact. Tracked through the center of mass shifts, these bridges significantly stabilized the system during equilibration. They introduced a unique stabilizing mechanism not previously documented in MD simulations. Additionally, partial pressure within the interfacial gap was tracked. Peaks in partial pressure served as markers for coalescence timing, opening avenues to further investigate thermodynamic and energetic elements of nucleation at hydrophobic interfaces.

Furthermore, a detailed examination of the wetting interfaces on porous and non-porous PTFE revealed how surface morphology influences interfacial water density and the distribution of wetting ranges. These variations induced structural deformations on the hydrophobic surfaces, such as bending angles and pore-specific contact angles, highlighting how slab configurations produce distinct wetting behaviors compared to droplets. This difference was further emphasized in contact angle measurements: water slabs exhibited significantly higher contact angles than droplets due to the broader and flatter contact region on the hydrophobic PTFE surface. The increased contact angle for

slabs was attributed to enhanced hydrophobic interactions, which were amplified by surface roughness.

Lastly, the chapter introduced a fresh perspective on concentration polarization in porous PTFE systems through a spatial analysis of NaCl distribution. The selective accumulation of ions, particularly in the Pore-Center region, resulted in sharp ion gradients that have not been previously addressed. This effect of microscopic porosity on ion distribution adds to the understanding of interfacial behaviors and extends current knowledge on wettability and ion segregation near hydrophobic interfaces.

## **Chapter 7: Conclusions and Recommendations for Future Research**

### **7.1. Conclusions**

This dissertation was crafted to significantly contribute to understanding interfacial phenomena between water and hydrophobic PTFE surfaces through molecular dynamics (MD) simulations, focusing on the rigorous development of force field parameters tailored explicitly to these interactions. A foundational methodology was provided for investigating complex interfacial systems by establishing reliable parameters.

CHARMM-compliant parameters for TD were developed to address a critical gap in computational modeling, as prior studies had lacked bonded parameters for TD. These parameters were validated against quantum mechanical (QM) data and experimental vibrational spectra, confirming their accuracy and reliability for future studies on TD interactions. This achievement is anticipated to open new avenues for computational research into TD's role in drug discovery, particularly its interactions with biomolecules, and to set a standard for parameterizing other organometallic compounds in MD.

New force field parameters for PTFE were established using the AMBER functional form, representing a pioneering contribution. These parameters enabled comprehensive modeling of PTFE's condensed-phase behaviors and improved predictions for its density,

heat capacity, and structural properties. The parameters were rigorously tested across various molecular weights and conformational states, validating their applicability. This methodological advancement is expected to prove valuable in material science and industry by enabling precise PTFE interaction simulations under varied conditions, which is essential for designing PTFE-based materials in industrial applications.

Contact angle measurements were conducted to confirm the reliability of the PTFE force field parameters for water interfacial studies. Subsequently, the effect of NaCl concentration on the wettability of a hydrophobic PTFE surface was investigated through MD simulations. The atomic mechanisms behind wettability behavior were elucidated by analyzing the contact angle, ion concentration, density distribution at the interface, and RDF. It was demonstrated that temperature and surface interactions significantly affected the structural properties of water and NaCl solutions, impacting the wettability and interfacial characteristics of droplets on PTFE surfaces. As the temperature increased from 25°C to 80°C, the contact angle rose, indicating that higher temperatures weakened the liquid-solid interaction, rendering the PTFE surface more hydrophobic. The reduction in surface tension and disruption of hydrogen bonding with temperature further contributed to this behavior. The presence of NaCl in water was shown to alter wetting behavior, as salt ions disrupted the water structure, reducing spreading and increasing contact angles. NaCl ions tended to accumulate near the droplet surface at higher temperatures, further increasing hydrophobicity. Analysis of RDFs also revealed weaker ion-water interactions near the PTFE surface at elevated temperatures, with disruptions in hydration shells contributing to the observed changes in wettability. These findings provide insights into the behavior of saline water on hydrophobic surfaces.

The simulation of water slabs interacting with PTFE surfaces yielded insights into unique molecular-level phenomena, including vapor bridge formation, bending, pore contact angles, and water structuring near PTFE. Vapor bridges were observed as transient structures facilitating contact and coalescence between water slabs and the PTFE surface, presenting new perspectives on liquid-solid interactions and bridging mechanisms in confined environments. Analyses of pore contact angles and slab-induced bending highlighted how PTFE's surface morphology modulated interfacial water behavior, with salinity influencing these dynamics by extending vapor bridge formation and intensifying localized deformation. These insights are expected to inform the design of advanced hydrophobic membranes and improve performance in filtration and separation processes.

## **7.2. Recommendations for Future Research**

In Chapter 5, the focus was primarily on large droplet sizes when analyzing the effects of salinity and temperature on hydrophobic wettability. However, it is essential to investigate how the size effect interacts with salinity variations for smaller droplet sizes. Future research could extend the findings by incorporating NaCl in different ratios into smaller droplets. Since smaller droplets may exhibit more complex interfacial dynamics, wetting simulations on smooth surfaces are recommended to obtain more accurate and precise results. This approach would minimize the influence of surface roughness and better isolate the size-dependent effects of salinity and temperature on wettability.

In Chapter 6, this dissertation examined the behavior of ions near hydrophobic surfaces, but future research could delve deeper into the mechanisms of ion segregation. Specifically, it would be valuable to investigate the impact of different ion species, ion concentrations,



scaling nucleation at varying salt levels, feed solution temperatures, and flow rates. While the research in Chapter 6 primarily focuses on equilibrium MD simulations, future studies could explore the effects of dynamic flow conditions, mainly how flow-induced forces influence the structuring of water and ions near hydrophobic surfaces. Additionally, future work could investigate how surface morphology influences ion behavior and segregation at the interface. Comparing the effects of highly structured versus relatively smooth surfaces on salt deposition and ion diffusion could provide valuable insights into scaling and fouling mechanisms in filtration systems.

## References

- [1] U. Anand *et al.*, “Cancer chemotherapy and beyond: Current status, drug candidates, associated risks and progress in targeted therapeutics,” *Genes Dis.*, vol. 10, no. 4, pp. 1367–1401, Jul. 2023, doi: 10.1016/j.gendis.2022.02.007.
- [2] R. Serrano *et al.*, “New titanocene derivative with improved stability and binding ability to albumin exhibits high anticancer activity,” *J. Inorg. Biochem.*, vol. 223, p. 111562, Oct. 2021, doi: 10.1016/j.jinorgbio.2021.111562.
- [3] D.-W. Shen, L. M. Pouliot, M. D. Hall, and M. M. Gottesman, “Cisplatin Resistance: A Cellular Self-Defense Mechanism Resulting from Multiple Epigenetic and Genetic Changes,” *Pharmacol. Rev.*, vol. 64, no. 3, pp. 706–721, Jul. 2012, doi: 10.1124/pr.111.005637.
- [4] P. Kupf-Maier, “Complexes of metals other than platinum as antitumour agents,” *Eur. J. Clin. Pharmacol.*, vol. 47, no. 1, Aug. 1994, doi: 10.1007/BF00193472.
- [5] R. M. Roat-Malone, *Bioinorganic Chemistry: A Short Course*, 1st ed. Wiley, 2007. doi: 10.1002/9780470191712.
- [6] M. Cini, T. D. Bradshaw, and S. Woodward, “Using titanium complexes to defeat cancer: the view from the shoulders of titans,” *Chem. Soc. Rev.*, vol. 46, no. 4, pp. 1040–1051, 2017, doi: 10.1039/C6CS00860G.
- [7] O. Okada, K. Oka, S. Kuwajima, and K. Tanabe, “Molecular Dynamics Studies of Amorphous Poly(Tetrafluoroethylene),” *Mol. Simul.*, vol. 21, no. 5–6, pp. 325–342, Jan. 1999, doi: 10.1080/08927029908022072.
- [8] L. A. Curtiss, K. Raghavachari, P. C. Redfern, V. Rassolov, and J. A. Pople, “Gaussian-3 (G3) theory for molecules containing first and second-row atoms,” *J. Chem. Phys.*, vol. 109, no. 18, pp. 7764–7776, Nov. 1998, doi: 10.1063/1.477422.
- [9] T. H. Dunning, “Gaussian basis sets for use in correlated molecular calculations. I. The atoms boron through neon and hydrogen,” *J. Chem. Phys.*, vol. 90, no. 2, pp. 1007–1023, Jan. 1989, doi: 10.1063/1.456153.
- [10] S. S. Jang, M. Blanco, W. A. Goddard, G. Caldwell, and R. B. Ross, “The Source of Helicity in Perfluorinated *N* -Alkanes,” *Macromolecules*, vol. 36, no. 14, pp. 5331–5341, Jul. 2003, doi: 10.1021/ma025645t.

- [11] A. D. Becke, “Density-functional thermochemistry. III. The role of exact exchange,” *J. Chem. Phys.*, vol. 98, no. 7, pp. 5648–5652, Apr. 1993, doi: 10.1063/1.464913.
- [12] C. Lee, W. Yang, and R. G. Parr, “Development of the Colle-Salvetti correlation-energy formula into a functional of the electron density,” *Phys. Rev. B*, vol. 37, no. 2, pp. 785–789, Jan. 1988, doi: 10.1103/PhysRevB.37.785.
- [13] S. Dasgupta, T. Yamasaki, and W. A. Goddard, “The Hessian biased singular value decomposition method for optimization and analysis of force fields,” *J. Chem. Phys.*, vol. 104, no. 8, pp. 2898–2920, Feb. 1996, doi: 10.1063/1.471112.
- [14] R. S. Mulliken, “Electronic Population Analysis on LCAO–MO Molecular Wave Functions. I,” *J. Chem. Phys.*, vol. 23, no. 10, pp. 1833–1840, Oct. 1955, doi: 10.1063/1.1740588.
- [15] E. K. Watkins and W. L. Jorgensen, “Perfluoroalkanes: Conformational Analysis and Liquid-State Properties from ab Initio and Monte Carlo Calculations,” *J. Phys. Chem. A*, vol. 105, no. 16, pp. 4118–4125, Apr. 2001, doi: 10.1021/jp004071w.
- [16] J. Vaara, O. L. Malkina, H. Stoll, V. G. Malkin, and M. Kaupp, “Study of relativistic effects on nuclear shieldings using density-functional theory and spin–orbit pseudopotentials,” *J. Chem. Phys.*, vol. 114, no. 1, pp. 61–71, Jan. 2001, doi: 10.1063/1.1330208.
- [17] O. Borodin, G. D. Smith, and D. Bedrov, “A Quantum Chemistry Based Force Field for Perfluoroalkanes and Poly(tetrafluoroethylene),” *J. Phys. Chem. B*, vol. 106, no. 38, pp. 9912–9922, Sep. 2002, doi: 10.1021/jp026158i.
- [18] Chr. Møller and M. S. Plesset, “Note on an Approximation Treatment for Many-Electron Systems,” *Phys. Rev.*, vol. 46, no. 7, pp. 618–622, Oct. 1934, doi: 10.1103/PhysRev.46.618.
- [19] J. Wang, R. M. Wolf, J. W. Caldwell, P. A. Kollman, and D. A. Case, “Development and testing of a general amber force field,” *J. Comput. Chem.*, vol. 25, no. 9, pp. 1157–1174, Jul. 2004, doi: 10.1002/jcc.20035.
- [20] R. Bhowmik, S. Sihn, V. Varshney, A. K. Roy, and J. P. Vernon, “Calculation of specific heat of polymers using molecular dynamics simulations,” *Polymer*, vol. 167, pp. 176–181, Mar. 2019, doi: 10.1016/j.polymer.2019.02.013.

- [21] J. H. Park and N. R. Aluru, “Temperature-dependent wettability on a titanium dioxide surface,” *Mol. Simul.*, vol. 35, no. 1–2, pp. 31–37, Jan. 2009, doi: 10.1080/08927020802398884.
- [22] C. D. Daub, D. Bratko, and A. Luzar, “Electric Control of Wetting by Salty Nanodrops: Molecular Dynamics Simulations,” *J. Phys. Chem. C*, vol. 115, no. 45, pp. 22393–22399, Nov. 2011, doi: 10.1021/jp206242n.
- [23] J. Zhang, M. K. Borg, K. Sefiane, and J. M. Reese, “Wetting and evaporation of salt-water nanodroplets: A molecular dynamics investigation,” *Phys. Rev. E*, vol. 92, no. 5, p. 052403, Nov. 2015, doi: 10.1103/PhysRevE.92.052403.
- [24] X. Li, C. Zhang, J. Wang, H. Huang, and S. Wang, “Atomic-level insights into nano-salt droplets wetting on the MgO surface using molecular dynamics simulations,” *Corros. Sci.*, vol. 167, p. 108549, May 2020, doi: 10.1016/j.corsci.2020.108549.
- [25] J. A. Nelder and R. Mead, “A Simplex Method for Function Minimization,” *Comput. J.*, vol. 7, no. 4, pp. 308–313, Jan. 1965, doi: 10.1093/comjnl/7.4.308.
- [26] B. R. Brooks *et al.*, “CHARMM: The biomolecular simulation program,” *J. Comput. Chem.*, vol. 30, no. 10, pp. 1545–1614, Jul. 2009, doi: 10.1002/jcc.21287.
- [27] M. D. Hanwell, D. E. Curtis, D. C. Lonie, T. Vandermeersch, E. Zurek, and G. R. Hutchison, “Avogadro: an advanced semantic chemical editor, visualization, and analysis platform,” *J. Cheminformatics*, vol. 4, no. 1, p. 17, Dec. 2012, doi: 10.1186/1758-2946-4-17.
- [28] J. Ghosh, S. Marru, N. Singh, K. Vanomesslaeghe, Y. Fan, and S. Pamidighantam, “Molecular parameter optimization gateway (ParamChem): workflow management through TeraGrid ASTA,” in *Proceedings of the 2011 TeraGrid Conference: Extreme Digital Discovery*, Salt Lake City Utah: ACM, Jul. 2011, pp. 1–8. doi: 10.1145/2016741.2016779.
- [29] K. Vanommeslaeghe and A. D. MacKerell, “Automation of the CHARMM General Force Field (CGenFF) I: Bond Perception and Atom Typing,” *J. Chem. Inf. Model.*, vol. 52, no. 12, pp. 3144–3154, Dec. 2012, doi: 10.1021/ci300363c.
- [30] S. Cross, M. M. Kuttel, J. E. Stone, and J. E. Gain, “Visualisation of cyclic and multi-branched molecules with VMD,” *J. Mol. Graph. Model.*, vol. 28, no. 2, pp. 131–139, Sep. 2009, doi: 10.1016/j.jmgm.2009.04.010.

- [31] K. Vanommeslaeghe, E. P. Raman, and A. D. MacKerell, "Automation of the CHARMM General Force Field (CGenFF) II: Assignment of Bonded Parameters and Partial Atomic Charges," *J. Chem. Inf. Model.*, vol. 52, no. 12, pp. 3155–3168, Dec. 2012, doi: 10.1021/ci3003649.
- [32] M. J. Frisch, G. W. Trucks, and H. B. Schlegel, *Gaussian 16, Revision C.01*. (2016). Gaussian, Inc., Wallingford CT.
- [33] J. C. Phillips *et al.*, "Scalable molecular dynamics with NAMD," *J. Comput. Chem.*, vol. 26, no. 16, pp. 1781–1802, Dec. 2005, doi: 10.1002/jcc.20289.
- [34] T. H. Dunning, "Gaussian basis sets for use in correlated molecular calculations. I. The atoms boron through neon and hydrogen," *J. Chem. Phys.*, vol. 90, no. 2, pp. 1007–1023, Jan. 1989, doi: 10.1063/1.456153.
- [35] A. V. Mitin, J. Baker, and P. Pulay, "An improved 6-31G\* basis set for first-row transition metals," *J. Chem. Phys.*, vol. 118, no. 17, pp. 7775–7782, May 2003, doi: 10.1063/1.1563619.
- [36] W. L. Jorgensen, J. Chandrasekhar, J. D. Madura, R. W. Impey, and M. L. Klein, "Comparison of simple potential functions for simulating liquid water," *J. Chem. Phys.*, vol. 79, no. 2, pp. 926–935, Jul. 1983, doi: 10.1063/1.445869.
- [37] C. G. Mayne, J. Saam, K. Schulten, E. Tajkhorshid, and J. C. Gumbart, "Rapid parameterization of small molecules using the force field toolkit," *J. Comput. Chem.*, vol. 34, no. 32, pp. 2757–2770, Dec. 2013, doi: 10.1002/jcc.23422.
- [38] O. Guvench and A. D. MacKerell, "Automated conformational energy fitting for force-field development," *J. Mol. Model.*, vol. 14, no. 8, pp. 667–679, Aug. 2008, doi: 10.1007/s00894-008-0305-0.
- [39] T. N. Doman, C. R. Landis, and B. Bosnich, "Molecular mechanics force fields for linear metallocenes," *J. Am. Chem. Soc.*, vol. 114, no. 18, pp. 7264–7272, Aug. 1992, doi: 10.1021/ja00044a042.
- [40] D. Kleinhesselink and M. Wolfsberg, "The evaluation of power spectra in molecular dynamics simulations of anharmonic solids and surfaces," *Surf. Sci.*, vol. 262, no. 1–2, pp. 189–207, Feb. 1992, doi: 10.1016/0039-6028(92)90471-H.
- [41] V. Agarwal, G. W. Huber, W. C. Conner, and S. M. Auerbach, "Simulating infrared spectra and hydrogen bonding in cellulose I $\beta$  at elevated temperatures," *J. Chem. Phys.*, vol. 135, no. 13, p. 134506, Oct. 2011, doi: 10.1063/1.3646306.

- [42] M. J. Abraham *et al.*, “GROMACS: High performance molecular simulations through multi-level parallelism from laptops to supercomputers,” *SoftwareX*, vol. 1–2, pp. 19–25, Sep. 2015, doi: 10.1016/j.softx.2015.06.001.
- [43] T. Darden, D. York, and L. Pedersen, “Particle mesh Ewald: An  $N \cdot \log(N)$  method for Ewald sums in large systems,” *J. Chem. Phys.*, vol. 98, no. 12, pp. 10089–10092, Jun. 1993, doi: 10.1063/1.464397.
- [44] S. Nosé, “A molecular dynamics method for simulations in the canonical ensemble,” *Mol. Phys.*, vol. 52, no. 2, pp. 255–268, Jun. 1984, doi: 10.1080/00268978400101201.
- [45] M. Parrinello and A. Rahman, “Polymorphic transitions in single crystals: A new molecular dynamics method,” *J. Appl. Phys.*, vol. 52, no. 12, pp. 7182–7190, Dec. 1981, doi: 10.1063/1.328693.
- [46] “National Institute of Advanced Industrial Science and Technology.” [Online]. Available: <http://sdb.sdb.aist.go.jp>
- [47] E. Diana, Rossetti, P. L. Stanghellini, and S. F. A. Kettle, “Vibrational Study of (n5-Cyclopentadienyl)metal Complexes,” *Inorg. Chem.*, vol. 36, no. 3, p. 382, 1997, doi: <https://doi.org/10.1021/ic960545n>.
- [48] A. Clearfield, W. David Keith, C. H. Molina-Salazar, R. Ropal, and I. Bernal, “Structural Studies of  $(\pi\text{-C}_5\text{H}_5)_2\text{MX}_2$  Complexes and their Derivatives. The Structure of Bis( $\pi$ -cyclopentadienyl)titanium Dichloride,” *Can. J. Chem.*, 1975, doi: <https://doi.org/10.1139/v75-228>.
- [49] “Normal-Mode Analysis.” [Online]. Available: <https://manual.gromacs.org/current/reference-manual/algorithms/normal-mode-analysis.html>
- [50] M. D. Hanwell, D. E. Curtis, D. C. Lonie, T. Vandermeersch, E. Zurek, and G. R. Hutchison, *SOFTWARE Open Access Avogadro*. (2012).
- [51] P. E. Hansen, B. A. Saeed, R. S. Rutu, and T. Kupka, “One-bond  $^1J(^{15}\text{N},\text{H})$  coupling constants at  $\text{sp}^2$ -hybridized nitrogen of Schiff bases, enaminones and similar compounds: A theoretical study,” *Magn. Reson. Chem.*, vol. 58, no. 8, pp. 750–762, Aug. 2020, doi: 10.1002/mrc.5052.

- [52] A. Malloum, J. J. Fifen, and J. Conradie, “Solvation energies of the proton in methanol revisited and temperature effects,” *Phys. Chem. Chem. Phys.*, vol. 20, no. 46, pp. 29184–29206, 2018, doi: 10.1039/C8CP05823G.
- [53] D. A. Case *et al.*, “AmberTools,” *J. Chem. Inf. Model.*, vol. 63, no. 20, pp. 6183–6191, Oct. 2023, doi: 10.1021/acs.jcim.3c01153.
- [54] C. W. Hopkins and A. E. Roitberg, “Fitting of Dihedral Terms in Classical Force Fields as an Analytic Linear Least-Squares Problem,” *J. Chem. Inf. Model.*, vol. 54, no. 7, pp. 1978–1986, Jul. 2014, doi: 10.1021/ci500112w.
- [55] “PubChem Compound Summary for CID 9638, Perflubutane.” 2024. [Online]. Available: <https://pubchem.ncbi.nlm.nih.gov/compound/Perflubutane>
- [56] J. A. Brown and W. H. Mears, “Physical Properties of n-Perfluorobutane,” *J. Phys. Chem.*, vol. 62, no. 8, pp. 960–962, Aug. 1958, doi: 10.1021/j150566a015.
- [57] R. Faller, H. Schmitz, O. Biermann, and F. Muller-Plathe, “Automatic parameterization of force fields for liquids by simplex optimization,” *J. Comput. Chem.*, vol. 20, no. 10, pp. 1009–1017, Jul. 1999, doi: 10.1002/(SICI)1096-987X(19990730)20:10<1009::AID-JCC3>3.0.CO;2-C.
- [58] R. R. Barton and J. S. Ivey, “Modifications of the Nelder-Mead simplex method for stochastic simulation response optimization,” in *1991 Winter Simulation Conference Proceedings.*, Phoenix, AZ, USA: IEEE, 1991, pp. 945–953. doi: 10.1109/WSC.1991.185709.
- [59] C. Tantardini and A. R. Oganov, “Thermochemical electronegativities of the elements,” *Nat. Commun.*, vol. 12, no. 1, p. 2087, Apr. 2021, doi: 10.1038/s41467-021-22429-0.
- [60] T. Darden, D. York, and L. Pedersen, “Particle mesh Ewald: An  $N \cdot \log(N)$  method for Ewald sums in large systems,” *J. Chem. Phys.*, vol. 98, no. 12, pp. 10089–10092, Jun. 1993, doi: 10.1063/1.464397.
- [61] W. G. Hoover, “Canonical dynamics: Equilibrium phase-space distributions,” *Phys. Rev. A*, vol. 31, no. 3, pp. 1695–1697, Mar. 1985, doi: 10.1103/PhysRevA.31.1695.
- [62] S. Smidstrup *et al.*, “QuantumATK: an integrated platform of electronic and atomic-scale modelling tools,” *J. Phys. Condens. Matter*, vol. 32, no. 1, p. 015901, Jan. 2020, doi: 10.1088/1361-648X/ab4007.

- [63] J. Schneider *et al.*, “ATK-ForceField: a new generation molecular dynamics software package,” *Model. Simul. Mater. Sci. Eng.*, vol. 25, no. 8, p. 085007, Dec. 2017, doi: 10.1088/1361-651X/aa8ff0.
- [64] A. W. Sousa Da Silva and W. F. Vranken, “ACPYPE - AnteChamber PYthon Parser interfacE,” *BMC Res. Notes*, vol. 5, no. 1, p. 367, Dec. 2012, doi: 10.1186/1756-0500-5-367.
- [65] L. C. S. Nunes, F. W. R. Dias, and H. S. Da Costa Mattos, “Mechanical behavior of polytetrafluoroethylene in tensile loading under different strain rates,” *Polym. Test.*, vol. 30, no. 7, pp. 791–796, Oct. 2011, doi: 10.1016/j.polymertesting.2011.07.004.
- [66] W. Humphrey, A. Dalke, and K. Schulten, “VMD: Visual molecular dynamics,” *J. Mol. Graph.*, vol. 14, no. 1, pp. 33–38, Feb. 1996, doi: 10.1016/0263-7855(96)00018-5.
- [67] G. Xu, “X-Ray Scattering Study of New Perfluorinated Ionomers,” *Polym J*, vol. 25, no. 4, 1993.
- [68] W. Langel, “Introduction to neutron scattering,” *ChemTexts*, vol. 9, no. 4, p. 12, Oct. 2023, doi: 10.1007/s40828-023-00184-7.
- [69] Y. Onodera, T. Sato, and S. Kohara, “X-Ray and Neutron Pair Distribution Function Analysis,” in *Hyperordered Structures in Materials*, K. Hayashi, Ed., in The Materials Research Society Series. , Singapore: Springer Nature Singapore, 2024, pp. 93–120. doi: 10.1007/978-981-99-5235-9\_4.
- [70] R. Wang, G. Xu, and Y. He, “Structure and properties of polytetrafluoroethylene (PTFE) fibers,” *E-Polym.*, vol. 17, no. 3, pp. 215–220, May 2017, doi: 10.1515/epoly-2016-0059.
- [71] C. Quarti, A. Milani, and C. Castiglioni, “Ab Initio Calculation of the IR Spectrum of PTFE: Helical Symmetry and Defects,” *J. Phys. Chem. B*, vol. 117, no. 2, pp. 706–718, Jan. 2013, doi: 10.1021/jp3102145.
- [72] H. W. Starkweather, R. C. Ferguson, D. B. Chase, and J. M. Minor, “Infrared spectra of amorphous and crystalline poly(tetrafluoroethylene),” *Macromolecules*, vol. 18, no. 9, pp. 1684–1686, Sep. 1985, doi: 10.1021/ma00151a007.
- [73] J. Horbach, W. Kob, and K. Binder, “Specific Heat of Amorphous Silica within the Harmonic Approximation,” *J. Phys. Chem. B*, vol. 103, no. 20, pp. 4104–4108, May 1999, doi: 10.1021/jp983898b.



- [74] S.-T. Lin, M. Blanco, and W. A. Goddard, “The two-phase model for calculating thermodynamic properties of liquids from molecular dynamics: Validation for the phase diagram of Lennard-Jones fluids,” *J. Chem. Phys.*, vol. 119, no. 22, pp. 11792–11805, Dec. 2003, doi: 10.1063/1.1624057.
- [75] G. T. Furukawa, R. E. Mccoskey, and G. J. King, “Calorimetric properties of polytetrafluoroethylene (teflon) from 0-degrees to 365-degrees-K,” *J. Res. Natl. Bur. Stand.*, vol. 49, no. 4, p. 273, Oct. 1952, doi: 10.6028/jres.049.029.
- [76] S. Plimpton, “Fast Parallel Algorithms for Short-Range Molecular Dynamics,” *J. Comput. Phys.*, vol. 117, no. 1, pp. 1–19, Mar. 1995, doi: 10.1006/jcph.1995.1039.
- [77] A. Stukowski, “Visualization and analysis of atomistic simulation data with OVITO—the Open Visualization Tool,” *Model. Simul. Mater. Sci. Eng.*, vol. 18, no. 1, p. 015012, Jan. 2010, doi: 10.1088/0965-0393/18/1/015012.
- [78] O. Kaya, A. Oztekin, and E. B. Webb, “Development of AMBER-compliant transferable force field parameters for polytetrafluoroethylene,” *Open Chem.*, vol. 22, no. 1, p. 20240072, Aug. 2024, doi: 10.1515/chem-2024-0072.
- [79] O. Kaya, “Data from ‘Development of an AMBER-Compliant Transferable Force Field Parameters for Polytetrafluoroethylene.’” figshare, p. 322406 Bytes, 2024. doi: 10.6084/M9.FIGSHARE.26197325.V1.
- [80] H. J. C. Berendsen, J. R. Grigera, and T. P. Straatsma, “The missing term in effective pair potentials,” *J. Phys. Chem.*, vol. 91, no. 24, pp. 6269–6271, Nov. 1987, doi: 10.1021/j100308a038.
- [81] W. L. Jorgensen, D. S. Maxwell, and J. Tirado-Rives, “Development and Testing of the OPLS All-Atom Force Field on Conformational Energetics and Properties of Organic Liquids,” *J. Am. Chem. Soc.*, vol. 118, no. 45, pp. 11225–11236, Nov. 1996, doi: 10.1021/ja9621760.
- [82] S. Nosé, “A molecular dynamics method for simulations in the canonical ensemble,” *Mol. Phys.*, vol. 52, no. 2, pp. 255–268, Jun. 1984, doi: 10.1080/00268978400101201.
- [83] H. C. Andersen, “Rattle: A ‘velocity’ version of the shake algorithm for molecular dynamics calculations,” *J. Comput. Phys.*, vol. 52, no. 1, pp. 24–34, Oct. 1983, doi: 10.1016/0021-9991(83)90014-1.

- [84] N. Giovambattista, A. B. Almeida, A. M. Alencar, and S. V. Buldyrev, “Validation of Capillarity Theory at the Nanometer Scale by Atomistic Computer Simulations of Water Droplets and Bridges in Contact with Hydrophobic and Hydrophilic Surfaces,” *J. Phys. Chem. C*, vol. 120, no. 3, pp. 1597–1608, Jan. 2016, doi: 10.1021/acs.jpcc.5b10377.
- [85] L. Martínez, R. Andrade, E. G. Birgin, and J. M. Martínez, “P ACKMOL : A package for building initial configurations for molecular dynamics simulations,” *J. Comput. Chem.*, vol. 30, no. 13, pp. 2157–2164, Oct. 2009, doi: 10.1002/jcc.21224.
- [86] T. D. Blake and J. M. Haynes, “Kinetics of displacement,” *J. Colloid Interface Sci.*, vol. 30, no. 3, pp. 421–423, Jul. 1969, doi: 10.1016/0021-9797(69)90411-1.
- [87] E. B. Webb, G. S. Grest, and D. R. Heine, “Precursor Film Controlled Wetting of Pb on Cu,” *Phys. Rev. Lett.*, vol. 91, no. 23, p. 236102, Dec. 2003, doi: 10.1103/PhysRevLett.91.236102.
- [88] R. Sedev, “The molecular-kinetic approach to wetting dynamics: Achievements and limitations,” *Adv. Colloid Interface Sci.*, vol. 222, pp. 661–669, Aug. 2015, doi: 10.1016/j.cis.2014.09.008.
- [89] J. Hautman and M. L. Klein, “Microscopic wetting phenomena,” *PHYSICAL Rev. Lett.*, vol. 67, no. 13, 1991.
- [90] Y. Xiang, P. Fulmek, D. Platz, and U. Schmid, “Temperature Dependence of Water Contact Angle on Teflon AF1600,” *Langmuir*, vol. 38, no. 4, pp. 1631–1637, Feb. 2022, doi: 10.1021/acs.langmuir.1c03202.
- [91] C. F. Fan and T. Çağın, “Wetting of crystalline polymer surfaces: A molecular dynamics simulation,” *J. Chem. Phys.*, vol. 103, no. 20, pp. 9053–9061, Nov. 1995, doi: 10.1063/1.470016.
- [92] M. J. De Ruijter, T. D. Blake, and J. De Coninck, “Dynamic Wetting Studied by Molecular Modeling Simulations of Droplet Spreading,” *Langmuir*, vol. 15, no. 22, pp. 7836–7847, Oct. 1999, doi: 10.1021/la990171l.
- [93] E. Santiso, C. Herdes, and E. Müller, “On the Calculation of Solid-Fluid Contact Angles from Molecular Dynamics,” *Entropy*, vol. 15, no. 9, pp. 3734–3745, Sep. 2013, doi: 10.3390/e15093734.

- [94] M. J. Hancock, K. Sekeroglu, and M. C. Demirel, “Bioinspired Directional Surfaces for Adhesion, Wetting, and Transport,” *Adv. Funct. Mater.*, vol. 22, no. 11, pp. 2223–2234, Jun. 2012, doi: 10.1002/adfm.201103017.
- [95] M. Khalkhali, N. Kazemi, H. Zhang, and Q. Liu, “Wetting at the nanoscale: A molecular dynamics study,” *J. Chem. Phys.*, vol. 146, no. 11, p. 114704, Mar. 2017, doi: 10.1063/1.4978497.
- [96] M. Galib *et al.*, “Revisiting the hydration structure of aqueous Na<sup>+</sup>,” *J. Chem. Phys.*, vol. 146, no. 8, p. 084504, Feb. 2017, doi: 10.1063/1.4975608.
- [97] R. Mancinelli, A. Botti, F. Bruni, M. A. Ricci, and A. K. Soper, “Hydration of Sodium, Potassium, and Chloride Ions in Solution and the Concept of Structure Maker/Breaker,” *J. Phys. Chem. B*, vol. 111, no. 48, pp. 13570–13577, Dec. 2007, doi: 10.1021/jp075913v.
- [98] L. B. Skinner, C. Huang, D. Schlesinger, L. G. M. Pettersson, A. Nilsson, and C. J. Benmore, “Benchmark oxygen-oxygen pair-distribution function of ambient water from x-ray diffraction measurements with a wide  $Q$  -range,” *J. Chem. Phys.*, vol. 138, no. 7, p. 074506, Feb. 2013, doi: 10.1063/1.4790861.
- [99] M. L. Schlegel, K. L. Nagy, P. Fenter, and N. C. Sturchio, “Structures of quartz (100)- and (101)-water interfaces determined by x-ray reflectivity and atomic force microscopy of natural growth surfaces,” *Geochim. Cosmochim. Acta*, vol. 66, no. 17, pp. 3037–3054, Sep. 2002, doi: 10.1016/S0016-7037(02)00912-2.
- [100] D. Argyris, N. R. Tummala, A. Striolo, and D. R. Cole, “Molecular Structure and Dynamics in Thin Water Films at the Silica and Graphite Surfaces,” *J. Phys. Chem. C*, vol. 112, no. 35, pp. 13587–13599, Sep. 2008, doi: 10.1021/jp803234a.
- [101] D. Argyris, T. Ho, D. R. Cole, and A. Striolo, “Molecular Dynamics Studies of Interfacial Water at the Alumina Surface,” *J. Phys. Chem. C*, vol. 115, no. 5, pp. 2038–2046, Feb. 2011, doi: 10.1021/jp109244c.
- [102] A. Ali, T. T. B. Le, A. Striolo, and D. R. Cole, “Salt Effects on the Structure and Dynamics of Interfacial Water on Calcite Probed by Equilibrium Molecular Dynamics Simulations,” *J. Phys. Chem. C*, vol. 124, no. 45, pp. 24822–24836, Nov. 2020, doi: 10.1021/acs.jpcc.0c07621.
- [103] R. Garcia, “Interfacial Liquid Water on Graphite, Graphene, and 2D Materials,” *ACS Nano*, vol. 17, no. 1, pp. 51–69, Jan. 2023, doi: 10.1021/acsnano.2c10215.

- [104] A. Uysal *et al.*, “What x rays can tell us about the interfacial profile of water near hydrophobic surfaces,” *Phys. Rev. B*, vol. 88, no. 3, p. 035431, Jul. 2013, doi: 10.1103/PhysRevB.88.035431.
- [105] S. Chattopadhyay *et al.*, “How Water Meets a Very Hydrophobic Surface,” *Phys. Rev. Lett.*, vol. 105, no. 3, p. 037803, Jul. 2010, doi: 10.1103/PhysRevLett.105.037803.
- [106] M. Maccarini *et al.*, “Density Depletion at Solid–Liquid Interfaces: a Neutron Reflectivity Study,” *Langmuir*, vol. 23, no. 2, pp. 598–608, Jan. 2007, doi: 10.1021/la061943y.

## Vitae

Name: Orhan Kaya

Date of Birth: June 4<sup>th</sup>, 1988

Birthplace: Istanbul, Türkiye

---

## Education History

- Bachelor of Science (BSc) in Mechanical Engineering  
İnönü University (2007–2012)
- Bachelor of Science (BSc) in Mechanical Engineering  
Yıldız Technical University (2010–2011)  
*(FARABI Scholarship & Exchange Program)*
- Master of Science (MSc) in Computational Science and Engineering  
Istanbul Technical University (2015–2016)  
*(Left after being accepted to Lehigh University, no degree awarded)*
- Master of Science (MSc) in Mechanical Engineering & Mechanics  
Lehigh University (2017–2019)
- Doctor of Philosophy (PhD) in Mechanical Engineering & Mechanics  
Lehigh University (2019–2025)

## **Professional Experience**

### **HVAC and Pipeline Engineer**

*Çetin Mühendislik Ltd. Company, Istanbul, Türkiye (2012–2013)*

- Designed air heating, water heating, ventilation, and air conditioning systems for various building types, overseeing their implementation throughout the construction process. Developed different gas units for IGDAS (Istanbul Gas Distribution Industry). Utilized design and analysis programs such as REVIT-MEP, AutoCAD, and GASLINE 3D.

### **Field Service Engineer**

*Gendarmerie Maintenance Command, Ağrı, Türkiye (2012–2013)*

- Served as a control engineer in the Maintenance Command, responsible for the repair, overhaul, and maintenance of military vehicles, including Otokar Akrep, Otokar Cobra, Dragoon 300, Cadillac V150/S, and Shortland S55. (In Türkiye, military service is compulsory for all male citizens, and it is typically considered a part of one's professional experience.)

### **Foreign Trade Specialist**

*PETES Machinery Industry, Istanbul, Türkiye (2014–2014)*

- Managed the import and export processes for lift tables, jacks, compressors, oiling equipment, garage equipment, and engineering parts, coordinating between the company and international partners.

## Operating System Project

*C and System Programmers Association, Istanbul, Türkiye (2014–2015)*

- Completed courses in C, C++, Unix/Linux System Programming, and Assembly Language. Joined the operating system project in August 2015, tasked with implementing low-level programs for CSD, a new operating system developed by the C and System Programmers Association. The project involved creating a completely original kernel (not based on Linux), with a graphical user interface, supporting multithreaded preemptive operations on multicore hardware.

## Graduate Assistant

*Lehigh University, Bethlehem, United States (2017–2019)*

- Graded Mathematical Methods in Engineering I homework assignments.
- As a graduate assistant for the Strength of Materials course, held office hours to assist undergraduate students and graded their assignments.

## Lab Instructor & CAD Specialist & Graduate Energy Analyst

*Lehigh University, Bethlehem, United States (2019–2025)*

- Instructed undergraduate students in the laboratory for the Engineering Graphics and Design course using SOLIDWORKS CAD software.
- Participated in the Department of Energy's Industrial Assessment Center (IAC) at Lehigh University as graduate energy analyst, recommended energy efficiency practices and technologies to small and medium-sized manufacturing industries lacking dedicated energy personnel, ultimately helping to reduce production costs.